2015

Scanning angle Raman spectroscopy in polymer thin film characterization

Vy H. T. Nguyen
Iowa State University

Scanning Angle Raman spectroscopy in polymer thin film characterization

by

Vy H. T. Nguyen

A thesis submitted to the graduate faculty

in partial fulfillment of the requirements for the degree of

MASTER OF SCIENCE

Major: Analytical Chemistry

Program of Study Committee:
Emily A. Smith, Major Professor
Robert S. Houk
Joseph Burnett

Iowa State University

Ames, Iowa

2015

To my friends and family

TABLE OF CONTENTS

ACKNOWLEDGEMENTS

I would like to thank my committee chair, Emily Smith, and my committee members, Robert Sam Houk, and Joseph Burnett, for their guidance and support throughout the course of this research.

I would also like to thank family, friends, colleagues and advisors for the patience, love and support that have kept me moving forward.

Research work in this thesis has been done under the support of Department of Chemistry and the Ames Laboratory.

CHAPTER 1:

INTRODUCTION

THESIS OVERVIEW

The focus of this thesis is the application of Raman spectroscopy for the characterization of thin polymer films. Chapter 1 provides background information and motivation, including the fundamentals of Raman spectroscopy for chemical analysis, scanning angle Raman scattering and scanning angle Raman scattering for applications in thin polymer film characterization. Chapter 2 represents a published manuscript that focuses on the application of scanning angle Raman spectroscopy for the analysis of submicron thin films with a description of methodology for measuring the film thickness and location of an interface between two polymer layers. Chapter 3 provides an outlook and future directions for the work outlined in this thesis. Appendix A, contains a published manuscript that outlines the use of Raman spectroscopy to aid in the synthesis of heterogeneous catalytic systems. Appendix B and C contain published manuscripts that set a foundation for the work presented in Chapter 2.

RAMAN SPECTROSCOPY

Fundamental theory

Raman spectroscopy is an inelastic scattering phenomenon, which was first proposed by Adolf Smekal in 1923.[1] Landsberg and Mandelstam initiated a light scattering experiment on solid quartz and reported this discovery in February 1928.[2] Independently, a week later, Raman and Krishnan reported the observation of the scattering of light in pure liquid and vapor. In this original experiment, sunlight was used as an incoherent light source. It was focused onto the

sample using a telescope with a narrow band photographic filter.[3] The phenomenon was eventually called Raman scattering.[4] George Placzek further developed Raman instrumentation replacing the white light source with a low pressure mercury arc lamp and a spectrophotometric detector.[5] In the early days of Raman analyses, due to weak Raman intensities, fluorescence interference, and low efficiency detectors, Raman applications in chemical analysis required much more concentrated samples. For a period of time, Raman spectroscopy remained less popular than infrared spectroscopy.[6] In the last couple of decades, Raman spectroscopy experienced a growth in use with the introduction of near-infrared lasers, charged-coupled devices, and small personal computers.[5]

Raman spectroscopy is employed to detect molecular vibrations by Raman scattering. In Raman spectroscopy, a monochromatic light source is used to irradiate the sample. The photons incident on molecules cause the electron cloud around the nuclei to be polarized. This process promotes the electron's energy level, either from the ground state or low vibrational excited state, to the "virtual state". In the virtual state, the nuclei do not reach equilibrium and quickly drop to lower vibrational excited state or ground state. The process generates scattered photons that may have higher or lower energy compare to the original incident photons. The virtual state is a short-lived state that represents a distorted molecule. Rayleigh scattering is the dominant elastic scattering process, which occurs when the scattered photon has no change in its frequency. In the case of scattering involving induced nuclear motion, the scattered photons have a recognizable change in frequency from that of the incident photons, the process is inelastic and called Raman scattering. Raman scattering is known to be a low sensitivity technique as only one in every $10^6 – 10^8$ photons produces the Raman effect.[7]

The Jablonski diagram in Figure 1 shows the basic scattering process. The Rayleigh process does not involve a change in energy for the scattered photons. When a molecule's energy is at ground state *m*, after being promoted to a virtual state and then drops to an excited vibrational state *n*, the scattered photons have less energy than the incident photons and this process is called Stokes scattering. If a molecule is in a vibrationally excited state before the excitation photon is incident, and the scattered photon gains energy, anti-Stokes Raman scattering occurs. The relative intensities of Stokes and anti-Stokes scattering can be calculated using Boltzmann's equation.[4]

At room temperature, anti-Stokes scattering is weaker than Stokes scattering since the ground state *m* has a larger population of molecules in it compared to the excited state *n*. As the temperature increases, the ratio of Stokes to anti-Stokes scattering decreases. Even though anti-Stokes scattering is weaker in intensity and used less often, it is favorable over Stokes scattering in the presence of fluorescence interference.

Applications

Raman spectroscopy is a versatile analysis tool that can be used to study vapor, liquid and solid samples. The flexibility of sample handling allows the samples to be studied inside reaction containers or without a sample holder. By customizing the instrumentation, the sample analysis can be performed at varied conditions, temperatures and pressures. There are numerous publications covering Raman spectroscopy applications for polymer and copolymer analyses.[8] Gulari demonstrated the use of Raman spectroscopy in quantitative analysis.[9] In this work, a strong Raman band at 1545 cm^{-1} was used to observe the polymerization of methyl methacrylate initiated with azobisisobutyronitrile. In many cases, this approach is not possible due to the dependence of the band's intensity and location (wavenumber) on different polymer phases,

temperature and pressure. In many applications, Raman studies were performed on bulk samples in reaction vessels.[10-12] *In situ* Raman applications on polymer fibers and films provide physical properties and chemical compositions. Raman spectroscopy can be used to analyze the crystallinity, chain conformation and orientation of polymer.[13, 14]

SCANNING ANGLE RAMAN SPECTROSCOPY

When light encounters matter (gas, solid, liquid), it can be reflected, scattered, transmitted (refracted), or absorbed. The process can be expressed by the following relationship:

$$I_0 = I_R + I_A + I_S + I_T$$

where I_0 is the incident beam intensity, I_R , I_A , I_S , I_T are the portion of beam's intensities that are reflected, absorbed, scattered, and transmitted.[15]

When light is incident on an interface between two media with different refractive indices, refraction and reflection can occur, together with possible absorption and scattering. The refractive index of a medium is a measure of the medium-radiation interaction and is defined by $\eta(\lambda)=c/v(\lambda)$ where $\eta(\lambda)$ is the refractive index at wavelength λ, $v(\lambda)$ is radiation velocity in the medium, c is velocity of light in a vacuum. Provided the root-mean-square surface roughness is much smaller than the wavelength λ, the angle of incidence is equal to the angle of reflection. The fraction of the reflected radiation increases as the difference between the two media's refractive indices increases. The reflectance at the interface can be calculated by $R=\frac{I_R}{I_0}$.

If medium 1 (with refractive index η_1) and medium 2 (with refractive index η_2) are in contact with a smooth interface, $\eta_1 > \eta_2$ and the excitation light propagates from medium 1 to medium 2, total internal reflection (TIR) occurs at the interface when the incident angle of the

excitation light is larger than the critical angle. This critical angle is specific to the media's refractive indices, defined by

$$\theta_c = \sin^{-1}\eta_{21} \text{ where } \eta_{21} = \eta_2/\eta_1$$

The incident angle is defined as the angle between the incident beam and a vertical line perpendicular to the sample surface.[15, 16] When the incident angle θ_1 equals the critical angle θ_c, all the power of the incident light is reflected back into medium 1. In other words, light is totally reflected at $\theta_1 > \theta_c$, partially reflected and transmitted when $\theta_1 < \theta_c$, and transmitted at θ_1=90° angle of incidence. Polarization needs to be taken into account when one considers the amplitude change of the reflected light. Fresnel's equations for the parallel (transverse electric) polarized light amplitude are: $r = \frac{\tan(\theta_1 - \theta_2)}{\tan(\theta_1 + \theta_2)}$

and for the perpendicular (transverse magnetic) polarized light amplitude: $r = \frac{\sin(\theta_1 - \theta_2)}{\sin(\theta_1 + \theta_2)}$.

An evanescent wave is formed at the interface of the two media under TIR. This evanescent wave is non-transverse, localizes to medium 2 where it interfaces with medium 1, and propagates in all directions. Its intensity decreases exponentially perpendicular to the surface with distance Z into medium 2. This exponential decay can be described as a function of distance Z into medium 2:

$$E = E_0 \exp - \frac{2\pi}{\lambda_1} (\sin_2\theta - \eta^2_{21})^{1/2} Z$$

where $\lambda_1 = \lambda/\eta_1$ is the wavelength of radiation in medium1, λ is the original excitation light wavelength, Z is the distance into medium 2 from the surface.[16]

SA Raman spectroscopy with $\theta_1 < \theta_c$ uses a similar sample geometry to TIR Raman spectroscopy. When the incident angles of the excitation light on the prism/sample interface are varied over a selected angle range that is less than the critical angle, the excitation light probes

through the medium 2 and a series of Raman spectra are collected at each angle. Under the condition of $\eta_{\text{prism}} > \eta_{\text{layer 1}} > \eta_{\text{layer 2}}$, a radiative waveguide occurs at the prism/layer 1 (Fig. 2). The optical energy density localizes in the polymer film and interference occurs at certain incident angles. In the case where constructive interference occurs, an increase in the Raman signal can be observed. The pattern of the Raman signal over a range of incident angles is dependent on the polymer thickness. Fig. 3 shows the dependence of the sum square electric field on the polystyrene film thickness over a range of incident angles from 55° to 65°.

SA RAMAN SPECTROSCOPY FOR POLYMER FILM CHARACTERIZATION

Polymeric materials have replaced many traditional materials in recent years due to advantages, such as low cost and ruggedness. Commercial optical polymers were developed in many laboratories, which provided a wide range of polymer systems fit for different applications.[17-21] Eldada's work on crosslinked acrylate photopolymers found the materials have low optical loss, thermal stability, humidity resistance, low refractive index dispersion, flexibility, capability for precise refractive index and manufacturing.[22, 23]

Interest in the analysis of polymer interfaces as well as thin film characterization has been growing. The thickness of thin films can be measured by a variety of techniques. A majority of these techniques have their limitations. Techniques which are ion or electron spectroscopy based can be used for ultra thin films of less than 100 nm, however, these techniques require a vacuum.[24, 25] Popular techniques that do not require special working conditions, such as profilometry and atomic force microscopy, can be sample destructive due to the need to scratch the surface.[26, 27] In a 2008 study, a white light interferometer was used to determine thickness and homogeneity of thin polystyrene films. Even though this technique is a fast, non-contact and

highly accurate approach, white light interferometer measurements do not provide chemical information of films. Another limitation of previously mentioned techniques is the inability to detect or measure multilayered polymer films.[26, 28] There are techniques that can overcome this issue, such as infrared ellipsometry which can be used for thickness analysis of thin multilayered polymer films, however, the technique's sensitivity can be strongly affected by other experimental and theoretical parameters.[29] Thickness variation in the fluorocarbon polymer (FCP) film during the drying-curing process was studied by Wang and Hongo (1997) to obtain the optimum FCP inner-coating Ag hollow glass waveguide coating.[30]

Optical methods that have the ability to provide chemical and thickness information with little sample destruction and sample preparation have been investigated. Nikonenko applied infrared frustrated total internal reflection spectroscopy in determining 0.1-5.0 micron thin films.[31] Attenuated total reflection Fourier transform infrared (ATR-FT-IR) spectroscopy takes advantage of the evanescent wave formation in the polymer sample under TIR to perform depth profiling in thin polymer films. By varying the excitation wavelength and incident angle the penetration depth of evanescent wave can be controlled and be utilized for depth profiling. The penetration depth varies across the entire spectrum; hence the technique’s wavelength dependence complicates the analysis.[32-37] Confocal Raman spectroscopy has advantages and limitations in multilayered samples analysis.[38-42] Due to axial spatial resolution of couple hundred nanometers to a micron, confocal Raman spectroscopy cannot perform effectively on films thinner than one micron.

Attenuated total reflection (ATR)[28, 43] and total internal reflection (TIR) Raman spectroscopy have the advantages of optical methods and doesn’t suffer from the disadvantages attributed to ATR-FT-IR and confocal Raman spectroscopy.[44-47] TIR Raman spectroscopy has a

fixed excitation wavelength and possess a constant penetration depth of evanescent wave. As one of the pioneer in the field, Iwamoto's work in 1981 discussed TIR Raman spectroscopy in thin film measurements. In this work, the sublayer's thickness of bilayered polymer film of polystyrene (PS) and polyethylene or polycarbonate was characterized and Raman spectra could be collected from PS layer as thin as 6-200 nm.[48] Paul Bohn first introduced TIR Raman spectroscopy for optical characterization of transparent interfaces in 1997.[49] TIR Raman spectroscopy was later employed by Kivioja et al. to measure single thin film with thickness range from 50-350 nm.[50] Scanning angle (SA) Raman spectroscopy was employed in Fontaine et al. to experimentally investigated transparent micron-scaled thin films. In another experiment envolving PS/PMMA bilayer film, the team successfully determined the thickness of thin PS film, bilayer film and the buried PS/PMMA interface.[51, 52] The study, however, focused onto a narrow selection of samples, and failed to introduce a methodology to real life application on larger variety of thin films. Waveguide Raman spectroscopy was used to investigate ultrathin polymer films.[53-55] Further studies on optical waveguide modes can be found in Miller and Bohn's work. [56-58] McKee developed a SA Raman spectrometer that allows Raman spectra to be collected simultaneously with a change in incident angle.[59] This allowed polystyrene films with thickness ranged from 400 nm to 1800 nm to be measured with SA Raman spectroscopy and theoretical simulation.[60] The average uncertainty in film thickness determined by SA Raman spectroscopy in this study was 4% in comparison to optical interferometry.

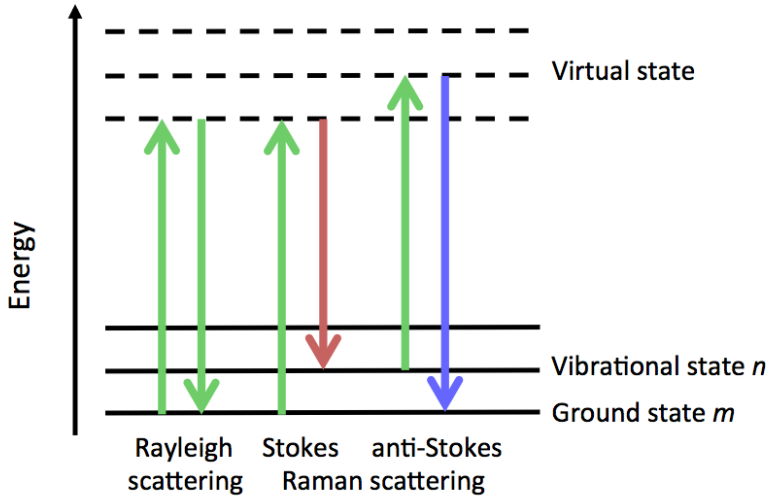

Fig. 1. Energy diagram for Rayleigh and Raman scattering. The Rayleigh process does not involve a change in the molecule's energy. Stokes scattering occurs when a molecule at ground state m is incident by a photon, promoted to virtual state and then drop to excited vibrational state n with a scattered photon that has less energy than the original incident photon. Anti-Stokes Raman scattering occurs when a molecule is in vibrational excited state n, after being promoted to virtual excited state, returns to ground state m after the scattering. The scattered photon in anti-Stokes has higher energy than the original incident photon.

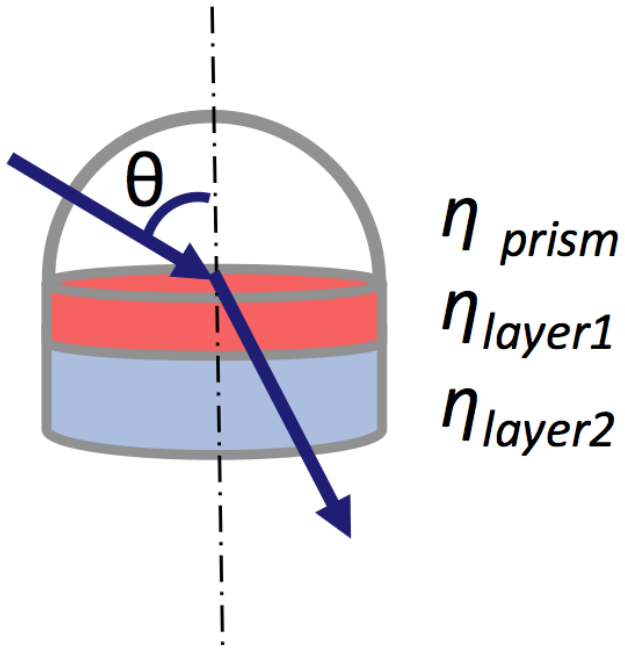

Fig. 2. Sample configuration for SA Raman spectroscopy.

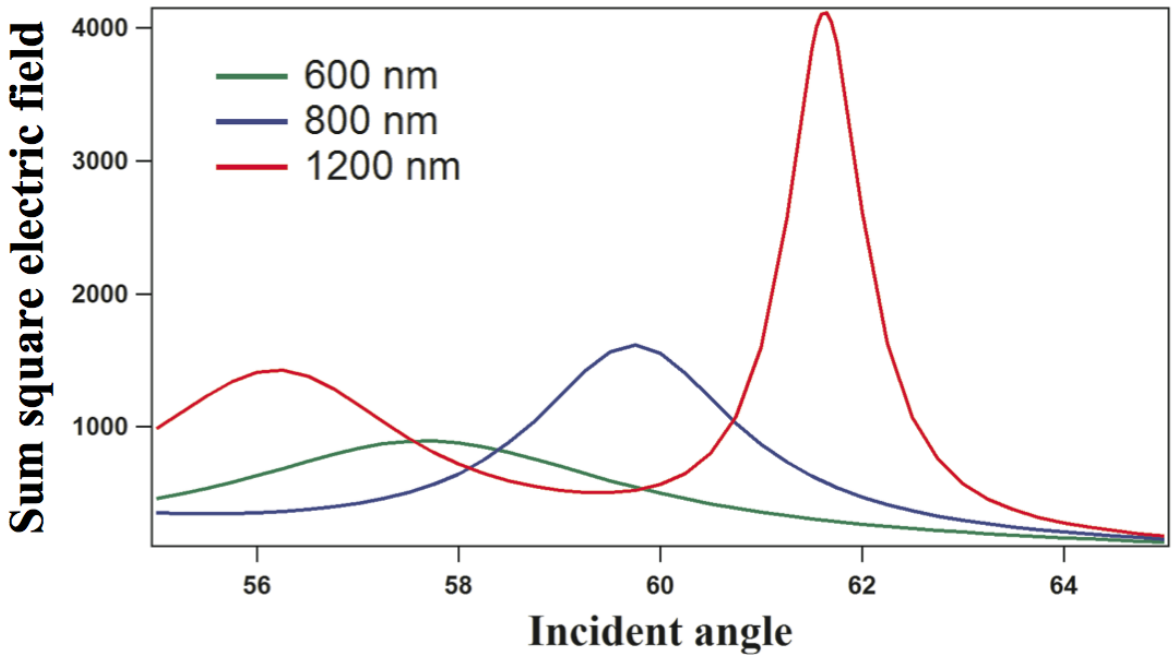

Fig. 3. The dependence of the Sum square electric field on polystyrene film thickness (600, 800, 1200 nm) over the incident angle range from 55° to 65°. The data were generated by finite-difference-time-domain (FDTD)-based simulations, and show the thicker polystyrene film (red) achieving higher SSEF intensity, in comparison to the thinner film at 600 nm (green).

REFERENCES

1. A. Smekal, *Z Phys*, 1923, **15**, 58-60.
2. R. Singh and F. Riess, *Notes Rec Roy Soc*, 2001, **55**, 267-283.
3. C. V. Raman and K. S. Krishnan, *Nature*, 1928, **121**, 501-502.
4. E. Smith and G. Dent, 2005.
5. G. Placzek, *Handbuch der Radiologie*, 1934, **6 part 2**.
6. M. R. L., *Raman Spectroscopy for Chemical Analysis*, John Wiley& Sons, Canada, 2000.
7. E. Smith and G. Dent, *Modern Raman Spectroscopy- A Practical Approach*, John Wiley& Sons Ltd., The Atrium, Southern Gate, Chichester, West Sussex, England, 2005.
8. H. G. M. Edwards, A. F. Johnson and I. R. Lewis, *Journal of Raman Spectroscopy*, 1993, **24**, 475-483.
9. E. Gulari, K. Mckeigue and K. Y. S. Ng, *Macromolecules*, 1984, **17**, 1822-1825.
10. J. F. Aust, K. S. Booksh, C. M. Stellman, R. S. Parnas and M. L. Myrick, *Applied spectroscopy*, 1997, **51**, 247-252.
11. L. F. Xu, C. Li and K. Y. S. Ng, *J Phys Chem A*, 2000, **104**, 3952-3957.
12. J. B. Cooper, K. L. Wise and B. J. Jensen, *Anal Chem*, 1997, **69**, 1973-1978.
13. B. Chase, *Mikrochim Acta*, 1997, 1-7.
14. P. J. Hendra, D. B. Morris, R. D. Sang and H. A. Willis, *Polymer*, 1982, **23**, 9-13.
15. M. W. Urban, *Attenuated Total Reflectance Spectroscopy of Polymers: Theory and Practice*, The American Chemical Society, Washington DC, 1996.
16. *Internal Reflection Spectroscopy: Theory and Applications*, Marcel Dekker, New York, 1993.
17. C. F. Kane and R. R. Krchnavek, *IEEE Photonic Tech L*, 1995, **7**, 535-537.

18. L. W. Shacklette, R. A. Norwood, L. Eldada, C. Glass, D. Nguyen, C. Poga, B. P. Xu, S. Yin and J. T. Yardley, *Nonlinear Optical Properties of Organic Materials X*, 1997, **3147**, 222-232.

19. L. Eldada, A. Nahata and J. T. Yardley, *Optoelectronic Interconnects V*, 1998, **3288**, 175-191.

20. Y. S. Liu, R. J. Wojnarowski, W. A. Hennessy, J. Rowlette, J. Stack, M. KadarKallen, E. Green, Y. Liu, J. P. Bristow, A. Peczalski, L. Eldada, J. Yardley, R. M. Osgood, R. Scarmozzino, S. H. Lee and S. Patra, *P Electr C*, 1997, 391-398.

21. R. Scarmozzino, R. M. Osgood, L. Eldada, J. T. Yardley, Y. Liu, J. Bristow, J. Stack, J. Rowlette and Y. S. Liu, *Optoelectronic Interconnects and Packaging Iv*, 1997, **3005**, 257-265.

22. L. Eldada and L. W. Shacklette, *Ieee J Sel Top Quant*, 2000, **6**, 54-68.

23. X. Li, X. H. Yu and Y. C. Han, *J Mater Chem C*, 2013, **1**, 2266-2285.

24. C. R. Brundle, *J Vac Sci Technol*, 1974, **11**, 212-224.

25. M. Bersani, D. Giubertoni, M. Barozzi, E. Elacob, L. Vanzetti, M. Anderle, P. Lazzeri, B. Crivelli and F. Zanderigo, *Appl Surf Sci*, 2003, **203**, 281-284.

26. I. Ohlidal and D. Franta, *Prog Opt*, 2000, **41**, 181-282.

27. M. M. Ayad and M. A. Shenashin, *Eur Polym J*, 2003, **39**, 1319-1324.

28. S. R. Kane, P. D. Ashby and L. A. Pruitt, *J Biomed Mater Res B*, 2009, **91B**, 613-620.

29. S. H. Kang, V. M. Prabhu, C. L. Soles, E. K. Lin and W. L. Wu, *Macromolecules*, 2009, **42**, 5296-5302.

30. Y. Wang, A. Hongo, Y. Kato, T. Shimomura, D. Miura and M. Miyagi, *Appl Optics*, 1997, **36**, 2886-2892.

31. N. A. Nikonenko and O. N. Tretinnikov, *Journal of Applied Spectroscopy*, 2008, **75**, 878-882.

32. P. M. Fredericks, in *Handbook of Vibrational Spectroscopy*, eds. J. M. Chalmers, P. R. Griffiths and E. Chichester, UK: John Wiley & Sons,Ltd, 2002, vol. 2, pp. 1493-1507.

33. P. M. Fredericks, in *Vibrational Spectroscopy of Polymers: Principles and Practice*, eds. N. Everall, J. M. Chalmers, P. R. Griffiths and N. Eds. Hoboken, John Wiley & Sons, Inc., 2007, pp. 179-200.

34. N. J. Harrick, *Phys. Rev. Lett.*, 1960, **4**, 224-226.

35. N. J. Harrick, *J Phys Chem-Us*, 1960, **64**, 1110-1114.

36. N. J. Harrick, *Ann Ny Acad Sci*, 1963, **101**, 928-959.

37. N. J. Everall, I. M. Priestnall, F. Clarke, L. Jayes, G. Poulter, D. Coombs and M. W. George, *Applied spectroscopy*, 2009, **63**, 313-320.

38. A. J. Sommer, in *Modern Techniques in Applied Molecular Spectroscopy*, ed. F. M. Mirabella, Wiley-Interscience, New York, 1998, pp. 291-322.

39. N. J. Everall, *Applied spectroscopy*, 2000, **54**, 1515-1520.

40. N. J. Everall, *Applied spectroscopy*, 2000, **54**, 773-782.

41. N. Everall, J. Lapham, F. Adar, A. Whitley, E. Lee and S. Mamedov, *Applied spectroscopy*, 2007, **61**, 251-259.

42. N. J. Everall, *Applied spectroscopy*, 2009, **63**, 245A-262A.

43. P. Yang, X. F. Meng, Z. Y. Zhang, B. X. Jing, J. Yuan and W. T. Yang, *Anal Chem*, 2005, **77**, 1068-1074.

44. T. Ikeshoji, Y. Ono and T. Mizuno, *Appl Opt*, 1973, **12**, 2236-2237.

45. T. Takenaka and T. Nakanaga, *J Phys Chem-Us*, 1976, **80**, 475-480.

46. D. A. Woods and C. D. Bain, *Analyst*, 2012, **137**, 35-48.

47. L. J. Tisinger and A. J. Sommer, in *Microscopy and Microanalysis*, 2004, vol. 10, pp. 1318-1319.

48. R. Iwamoto, K. Ohta, M. Miya and S. Mima, *Applied spectroscopy*, 1981, **35**, 584-587.

49. P. W. Bohn, *Annual Review of Materials Science*, 1997, **27**, 469-498.

50. A. O. Kivioja, A. S. Jaaskelainen, V. Ahtee and T. Vuorinen, *Vibrational Spectroscopy*, 2012, **61**, 1-9.

51. N. H. Fontaine and T. E. Furtak, *Physical Review B*, 1998, **57**, 3807-3810.

52. N. H. Fontaine and T. E. Furtak, *Journal of the Optical Society of America B-Optical Physics*, 1997, **14**, 3342-3348.

53. J. F. Rabolt, R. Santo and J. D. Swalen, *B Am Phys Soc*, 1980, **25**, 400-400.

54. J. F. Rabolt, R. Santo and J. D. Swalen, *Applied spectroscopy*, 1980, **34**, 517-521.

55. J. F. Rabolt, N. E. Schlotter and J. D. Swalen, *J Phys Chem-Us*, 1981, **85**, 4141-4144.

56. D. R. Miller, O. H. Han and P. W. Bohn, *Applied spectroscopy*, 1987, **41**, 249-255.

57. D. R. Miller and P. W. Bohn, *Appl Opt*, 1988, **27**, 2561-2566.

58. D. R. Miller and P. W. Bohn, *Anal Chem*, 1988, **60**, 407-411.

59. K. J. Mckee and E. A. Smith, *Rev Sci Instrum*, 2010, **81**.

60. M. W. Meyer, V. H. T. Nguyen and E. A. Smith, *Vibrational Spectroscopy*, 2013, **65**, 94-100.

CHAPTER 2:

APPLICATION OF SCANNING ANGLE RAMAN SPECTROSCOPY FOR DETERMINING THE LOCATION OF BURIED POLYMER INTERFACES WITH TENS OF NANOMETER PRECISION

A paper published in Analyst.

Craig A. Damin[ab†], Vy H. T. Nguyen[ab†], Auguste S. Niyibizi[a] and Emily A. Smith[ab]*

[a] Ames Laboratory, U.S. Department of Energy, Ames, IA 50011-3111, USA
[b] Department of Chemistry, Iowa State University, Ames, IA 50011-3111, USA

ABSTRACT

Near-infrared scanning angle (SA) Raman spectroscopy was utilized to determine the interface location in bilayer (a stack of two polymer layers) films of polystyrene (PS) and polycarbonate (PC). Finite-difference-time-domain (FDTD) calculations of the sum square electric field (SSEF) for films with total bilayer thicknesses of 1200-3600 nm were used to construct models for simultaneously measuring the film thickness and the location of the buried interface between the PS and PC layers. Samples with total thicknesses of 1320, 1890, 2300, and 2750 nm and varying PS/PC interface locations were analyzed using SA Raman spectroscopy. Comparing SA Raman spectroscopy and optical profilometry measurements, the average percent difference in the total bilayer thickness was 2.0% for films less than ~2300 nm thick. The average percent difference in the thickness of the PS layer, which reflects the interface location, was 2.5% when the PS layer was less than ~1800 nm. SA Raman spectroscopy has been shown to be a viable, non-destructive method capable of determining the total bilayer thickness and

buried interface location for bilayer samples consisting of thin polymer films with comparable indices of refraction.

INTRODUCTION

Thin and ultrathin polymer films are currently employed for use in the fields of optics, photovoltaics, microelectronics, and coatings.[1-3] In many applications, the thickness and composition of these films affect their function; therefore, accurate determinations of film thickness and composition are required. Interferometric methods, such as scanning white light interferometry, are commonly used to measure the thickness of polymer films.[4-6] A 2008 study by Madani-Grasset et al. employed a commercial scanning white light interferometer to determine thickness and homogeneity of 3 to 15 nm thick films of PS deposited on a borosilicate glass substrate.[7] Interferometry offers a fast, non-contact optical method capable of determining film thickness with high accuracy; however, this technique does not provide chemical information about the samples.

Attenuated total (internal) reflection-Fourier transform infrared (ATR-FT-IR) spectroscopy is a viable technique for depth profiling thin polymer films.[8,9] ATR-FT-IR spectroscopy is performed by placing the sample in optical contact with an internal reflection element.[10-13] Infrared light passing through the internal reflection element at angles equal to or greater than the critical angle will undergo total internal reflection (TIR) at the interface, resulting in the formation of an evanescent wave in the sample. Depth profiling using ATR-FT-IR spectroscopy can be accomplished by varying the penetration depth of the evanescent wave, which is dependent on the wavelength and

angle of incidence. The wavelength dependence of the penetration depth complicates the analysis since the penetration depth is not constant across the entire spectrum.

Confocal Raman spectroscopy utilizes a remote, limiting aperture placed at an image plane of the illuminated sample to reduce the contributions from out-of-focus regions and improve axial spatial resolution.[14] Everall has shown the capabilities and limitations of performing *z*-axis scanning by confocal Raman spectroscopy for the analysis of multi-layered samples, such as polymers.[15-18] Even though the axial spatial resolution can be improved through the use of a confocal aperture, the resolution is still on the order of a few hundreds of nanometers or more.

TIR-Raman (alternatively ATR-Raman) spectroscopy offers a potential solution to the problems associated with ATR-FT-IR spectroscopy and confocal Raman spectroscopy.[19-21] TIR-Raman spectroscopy is analogous to ATR-FT-IR spectroscopy in that the sample must be optically coupled to a material possessing a high index of refraction. Distinct from ATR-FT-IR spectroscopy, the Raman excitation wavelength is fixed and an order of magnitude shorter resulting in a reduced penetration depth of the evanescent wave, a value that is constant across the entire spectrum. The capability of TIR-Raman spectroscopy for characterizing thin surface layers was studied by Iwamoto et al. using a bilayer of polystyrene (PS) with polyethylene or polycarbonate (PC).[22] They reported that Raman spectra could be collected from PS surface layers as thin as 0.006-0.2 μm and that the thickness of the film could be determined by varying the incident angle of the laser excitation. A 2004 study by Tisinger and Sommer represented the first attempt at performing TIR-Raman spectroscopy using a conventional Raman microscope.[23] The authors reported Raman spectra of a 3.2 μm thick polydiacetylene film

spin coated onto the bottom of a zinc selenide prism. Thickness measurements of thin isotropic PS films on polypropylene substrates were performed by Kivioja et al. using TIR-Raman spectroscopy.[24]

Scanning angle (SA) Raman spectroscopy (alternatively known as variable angle Raman spectroscopy) is similar to TIR-Raman spectroscopy in that both techniques utilize similar sample geometries. However, unlike TIR-Raman spectroscopy, in which the angle of incidence at the prism-sample interface is usually fixed and equal to or greater than the critical angle required for TIR, SA Raman spectroscopy is performed by scanning the incidence of the laser excitation over a range of angles while collecting the Raman scattered light. SA Raman spectroscopy is suited to measuring optical waveguides possessing thicknesses on the order of the excitation wavelength. Radiative, or "leaky", waveguides can occur at the prism-dielectric film interface when $\eta_{\text{prism}} > \eta_{\text{layer 1}} > \eta_{\text{layer 2}}$ (η represents the index of refraction).[25] The optical energy density localized to the waveguide film can exhibit an interference pattern across selected incident angles due to multiple total internal reflections within the film.[26] Enhancements in the optical energy density are observed at angles where constructive interference occurs. Among other parameters, these enhancements are dependent upon the thickness of the dielectric film.

A study by Levy et al. indicated that thin films supported on a substrate forming an asymmetric slab waveguide could be used to obtain a Raman spectrum.[26] Waveguide Raman spectroscopy was later used to study ultrathin polymer films by Rabolt et al.[27-30] Optical waveguide modes in thin polymer films were also studied by Miller and Bohn.[31-35] Miller et al. compared the experimentally observed Raman scattering ratios of PS and poly(vinylpyrrolidone) to those based on computational iterations of film thicknesses and

indices of refraction.[32] It was concluded that such calculations for a range of waveguide thicknesses would require extensive computational time and a more efficient method capable of relating the electric field intensities to the observed Raman signals of multi-layered samples with varying thicknesses was needed.

Fontaine and Furtak demonstrated the extraction of depth-resolved vibrational information from transparent, optically homogeneous samples, including a 15-μm PS film using SA Raman spectroscopy.[36] They later demonstrated the ability to determine the thickness of a single-layer PS film and the location of buried interfaces between two immiscible polymers, PS and poly(methyl methacrylate) (PMMA).[25] The thicknesses of the single-layer PS films and the PS/PMMA bilayer were determined using the integrated scattering intensities of PS and PMMA Raman transitions. Although film thicknesses and the buried interface location were determined, the study was limited to a single 1200-nm PS film and a 3045-nm PS/PMMA bilayer sample. The model presented by Fontaine and Furtak could not be easily applied to other samples.

In a 2008 publication by Ishizaki and Kim, a near-infrared TIR-Raman spectrometer capable of measuring polymer surfaces was reported.[37] The utility of the instrument was demonstrated by collecting Raman spectra from a bilayer film consisting of a 130 nm thick layer of PS and a 250 μm thick layer of poly(vinyl methylether) at various incident angles between 50 and 70°. Ishizaki and Kim demonstrated the incident angle dependency of the Raman intensities for the PS/poly(vinyl methylether) sample and calculated the optical electric field at the prism/PS interface; however, the study did not include a method of determining the thicknesses of the films and the location of the buried interface between the polymers.

In 2010, McKee and Smith discussed the development of a SA Raman spectrometer capable of precisely varying the angle of incidence for measuring interfacial phenomena with chemical specificity and high axial resolution.[38] Meyer et al. presented a SA Raman method for measuring the thickness and composition of PS films spin coated onto a sapphire substrate using this instrument.[39] The goals of the present study were to present reliable models for determining: (1) the total thickness of PS/PC bilayer films and (2) the location of the buried PS/PC interfaces using SA Raman spectroscopy. Calibration models based on the SSEFs were constructed and applied to experimental SA Raman spectroscopy data for PS/PC bilayer films with total thicknesses ranging from 1.3-2.8 μm with varying interface locations.

EXPERIMENTAL

Sample preparation

Polystyrene (PS, M_W = 280×10^3) and poly(bisphenol A carbonate) (PC, M_w = 64×10^3) were purchased from Sigma-Aldrich (St. Louis, MO). Solutions of PS in toluene and PC in methylene chloride were prepared with concentrations ranging from 0.02-0.14 g/mL. Thin films of PS and PC were prepared using a Chemat Technology (Northridge, CA) KW-4A spin coater. First, 200 μL of the PS solution was dispensed onto a 1-in. diameter 0.02-in. thickness sapphire disk (Meller Optics, Providence, RI). After depositing the solution, the substrate was spun at 3000 rpm for 60 seconds. The PS film was allowed to dry overnight at room temperature. Thin films of PC were prepared on BK7 glass slides (Corning Glass, Corning, NY) using the same method as that used for the PS films. The thicknesses of the PS and PC films were determined using a Zygo

(Middlefield, CT) NewView 7100 3D optical surface profiler. Calibration curves of PS and PC film thickness, as measured by optical profilometry, versus the concentration of the polymer solution spin coated on the substrate are shown in supplemental information Fig. S1.

Bilayer films of PS and PC were prepared using the wedge transfer method.[40] The thickness of the PS layer divided by the thickness of the PC layer was defined as $Thick_{PS}/Thick_{PC}$. The bilayer samples were prepared to represent the conditions of: (1) $Thick_{PS}/Thick_{PC} < 1$, (2) $Thick_{PS}/Thick_{PS} \approx 1$, and (3) $Thick_{PS}/Thick_{PC} > 1$. Deionized water from a Barnstead 18.2 MΩ EasyPure II filtration system (Thermo Scientific, Waltham, MA) was filtered using a 0.20 µm sterile syringe filter (Corning Inc., Corning, NY). The PC thin film was extracted from the glass slide to the surface of the water. The sapphire substrate containing the PS thin film was submerged in water and lifted out to collect the PC film. The bilayer polymer film was heated at 40°C for 7 hours to remove residual water.

Surface characteristics of the PS film and the PS/PC bilayer were characterized using a Digital Instruments (Tonawanda, NY) Multimode atomic force microscope (AFM) equipped with a Bruker (Camarillo, CA) triangular sharp nitride lever probe with a resonant frequency of 40-75 kHz and spring constant of 0.1-0.48 N/m. The AFM system was operated in contact mode.

SA Raman instrumentation

SA Raman spectra were collected using a Raman microscope previously described by McKee et al.[38] The instrument was based on a Nikon (Melville, NY) Eclipse TE2000-

U inverted microscope coupled to a Kaiser Optical Systems (Ann Arbor, MI) HoloSpec f/1.8i holographic imaging spectrometer. The 785-nm line of a Toptica Photonics (Victor, NY) XTRA II high-power, near-infrared-enhanced diode laser was used for excitation. A polarizer and a half-wave plate were used to provide *p*-polarized excitation. The laser power at the sample position in the absence of the prism was maintained at 250 mW and was measured using an Ophir Photonics (North Logan, UT) NOVA II power meter. Raman scattered light from the PS and PC samples was collected using a 10× (0.30 NA) objective. The HoloSpec Raman spectrometer utilized a 25-μm slit and a Kaiser HSG-785-LF volume phase holographic (VPH) grating. The detector was a Princeton Instruments (Trenton, NJ) PIXIS 400 1340×400 near-infrared-enhanced CCD imaging array with 20 μm × 20 μm pixels. The detector was thermoelectrically cooled to -70°C. A 1:1 (v/v) solution of acetonitrile/toluene was used for wavelength calibration. Princeton Instruments WinSpec/32 [v. 2.6.14 (2013)] was used to collect data.

SA Raman spectroscopic measurements

The SA Raman sample configuration is illustrated in Fig. 1. The sapphire disk containing the bilayer PS/PC sample was brought into optical contact with a 25.4-mm diameter hemispherical sapphire prism (ISP Optics, Irvington, NY) using index matching fluid (η = 1.780, Cargille Labs, Cedar Grove, NJ). A custom-made sample holder was used to secure the prism and the sample to the microscope stage. SA Raman spectra of the bilayer films were collected over an angle range of 55.70-65.70° with respect to the surface normal using a 0.05° angle resolution. The selected angle range included angles above and below the critical angle required for TIR at the sapphire-PS interface. A single

acquisition was collected at each angle using a ten second exposure time. Replicate measurements were acquired by consecutive scans through the entire angle range.

Sum square electric field (SSEF) calculations

Three dimensional finite-difference-time-domain (FDTD)-based simulations (EM Explorer, San Francisco, CA) were used to calculate the SSEF over each layer of a 4-layer system consisting of a sapphire prism, PS film, PC film, and air. The input values for these calculations included the refractive indices of the layers at 785 nm and the thickness of each layer. The refractive indices of sapphire, PS, and PC for *p*-polarized 785-nm excitation were 1.762, 1.578, and 1.571, respectively.[41-43] In the simulations, the thickness of the prism and air layers were semi-infinite compared to the polymer layers. The total bilayer thickness varied from 1200-3000 nm in 100-nm increments and 3000-3600 nm in 200-nm increments with PS thicknesses varying from 6.25-93.75% (in 6.25% increments) of the total bilayer thickness. The angular range of 55-65^{o} at an angle resolution of 0.05^{o} was selected in order to coincide with the experimental conditions. The SSEF calculations were performed using a Yee cell size of 5 nm and a uniform index of refraction across a layer.

Relative Raman scattering cross-section

The calculated SSEF is proportional to the experimental Raman scattering after correcting the SSEF for differences in the PS and PC Raman scattering cross-sections. The relative Raman cross-sections of PS and PC were determined using a PS compact disk case and the PC substrate of a rewritable compact disk. The reflective coating on the

compact disk was removed prior to analysis. The thicknesses of the PS and PC samples measured with a digital caliper were 1.01 ± 0.01 mm and 1.09 ± 0.01 mm, respectively. Raman spectra of the PS and PC samples were collected using a 180° backscattering geometry with 785-nm excitation. Excitation and collection of the resulting Raman scattered light was done using a 10× (0.30 NA) objective. The laser power at the sample was 90 mW. The collected Raman spectra represented a two second exposure for a single accumulation. Integrated areas of the PS 1001 cm^{-1} and PC 889 cm^{-1} Raman transitions were determined using a Gaussian fit algorithm available in the multipeak fitting package of IGOR Pro (WaveMetrics, Inc., Lake Oswego, OR) [v. 6.3.4.1 (2014)]. The ratio of the integrated area of PS to that of PC was 2.0 ± 0.1. The uncertainty in the relative Raman scattering cross-section was calculated using the standard deviation associated with three replicate determinations of the integrated areas for the selected PS and PC Raman transitions.

Data analysis

IGOR Pro 6.4 was used to analyse the SA Raman spectra and results of the SSEF calculations from the FDTD simulations. Peak areas of the 1001 cm^{-1} and 889 cm^{-1} PC Raman transitions were determined using a Gaussian fit function with a linear baseline. Plots of Raman intensity versus incident angle were fit to a Lorentzian function in order to identify the angular positions and Raman intensities of the most intense waveguide modes. Matlab (MathWorks, Natick, MA) [v. 8.4.0.150421 (2014)] was used to construct surface plots of the resulting Raman data and FDTD calculations.

RESULTS AND DISCUSSION

SSEF calculations for the PS/PC bilayer films

The goal of this study was to determine the locations of buried interfaces between layers of PS and PC using SA Raman spectroscopy. PS and PC were selected for the present study because they possess similar refractive indices at the 785-nm excitation wavelength and thus optically can be treated as single layer. The first step of this method was to develop models capable of predicting the total bilayer thickness and the composition of the two-polymer samples based on the SSEF, which is related to the SA Raman signal. SSEF values were calculated using FDTD methods. Calculations were performed for bilayer films with total thicknesses ranging from 1200-3600 nm. In order to differentiate between bilayer films within this thickness range, an incident angle range of 55-65^{o} was used. The critical angle required for TIR at the sapphire/PS interface is 63.6^{o}. Extending the angle range to values below 55^{o} permits models of thinner films to be constructed; however, extension of the angle range also increases computing time.

FDTD is a numerical analysis technique that is used to perform electromagnetic simulations.[44] The FDTD method was originally proposed by Yee in a seminal paper published in 1966.[45] The FDTD method employs finite differences as approximations to both the spatial and temporal derivatives that appear in Maxwell's equations. In the present study, 3D FDTD calculations were performed with *p*-polarized incident light and perfectly matched layers (PMLs) as boundary conditions. The output of the calculations included the percent reflected light from the interface, the integrated electric field over the PS and PC layers, and the electric field profile over the entire 4-layer system at each incident angle. The FDTD method is capable of solving complicated problems; however,

it is generally computationally expensive. Depending on the polarization of the incident light, it is possible to use 1D or 2D FDTD calculations to develop a model requiring appreciably less computing time.

Surface plots of the calculated SSEF versus angle and the interface location for bilayer films with total thicknesses of 1300, 2200, and 2700 nm are shown in Fig. 2. (Note: the interface location is represented as either the percent thickness of PS relative to the total bilayer thickness or the ratio of the PS to PC thicknesses, $Thick_{PS}/Thick_{PC}$, throughout the text.) SSEF values calculated for the PS and PC layers are shown in the left (A, C, and E) and right (B, D, and F) plots, respectively. The most intense waveguide mode was designated mode 0. Additional modes were sequentially assigned (1, 2, etc.) based on their intensities. For example, in the SSEF plots of the 2700 nm thick bilayer film, mode 0 was located at 63.10^o for PS (Fig. 2E) and 62.60^o for PC (Fig. 2F). Mode 1 for PS and PC were respectively located at 61.75^o and 61.25^o. As the total bilayer thickness increased, additional modes were observed, and the locations of these modes shifted to higher angles.

The angle difference between modes 0 and 1, hereafter designated as $\Delta\theta$, is affected by the total bilayer thickness. For example, $\Delta\theta$ calculated for the PS layer ($\Delta\theta_{PS}$) when it is 25% of the total film thickness was 4.60^o, 1.80^o, and 1.25^o for films with total bilayer thicknesses of 1300, 2200, and 2700 nm, respectively. The SSEF surface plots presented in Fig. 2 also show that there is a minor dependence of $\Delta\theta$ on the location of the buried interface. It is for this reason that the SSEF plots for PS and PC are not mirror images.

The interdependence of $\Delta\theta$ on the total bilayer thickness and interface location can affect the accuracy associated with determinations of total bilayer thickness by SA Raman

spectroscopy. Plots of $\Delta\theta$ versus total bilayer thickness are shown in Fig. 3 for PS and PC. Each curve represents a fixed interface location ($Thick_{PS}/Thick_{PC}$). Using the parameter $\Delta\theta$ and the PS or PC signal, the uncertainty in the bilayer thickness will be greatest for thicker films since the curves approach zero slope. For thinner films, $\Delta\theta$ for PC ($\Delta\theta_{PC}$) will produce a smaller uncertainty than the PS signal since the latter has a larger distribution of values for a given total bilayer thickness. The PS film is located closer to the prism interface, which makes $\Delta\theta$ more sensitive to the interface location. The uncertainty associated with determinations of total bilayer thickness is further complicated by the limitation of accurately measuring the incident angle. All curves shown in Fig. 3 were fit to power functions; the corresponding fit functions and their In order to account for the interdependence of $\Delta\theta$ on total bilayer thickness and interface location, a second parameter, the SSEF was included in the model. The ratio of the maximum SSEF at mode 0 for PS to the maximum SSEF at mode 0 for PC ($SSEF_{PS}/SSEF_{PC}$) was multiplied by the relative Raman scattering cross-section in order to correlate $SSEF_{PS}/SSEF_{PC}$ to the experimental Raman scattering intensities of the polymers (Int_{PS}/Int_{PC}). Correction of the SSEF ratio using the relative Raman scattering cross-section was done under the assumption that the photon collection efficiency was consistent across the entire film thickness, which will hold for the low numerical aperture objective used in this study. The Rayleigh length for the optical system is approximately 10 μm.

Curves relating the interface location ($Thick_{PS}/Thick_{PC}$) to the corrected $SSEF_{PS}/SSEF_{PC}$ ratio and, by extension, the Raman scattering intensities, were constructed for total bilayer thicknesses of 1200-3600 nm. Selected plots of the corrected $SSEF_{PS}/SSEF_{PC}$ ratio versus

$Thick_{PS}/Thick_{PC}$ are shown in Fig. 4. All of the curves were fit to power functions over the full $Thick_{PS}/Thick_{PC}$ range of 0.067-15. The resulting fit functions are listed in supplemental table S1. By defining a range of restricted $Thick_{PS}/Thick_{PC}$ values, the uncertainty in the fit function can be reduced, thereby improving the accuracy of determining the location of the buried interface between the two polymers. The power fit functions corresponding to the $Thick_{PS}/Thick_{PC}$ range of 0.067-3 are listed in Table 2. The average RMSR of the fit functions over the selected range was 0.06.

In summary, the unknown sample variables to be determined in this analysis were the total bilayer thickness and $Thick_{PS}/Thick_{PC}$. These variables, which are defined by the fit functions in Tables 1 and 2, are a function of parameters that can be experimentally determined: (1) $\Delta\theta$, the angle difference between modes 0 and 1 for PS or PC, and (2) Int_{PS}/Int_{PC} determined at mode 0. Both of the unknown variables can be determined by defining the relevant fit functions for a given sample using Tables 1 and 2 and the two experimentally-determined parameters. The magnitude of the uncertainty for each variable is sample-dependent, as further described below.

SA Raman spectroscopy of bilayer PS/PC films

SA Raman data collected for a 2300 nm thick bilayer film are shown in Fig. 5. The PS and PC film thicknesses were measured by optical profilometry to be 1100 ± 30 and 1200 ± 60 nm, respectively. Raman spectra of the bilayer sample exhibited transitions associated with both PS and PC. The dominant Raman transitions of PS and PC were observed at 1001 and 889 cm^{-1}, respectively. The Raman spectra of PS[46-48] and PC[49,50] have been previously reported. The 1001 cm^{-1} shift transition of PS has been assigned to

the aromatic ring breathing mode. A transition located at 1028 cm^{-1} was assigned to a C-H in-plane bending mode of PS.[47] The 889 cm^{-1} shift transition of PC has been previously assigned to both an O-C(O)-O stretch and a C-CH_3 stretch. Additional Raman transitions observed at 1108 and 1180 cm^{-1} were associated with PC. These transitions have been previously assigned to C-O-C stretches[43] and in-plane C-H wags[50]. In the discussion to follow, all quantitation was performed using the 1001 and 889 cm^{-1} shift transitions of PS and PC, respectively. In Fig. 5, the maximum intensity for mode 0 of PS, located at 63.52º, possessed an intensity of ~7000 arbitrary units, and the maximum intensity for mode 0 of PC, located at 63.45º, possessed an intensity of ~3500 arbitrary units. Considering the approximately equal PS and PC thicknesses for this sample, the ratio of Int_{PS}/Int_{PC} was consistent with that observed for bulk PS and PC samples, which had a relative Raman cross-section ratio of 2.0 ± 0.1.

The application of SA Raman spectroscopy for determinations of total bilayer thickness and buried interface location requires samples with smooth surfaces. The SSEF calculations assume smooth surfaces for the individual layers. Atomic force microscopy (AFM) was used to investigate the surface characteristics of two types of samples: (1) an 1800 nm thick PS film on a glass substrate prior to the deposition of a PC layer and (2) a 2500 nm thick bilayer film consisting of PS and PC thicknesses of 1800 and 700 nm, respectively. The resulting AFM images are shown in supplemental information Fig. S2. The root-mean-square roughness of the PS film was 0.29 nm, and the vertical distance between the highest and lowest points of the AFM image was 2.1 ± 0.3 nm. The surface of the PS film (supplemental information Fig. S2A) was characterized as a smooth surface because the peak-to-peak roughness was appreciably less than the excitation wavelength. The root-mean-square roughness of the bilayer film (supplemental

information Fig. S2B) was 0.25 nm, and the vertical distance between the highest and lowest points of the AFM image was 2.6 ± 0.3 nm. Given that the peak-to-peak roughness for the two polymers was similar, and much smaller than the excitation wavelength, the transfer process produced a bilayer sample with a smooth interface between the individual layers.

SA Raman data collected for four PS/PC bilayer films are shown in Fig. 6. The PS and PC thicknesses measured by optical profilometry are listed in Fig. 6 for samples prepared using identical conditions as those used to prepare samples for the SA Raman studies. Optical profilometry is a destructive technique that precluded measuring the individual PS and PC thicknesses on the same samples used for the SA Raman analysis. It was assumed that the PS and PC thicknesses are not altered by the transfer process used to generate the bilayer and that the total bilayer thickness is the sum of the PS and PC thicknesses. In order to test the validity of this assumption, the total bilayer thickness was measured by optical profilometry for each sample after the Raman analysis was complete. The average difference between the sum of the PS and PC thicknesses measured on independent samples and the total bilayer thickness of the SA Raman samples was 6%.

The values of $\Delta\theta$ and Int_{PS}/Int_{PC} obtained from the spectra in Fig. 6 are listed in Table 3. The application of SA Raman spectroscopy for determinations of total bilayer and PS thicknesses was performed in two steps. *Step 1*. The experimentally-determined values of $\Delta\theta_{PS}$ and $\Delta\theta_{PC}$ were input into each of the corresponding fit functions listed in Table 1. Fifteen values representing the curves for $Thick_{PS}/Thick_{PC}$ ranging from 0.067-15 were obtained for each interface. The resulting data are plotted as the gray (PS) and open (PC) symbols in Fig. 7. In order to improve the clarity of the constructed plots, the $Thick_{PS}/Thick_{PC}$ ratios have been restricted to a range of 0 to 5. *Step 2*. The ratio of

Int_{PS}/Int_{PC} determined at mode 0 for each sample was input into the fit functions listed in Table 2 to obtain twenty-two values plotted as black symbols in Fig. 7. The *x*- and *y*-values at the intersections of the fit functions (supplemental information Tables S2 and S3) represent the location of the buried interface and the total bilayer thickness, respectively.

Considering the range of $Thick_{PS}/Thick_{PC}$ represented in Fig. 7, there are appreciable differences in the total bilayer thicknesses calculated using $\Delta\theta_{PS}$ and $\Delta\theta_{PC}$ for values below 0.5. Determinations of total bilayer thickness within this region will inherently possess greater uncertainties than those performed at larger thickness ratios. As the value of $Thick_{PS}/Thick_{PC}$ increased, the total bilayer thicknesses calculated using $\Delta\theta_{PS}$ and $\Delta\theta_{PC}$ converged for the data shown in Fig. 7A, C and D, indicating good agreement between the two values. The curves presented in Fig. 7B possessed an appreciable difference in the total bilayer thicknesses calculated using the values of $\Delta\theta_{PS}$ and $\Delta\theta_{PC}$ across the entire range of $Thick_{PS}/Thick_{PC}$. This data set had a smaller value of $\Delta\theta_{PC}$ compared to the expected calculated value by 2°. When the smaller value of $\Delta\theta_{PC}$ is input into the fit functions (Table 1) the total bilayer thickness is overestimated.

The total bilayer and PS thicknesses determined by SA Raman spectroscopy are summarized in Table 3. The listed values represent averages of the total bilayer thickness and interface locations determined using the PS and PC fit functions. Percent differences between the total bilayer thicknesses determined by SA Raman spectroscopy and optical profilometry were 0.8% (sample 4) and 1.6% (sample 3) and increased for the thicker samples, as expected based on the preceding discussion of Figure 3. The accuracy associated with thickness determinations for samples thicker than ~2300 nm can potentially be improved through the construction of

calibration models based on the angle difference between modes 1 and 2, or even higher modes. The angle difference for higher order modes will be larger for thicker films than the angle difference between modes 0 and 1, as shown in Figure 2.

The percent difference between the SA Raman spectroscopy and optical profilometry determinations of the buried interface location (PS thickness) was less than 6% for all four samples. The small percent differences indicate that accurate determinations of the buried interface location between two optically homogeneous polymers can be obtained using the outlined method. When considering the capabilities of three complementary Raman techniques: TIR, SA, and confocal Raman spectroscopy, the methodology presented herein fills a missing gap for measuring films of a few hundred nanometers to a few micrometers thickness with tens-of-nanometer precision. The lower limit is governed by the polymer thickness required to form a waveguide, while the upper thickness is governed by the optics. To increase the polymer thickness range that can be studied with the SA Raman methodology, a shorter excitation wavelength could be employed to extend the range at lower thicknesses. In addition, the incident angle range could also be extended, as already discussed.

CONCLUSIONS

Near-infrared SA Raman spectroscopy has been shown to be a viable, non-destructive method for determinations of chemical composition, total bilayer thickness, and buried interface location. The latter two parameters determined using this method were in agreement with independent measurements performed using optical profilometry. For the analysis of thin film compositions, SA Raman spectroscopy offers the advantage of at least an order of magnitude

improvement in axial spatial resolution compared to wide-field and confocal Raman spectroscopy. While the two polymers used in this study had similar indices of refraction, the method is expected to be applicable to the analysis of polymer bilayers where the refractive indices of the layers vary. The limits of suitable indices of refraction, however, need to be studied. SA Raman spectroscopy is applicable to the analysis of multi-layered polymer films when information regarding chemical composition and thickness is required.

ACKNOWLEDGEMENTS

This research is supported by the U.S. Department of Energy, Office of Basic Energy Sciences, Division of Chemical Sciences, Geosciences, and Biosciences through Ames Laboratory. The Ames Laboratory is operated for the U.S. Department of Energy by Iowa State University under Contract No. DE-AC02-07CH11358. The authors thank Wyman Martinek for his assistance with the optical profilometry measurements.

REFERENCES

1 Y. Wang, A. Hongo, Y. Kato, T. Shimomura, D. Miura and M. Miyagi, Appl. Opt., 1997, **36**, 2886-2892.

2 L. Eldada and L. W. Shacklette, IEEE J. Sel. Top. Quant., 2000, **6**, 54-68.

3 X. Li, X. H. Yu and Y. C. Han, J. Mater. Chem. C, 2013, **1**, 2266-2285.

4 S. W. Kim and G. H. Kim, Appl. Opt., 1999, **38**, 5968-5973.

5 M. Conroy, Wear, 2009, **266**, 502-506.

6 D. Mansfield, *Proc. SPIE* 7101, Advances in Optical Thin Films III, 710101 (October 15, 2008).

7 F. Madani-Grasset, N. T. Pham, E. Glynos and V. Koutsos, Mater. Sci. Eng. B-Adv., 2008, **152**, 125-131.

8 P. M. Fredericks, in *Handbook of Vibrational Spectroscopy*, eds. J. M. Chalmers and P. R. Griffiths, John Wiley & Sons, Ltd., Chichester, 2002, vol. 2, pp. 1493-1507.

9 P. M. Fredericks, in *Vibrational Spectroscopy of Polymers: Principles and Practice*, eds. N. J. Everall, J. M. Chalmers and P. R. Griffiths, John Wiley & Sons, Inc., Hoboken, 2007, pp. 179-200.

10 N. J. Harrick, Phys. Rev. Lett., 1960, **4**, 224-226.

11 N. J. Harrick, J. Phys. Chem., 1960, **64**, 1110-1114.

12 N. J. Harrick, Ann. NY. Acad. Sci., 1963, **101**, 928-959.

13 N. J. Harrick, in *Internal Reflection Spectroscopy*, Interscience, New York, 1967.

14 A. J. Sommer, in *Modern Techniques in Applied Molecular Spectroscopy*, ed. F. M. Mirabella, Wiley-Interscience, New York, 1998, pp. 291-322.

15 N. J. Everall, Appl. Spectrosc., 2000, **54**, 773-782.

16 N. J. Everall, Appl. Spectrosc., 2000, **54**, 1515-1520.

17 N. Everall, J. Lapham, F. Adar, A. Whitley, E. Lee and S. Mamedov, Appl. Spectrosc., 2007, **61**, 251-259.

18 N. J. Everall, Appl. Spectrosc., 2009, **63**, 245A-262A.

19 T. Ikeshoji, Y. Ono and T. Mizuno, Appl. Opt., 1973, **12**, 2236-2237.

20 T. Takenaka and T. Nakanaga, J. Phys. Chem., 1976, **80**, 475-480.

21 D. A. Woods and C. D. Bain, Analyst, 2012, **137**, 35-48.

22 R. Iwamoto, M. Miya, K. Ohta and S. Mima, J. Chem. Phys., 1981, **74**, 4780-4790.

23 L. G. Tisinger, A. J. Sommer, in *Microscopy and Microanalysis*, 2004, vol. 10, pp. 1318-1319.

24 A. O. Kivioja, A. S. Jaaskelainen, V. Ahtee and T. Vuorinen, Vibr. Spectrosc., 2012, **61**, 1-9.

25 N. H. Fontaine and T. E. Furtak, Phys. Rev. B, 1998, **57**, 3807-3810.

26 Y. Levy, C. Imbert, J. Cipriani, S. Racine and R. Dupeyrat, Opt. Commun. 1974, **11**, 66-69.

27 J. F. Rabolt, R. Santo and J. D. Swalen, Appl. Spectrosc., 1979, **33**, 549-551.

28 J. F. Rabolt, R. Santo and J. D. Swalen, Appl. Spectrosc., 1980, **34**, 517-521.

29 J. F. Rabolt, N. E. Schlotter and J. D. Swalen, J. Phys. Chem., 1981, **85**, 4141-4144.

30 C. G. Zimba, V. M. Hallmark, S. Turrell, J. D. Swalen and J. F. Rabolt, J. Phys. Chem., 1990, **94**, 939-943.

31 D. R. Miller, O. H. Han and P. W. Bohn, Appl. Spectrosc., 1987, **41**, 245-248.

32 D. R. Miller, O. H. Han and P. W. Bohn, Appl. Spectrosc., 1987, **41**, 249-255.

33 P. W. Bohn, Trac-Tren. Anal. Chem., 1987, **6**, 223-233.

34 D. R. Miller and P. W. Bohn, Anal. Chem., 1988, **60**, 407-411.

35 D. R. Miller and P. W. Bohn, Appl. Opt., 1988, **27**, 2561-2566.

36 N. H. Fontaine and T. E. Furtak, J. Opt. Soc. Am. B, 1997, **14**, 3342-3348.

37 F. Ishizaki and M. Kim, Jpn. J. Appl. Phys., 2008, **47**, 1621-1627.

38 K. J. McKee and E. A. Smith, Rev. Sci. Instrum., 2010, **81,** 043106-1-043106-6.

39 M. W. Meyer, V. H. T. Nguyen and E. A. Smith, Vibr. Spectrosc., 2013, **65**, 94-100.

40 G. F. Schneider, V. E. Calado, H. Zandbergen, L. M. K. Vandersypen and C. Dekker, Nano. Lett., 2010, **10**, 1912-1916.

41 I. H. Malitson, J. Opt. Soc. Am., 1962, **52**, 1377-1379.

42 F. Ay, A. Kocabas, C. Kocabas, A. Aydinli and S. Agan, J. Appl. Phys., 2004, **96**, 7147-7153.

43 S. N. Kasarova, N. G. Sultanova, C. D. Ivanov and I. D. Nikolov, Opt. Mater., 2007, **29**, 1481-1490.

44 D. M. Sullivan, *Electromagnetic Simulation Using the FDTD Method*, IEEE Press, Piscataway, 2000.

45 K. S. Yee, IEEE Transactions on Antennas and Propagation, 1966, **14**, 302-307.

46 A. Palm, J. Phys. Chem., 1951, **55**, 1320-1324.

47 W. M. Sears, J. L. Hunt and J. R. Stevens, J. Chem. Phys., 1981, **75**, 1589-1598.

48 C. H. Jones and I. J. Wesley, Spectrochim. Acta A, 1991, **47**, 1293-1298.

49 B. H. Stuart and P. S. Thomas, Spectrochim. Acta A, 1995, **51**, 2133-2137.

50 S. N. Lee, V. Stolarski, A. Letton and J. Laane, J. Molec. Struct., 2000, **521**, 19-23.

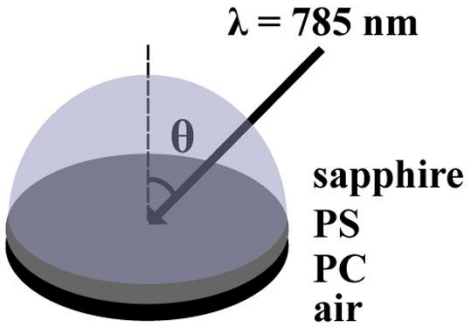

Fig. 1. Sample configuration of the bilayer polymer films measured using SA Raman spectroscopy. The incident angle, θ, of the 785-nm laser was varied from 55.70-65.70^{o} with Raman spectra collected every 0.05^{o}. Raman scattered light from the sample was collected from below the interface using a 10× (0.30 NA) objective.

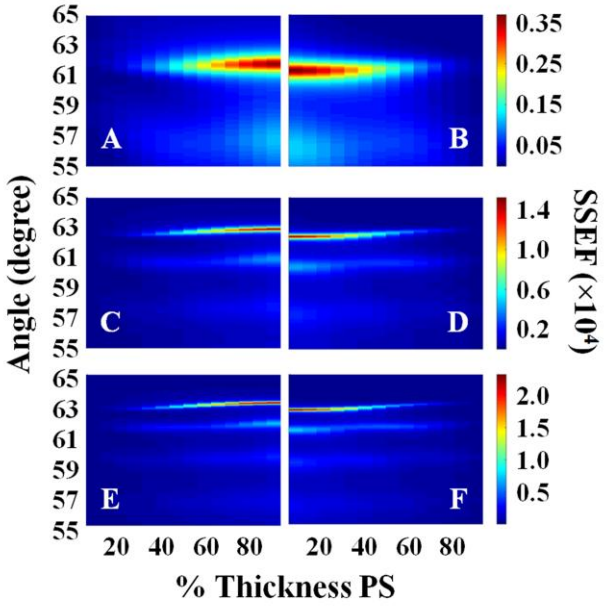

Fig. 2. Plots of the calculated MSEF versus interface location (% Thickness PS) and angle for films with total bilayer thicknesses of: (**A**, **B**) 1300 nm, (**C**, **D**) 2200 nm, and (**E**, **F**) 2700 nm. Plots **A**, **C**, and **E** represent the MSEF in the PS layer, and plots **B**, **D**, and **F** represent the MSEF in the PC layer. A schematic of the sample configuration used in the calculations is illustrated in Fig. 1.

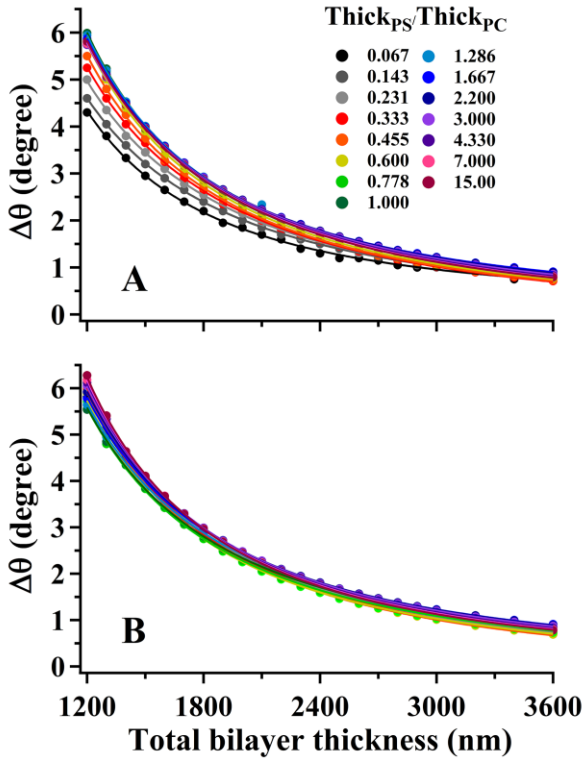

Fig. 3. Plots of angle difference between modes 0 and 1 (Δθ) in SSEF calculations of bilayer films for (**A**) PS and (**B**) PC as a function of the total bilayer thickness. Each curve represents a different buried interface location ($Thick_{PS}/Thick_{PC}$) from 0.067-15.00. The solid curves represent a power function fit to the data. The corresponding power fit functions are listed in Table 1.

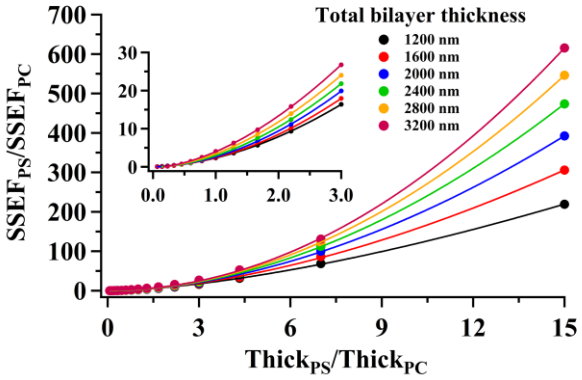

Fig. 4. Plots of the calculated ratio of $SSEF_{PS}/SSEF_{PC}$ corrected for the relative Raman cross-section as a function of the interface location ($Thick_{PS}/Thick_{PC}$) for selected total bilayer thicknesses. For clarity, not all generated data have been shown. The solid curves represent a power function fit to the data. The corresponding power fit functions for all curves are listed in Table 2.

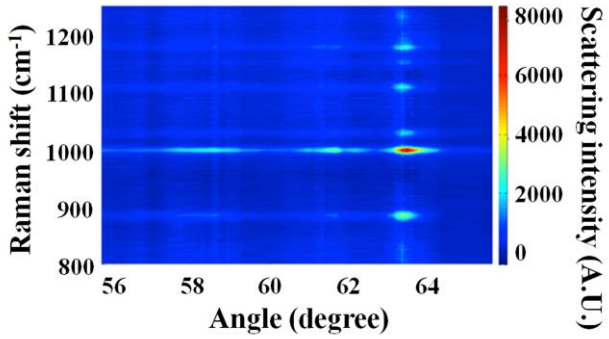

Fig. 5. Raman scattering intensity versus angle and Raman shift for a bilayer film consisting of 1070 nm PS and 1100 nm PC layers. Three waveguide modes were observed for both PS and PC within the selected angle region. Modes, 0, 1, and 2 for PS were located at 63.52º, 61.74º, and 58.40º. Modes 0, 1, and 2 for PC were located at 63.45º, 61.79º, and 58.28º. Only the most intense Raman transitions generated appreciable signal at modes 1 and 2.

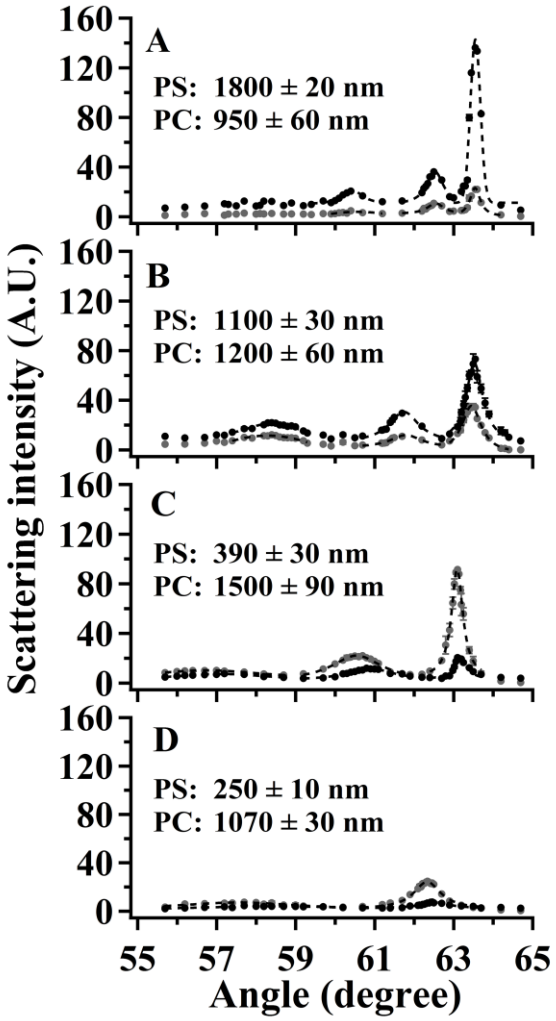

Fig. 6. SA Raman intensity for the 1001 cm^{-1} PS (black) and 889 cm^{-1} PC (gray) transitions as a function of angle for (**A**) sample 1, (**B**) sample 2, (**C**) sample 3, and (**D**) sample 4. The dashed lines represent Lorentzian fits for modes 0 and 1. The PS and PC film thicknesses for the samples, as measured by optical profilometry, are included in each spectrum.

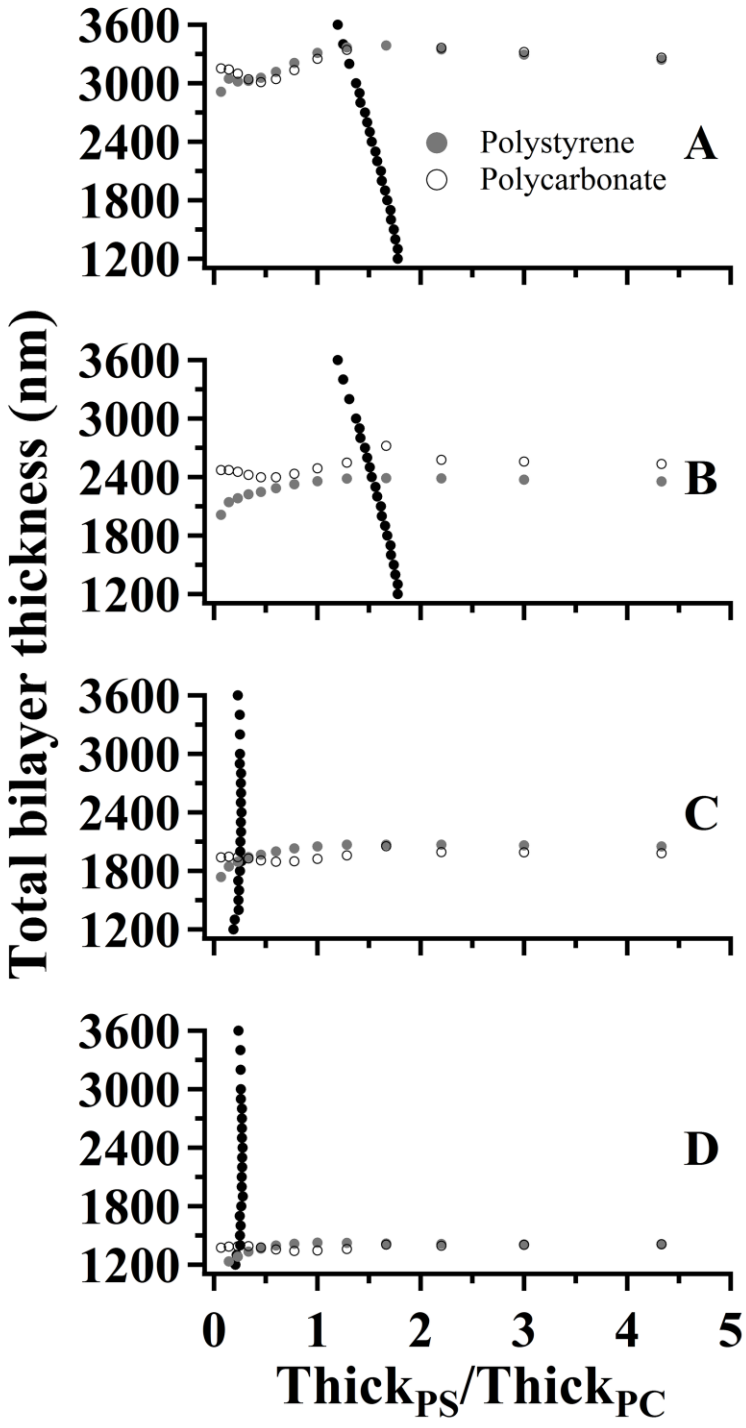

Fig. 7. Plots of total bilayer thickness versus interface location (Thick$_{PS}$/Thick$_{PC}$) constructed using the fit functions listed in Tables 1 and 2 and the SA Raman

spectroscopy data (Table 4) collected for: (**A**) sample 1, (**B**) sample 2, (**C**) sample 3, and (**D**) sample 4.

Table 1 Power fit functions for the curves shown in Fig. 3.

$\Delta\theta = \Delta\theta_0 + A(\Sigma t)^B$

Angle difference between modes 0 and 1 ($\Delta\theta$) and total bilayer thickness (Σt)

	Fig. 3A (PS)				**Fig. 3B (PC)**			
$\left(\frac{Thick_{PS}}{Thick_{PC}}\right)$	**$\Delta\theta_0$**	**A ($\times 10^6$)**	**B**	**RMSR[a]**	**$\Delta\theta_0$**	**A ($\times 10^6$)**	**B**	**RMSR[a]**
0.067	0.15	1.47	-1.80	0.04	-0.19	0.91	-1.68	0.01
0.143	-0.07	0.34	-1.58	0.02	-0.19	1.07	-1.70	0.01
0.231	-0.21	0.33	-1.56	0.03	-0.23	1.13	-1.71	0.02
0.333	-0.26	0.47	-1.60	0.02	-0.24	1.44	-1.74	0.01
0.455	-0.18	0.89	-1.69	0.02	-0.22	1.59	-1.76	0.02
0.600	-0.12	1.34	-1.74	0.02	-0.17	1.35	-1.74	0.02
0.778	-0.04	1.68	-1.77	0.02	-0.13	0.87	-1.68	0.03
1.000	0.07	2.50	-1.83	0.01	-0.07	0.78	-1.67	0.03
1.286	0.04	1.60	-1.76	0.03	-0.07	0.65	-1.64	0.02
1.667	0.04	1.35	-1.74	0.01	-0.07	0.69	-1.65	0.01
2.200	-0.06	0.81	-1.67	0.01	-0.07	0.85	-1.67	0.01
3.000	-0.13	0.65	-1.64	0.01	-0.07	1.16	-1.71	0.01
4.333	-0.16	0.70	-1.65	0.01	-0.08	1.48	-1.75	0.01
7.000	-0.18	0.74	-1.65	0.01	-0.09	1.85	-1.78	0.02
15.00	-0.16	0.94	-1.69	0.01	-0.07	2.43	-1.81	0.02

[a] Root mean square residual (RMSR) is the mean absolute value of the residuals (r), in which a smaller RMSR indicates a better fit. n is the number of data points.

$\text{RMSR}=\sqrt{\sum r^2 / n}$

Table 2 Best-fit functions for the curves shown in Fig. 4 when fitting a limited range of $\frac{Thick_{PS}}{Thick_{PC}}$.

$$\frac{Int_{PS}}{Int_{PC}} = \left(\frac{Int_{PS}}{Int_{PC}}\right)_0 + A\left(\frac{Thick_{PS}}{Thick_{PC}}\right)^B$$

$\left(\frac{Thick_{PS}}{Thick_{PC}}\right)$ **between 0.067 and 3**

Total thickness (nm)	$\left(\frac{Int_{PS}}{Int_{PC}}\right)_0$	**A**	**B**	**RMSR[a]**
1200	0.09	2.22	1.82	0.03
1300	0.09	2.19	1.84	0.05
1400	0.01	2.36	1.77	0.03
1500	0.04	2.28	1.85	0.02
1600	0.03	2.37	1.84	0.01
1700	0.05	2.32	1.88	0.06
1800	0.01	2.44	1.86	0.03
1900	-0.04	2.59	1.80	0.03
2000	-0.01	2.62	1.84	0.03
2100	-0.01	2.64	1.85	0.05
2200	-0.04	2.78	1.84	0.05
2300	-0.04	2.84	1.83	0.03
2400	-0.08	3.03	1.80	0.04
2500	-0.07	3.09	1.81	0.06
2600	-0.09	3.22	1.78	0.06
2700	-0.09	3.27	1.80	0.07
2800	-0.14	3.56	1.74	0.06
2900	-0.10	3.54	1.77	0.11
3000	-0.13	3.75	1.75	0.07
3200	-0.20	4.18	1.70	0.08
3400	-0.28	4.65	1.63	0.12
3600	-0.23	4.92	1.65	0.25

[a] Root mean square residual (RMSR) is the mean absolute value of the residuals (*r*), in which a smaller RMSR indicates a better fit. *n* is the number of data points.

RMSR= $\sqrt{\sum r^2 / n}$

Table 3 Summary of SA Raman spectroscopy results.

	$\Delta\theta$ (degree)		$\frac{R_{PS}}{R_{PC}}$ **at mode 0**	**Total bilayer thickness (nm)**		**PS thickness (nm)**	
	PS	PC		SA Raman spectroscopy[a]	% difference[b]	SA Raman spectroscopy[a]	% difference[b]
Sample 1	1.0 ± 0.1	1.0 ± 0.1	6.4 ± 0.7	3350 ± 10	19.7	1880 ± 10	4.3
Sample 2	1.8 ± 0.1	1.6 ± 0.1	1.8 ± 0.1	2380 ± 70	3.4	1040 ± 30	5.6
Sample 3	2.3 ± 0.1	2.5 ± 0.1	0.20 ± 0.01	1920 ± 20	1.6	390 ± 10	0.1
Sample 4	4.4 ± 0.3	4.6 ± 0.3	0.22 ± 0.01	1330 ± 80	0.8	250 ± 30	0.1

[a] Average of PS and PC determinations; uncertainties represent standard deviation
[b] Compared to optical profilometry values

CHAPTER 3:

CONCLUSION

This thesis presented the application of SA Raman spectroscopy for polymer thin film characterization. Previous work included in Appendix B and C provides the foundation of instrumentation and application of SA Raman analysis on single thin polystyrene films. Bilayer PS/PC films were prepared by the water transfer method to provide smooth interfaces. The total thickness of these PS/PC films ranges from 1300 to 2750 nm and the buried interface location ranges from 250 to 1880 nm. PS films of 1880 nm overlaps with confocal Raman spectroscopy's spatial resolution limit. Three-dimension FDTD-based calculations were performed to calculate the SSEF over each layer of a four-layer system. Calculations in combination with SA Raman experimental data allowed the buried PS/PC interface to be located, the total bilayer thickness to be determined, and the chemical composition to be obtained. The thicknesses calculated from this methodology are comparable to profilometry results. SA Raman spectroscopy is a nondestructive approach that offers at lease an order of magnitude improvement in axial spatial resolution compare to confocal Raman spectroscopy.

The future applications and limitations of SA Raman spectroscopy need to be further investigated, especially in complicated system consisting of more than two polymer layers. Developing models to characterize multilayer thin films with complicated interfaces is a challenge to overcome, so that the technique can be applied on a larger sample selection in real life thin film characterization.

APPENDIX A:
ENHANCED METAL LOADING IN SBA-15-TYPE CATALYSTS FACILITATED BY SALT ADDITION: SYNTHESIS, CHARACTERIZATION AND CATALYTIC ACTIVITY OF MOLYBDENUM INCORPORATED POROUS SILICA

A paper published in Apply Catalysis A: General.

Sridhar Budhi,[1,2] Chorthip Peeraphatdit,[1] Vy H. T. Nguyen,[1] Emily Smith,[1] Brian Trewyn[1,2]*

[1]Department of Chemistry, Iowa State University, Ames, IA 50011.
[2]Present address: Department of Chemistry and Geochemistry, Colorado School of Mines, Golden, CO 80401.

ABSTRACT

We report a novel method to increase the metal loading in SBA-15 silica matrix via direct synthesis. It was demonstrated through the synthesis and characterization of a series of molybdenum containing SBA-15 mesoporous silica catalysts prepared with and without diammonium hydrogen phosphate (DHP) as an additive. Catalysts prepared with DHP show a 2-3 times increase in incorporation of molybdenum in the silica matrix and pore size enlargement. The synthesized catalysts were characterized using nitrogen sorption, X-ray diffraction (XRD), Raman spectroscopy, scanning electron microscopy (SEM), transmission electron microscopy (TEM), X-ray photoelectron spectroscopy (XPS) and inductively coupled plasma – optical emission spectroscopy (ICP-OES). The catalytic activity of catalysts prepared with DHP for alcoholysis of epoxides was superior to that of the catalyst prepared without DHP. Alcoholysis

of epoxides was demonstrated for a range of alcohols and epoxides under ambient conditions in as little as 30 minutes with high selectivity.

INTRODUCTION

Mesoporous materials have gained momentum after the discovery of ordered mesoporous silicates (M41S) by scientists at Mobil Corporation[31] two decades ago. Since then it has gained global interest by addressing pressing problems of society such as energy and environment. Metal incorporated porous silica materials have been tested in applications such as catalysis[32], hydrogen energy[33], etc as efficient and reusable catalysts. The most comprehensively studied porous silica material for various applications (catalysis, host-guest chemistry, chromatographic separation) is MCM-41 since it has high specific surface area with uniform mesoporous channels[34]. However, small pore size and limited hydrothermal stability has limited its applications.

Stucky and coworkers[35] developed a new class of mesoporous silica called SBA-15 containing uniform cylindrical pores with tunable pore size (5 – 30 nm) and thick pore walls using environmentally benign non-ionic block copolymers as structure-forming templates under strong acidic conditions. However, unlike MCM-41-type synthesis, incorporation of metal ions in the framework of this mesoporous silica support for downstream applications is challenging because of strong acidic synthetic conditions. The highly acidic synthetic conditions of SBA-15 are detrimental for incorporation of metal ions through co-condensation[36] as it breaks the Si-O-metal bond. Additionally, under SBA-15 synthetic conditions, highly solubilized metal ions fail to precipitate and incorporation in the silica framework is not effective. Thus, post-synthetic grafting[37] is the widely used technique for doping metal ions in SBA-15 framework. Owing to

these difficulties there have only been a few reports in the literature for direct incorporation of metal ions in SBA-15 framework. Vinu and coworkers[38] have optimized the synthetic conditions to synthesize SBA-15 under relatively low acidic conditions for improved incorporation of metal ions. It was later determined that metal incorporation efficiency was better under these less acidic conditions[39].

Improvements and tailoring of mesoporous silica for specific applications are often done by adding additives to the reaction mixture. Hydrocarbons added during the synthesis of mesoporous materials influences average pore size, crystallinity and pore size distribution[40]. Addition of inorganic salts is another approach to modify the textural properties of mesoporous silica. Addition of salts such as $MgCl_2$, $Ni(CH_3COO)_2$, and $Mg(CH_3COO)_2$ increased the periodicity of mesophase structure as demonstrated by Wang et al[41.] Enlargement of the average pore size was observed when NaCl was added to reaction mixture when Kramer et al.[42] synthesized cubic *Ia3d* mesoporous silica. Tunable morphologies were reported by employment of K_2SO_4 and Na_2SO_4 by the Stucky and Zhao research groups[43]. Despite these advancements, to the best of our knowledge, there are no literature reports for the role of salts in dictating the incorporation of metals in a silica matrix.

Epoxidation, one of the most studied reactions in the literature, is of academic and industrial importance. It is a valuable intermediate to yield a range of products with applications in the pharmaceutical, polymer and agrochemical industries through regioselective ring opening. Nucleophiles such as alcohols, amines, cyanides, hydroxides, halides to name a few, can open epoxides. Ring opening of epoxides by alcohols (alcoholysis) yields β-alkoxyalcohols, which are precursors for mandelic acid and antibacterial agents including β-lactam antibiotics. Ring opening of epoxides are chemically cleaved by acid or base catalysts under elevated

temperatures. In addition to acids and bases, several metal ions such as Al(III), Sn(II), Sn(IV), Co(III), triflates, Cr(III), and Lewis acid supported metal-organic frameworks were recently reported as catalysts for ring opening of epoxides[44]. However, these catalysts are either toxic, less abundant in nature, involve complex preparatory procedures for synthesis, energy-intensive or require prolonged reaction times.

Next to titanium, molybdenum is the most studied transition metal through incorporation into silica matrix due to its wide catalytic applications. Molybdenum is widely studied in oxidation reactions, petroleum chemistry[45] and recently in the conversion of biomass into renewable energy[46]. A few examples of reactions catalyzed by molybdenum are epoxidation of olefins[47], decomposition of NO_x[48], hydrodeoxygenation, hydrodenitrogenation, hydrodesulfurization, alkane oxidation[49], oxidative dehydrogenation[50], metathesis[51] and transesterification[52]. To the best of our knowledge, there has been only two reports where Mo was used to study the ring opening of epoxides on alumina support[53]. However, their studies failed to distinguish whether the catalytic activity was due to Mo or Al(III) ions on the support. Graham et al.[54] demonstrated ring opening of epoxides using aluminosilicates where Al(III) was the active catalyst. Thus, the reports of catalytic activity by molybdenum on alumina for ring opening of epoxides could potentially be due to the presence of both molybdenum and alumina. These reports clearly indicate that participation of supports on catalytic activity cannot be ignored.

Mo incorporated SBA-15 is often prepared by post-synthesis impregnation and grafting rather than direct synthesis due to poor metal incorporation. Apart from highly acidic conditions, the oxidation state of molybdenum ions (+6) make isomorphic substitution by Si (+4)

challenging. Thus, we need a comprehensive preparatory procedure for direct synthesis of metal incorporated SBA-15. Herein, for the first time, we report the synthesis of Mo-SBA-15 through co-condensation using DHP as an additive added in the reaction mixture. Addition of DHP was found to influence the incorporation of molybdenum along with other textural properties. These catalysts were successfully tested for alcoholysis under ambient conditions for a wide range of alcohols

EXPERIMENTAL

Materials:

Ammonium heptamolybdate tetrahydrate [$(NH_4)_6Mo_7O_{24}\cdot 4H_2O$] and diammonium hydrogen phosphate [$(NH_4)_2HPO_4$, DHP] were purchased from Fisher Chemicals were used as the molybdenum precursor and additive, respectively. Triblock copolymer poly(ethylene glycol)-block-poly(propyleneglycol)-block-poly(ethylene glycol) (Pluronic P123, MW = 5800, $EO_{20}PO_{70}EO_{20}$, Aldrich) was used as the structure-directing template. Tetraethylorthosilicate (Aldrich) was used as the silica source for the synthesis of SBA-15. HCl (2 M) solution was prepared from 37 wt % HCl purchased from Fisher Chemical. All epoxides and alcohols tested for catalytic activity were purchased from Fisher and Aldrich. All reagents were used as received without further purification.

Synthesis of Molybdenum incorporated SBA-15 catalyst: In a typical synthesis, 4 g of pluronic P123 was added to 30 mL nanopure water in a polypropylene bottle at 313 K and stirred at 600 rpm for 3 h. A solution of previously mixed HCl (2 M, 10, mL) in 60 mL of water was also added to the dissolved template solution and stirred for another 1 h. TEOS (9 g, 4.3 mmol)

was added drop wise to the reaction mixture, followed by quick addition of the required amount of ammonium heptamolybdate tetrahydrate. The samples were labeled as Xg-Mo-SBA-15-TTT. Xg denotes amount of molybdenum precursor added and TTT represents the hydrothermal treatment temperature in degrees Celsius. For the syntheses that involved addition of the additive, diammonium hydrogen phosphate, labels were Xg-MoP-SBA-15-TTT, where Xg is the amount in grams of molybdenum and DHP added and TTT as defined above. In cases where different amounts of molybdenum precursor and DHP were added it was denoted by XgP-YgMo-SBA-15-TTT where Xg and Yg is amount of DHP and molybdenum precursor in grams respectively. Whenever the additive was included, it was added along with the molybdenum precursor. After addition of all components, the reaction mixture was stirred for another 24 h at 313 K and then subjected to hydrothermal treatment at the desired temperature for an additional 48 h. The reaction mixture was cooled, filtered and washed with methanol and water. The resulting sample was oven dried overnight at 373 K and then followed by calcination at 550 ^{o}C for 8 h to remove the template in presence of flowing air.

Characterization:

X-ray diffractograms (XRD) of synthesized samples were recorded utilizing a Rigaku Ultima (IV) diffractometer using Cu Kα radiation source. The diffractograms were recorded from 0.5° to 10° with a step size of 0.02°. Wide angle XRD were recorded for certain samples from 20° to 80° at a rate of 1°/min. Surface analyses of samples to determine surface area and pore sizes were measured utilizing nitrogen sorption analysis in a Micromeritcs ASAP 2020 analyser. The samples were degassed for 6 h at 373 K prior to measurements. The Brunauer-Emmett-Teller (BET) and the Barrett-Joyner Halenda (BJH) equations were used to calculate

specific surface area and pore size distributions, respectively. Transmission Electron Microscopy (TEM) imaging was done using a Tecnai F^2 microscope. Particle morphology was determined by Scanning Electron Microscopy (SEM) using a Hitachi S4700 FE-SEM system with 10 kV accelerating voltage. Raman spectra were collected using a previously described instrument with 785 nm excitation and a 10×, 0.3 numerical aperture objective to collect the Raman scatter[55]. The laser power at the sample was 6 mW for Mo samples or 64 mW for MoP samples. Spectra were collected with a 30 second acquisition, and were background subtracted using a spectrum collected with no sample in the sample holder. XPS was used to characterize the oxidation states of Mo in the catalysts on a Perkin–Elmer PHI 5500 XPS spectrometer with a position sensitive detector, a hemispherical energy analyzer in an ion-pumped chamber evacuated to 2×10^{-9} Torr (267×10^{-9} Pa)], and an AlKα (binding energy = 1486.6 eV) X-ray source at 300 W with a 15 kV acceleration voltage. Metal loading was quantified on a Perkin Elmer ICP-OES model Optima 2100DV. Approximately 5 mg of catalyst was dissolved in 10 ml aliquot of 500 mL solution prepared from mixing 50 µl of 36 % HF and 500 µl of aqua regia.

Catalytic Studies:

In a typical experiment, a 20 mL sample vial was charged with a certain amount of desired catalyst followed by 1.1 mmol of epoxide and 3 mL of alcohol. The reaction was stirred using magnetic stir bar at ambient temperature (396 K +/- 2K). The reaction mixture was withdrawn at regular intervals and injected into a gas chromatograph (HP 5890, FID detector and DB-5 capillary column) to monitor the progress of the reaction. Reactant conversion was calculated with respect to epoxide since alcohols were used in excess as the solvent and nucleophile.

RESULTS AND DISCUSSION:

X-ray diffraction measurements:

Figure 1 shows the XRD of Mo incorporated SBA-15 samples containing different amounts of molybdenum with and without DHP. Samples synthesized with 0.25 g molybdenum precursor with and without DHP [Fig 1: (a)] shows (100), (110), and (200) reflections characteristic of SBA-15 as described by Zhao *et al*[35]. The sample synthesized with DHP with 0.25 g of molybdenum precursor shows an additional reflection (210) indicating higher degree of periodicity. However, (100), (110), and (200) reflections are observed in the sample containing 0.5 g of molybdenum precursor without DHP, while the corresponding sample with DHP has a broad, unresolved reflection of representing superimposed (110) and (200) patterns apart from an intense (100) reflection. Samples containing 1 g of molybdenum precursor with and without DHP has a (100) reflection while low intense peaks are not clearly observed suggesting a loss in periodicity with increased amounts of molybdenum precursor and DHP during synthesis. When 2 g of molybdenum precursor was added without DHP a complete loss of structure was observed by XRD, while the XRD of the corresponding sample with DHP suggests that it has undergone a phase transformation similar to *Ia3d* structure since it has reflections (211) and (200) similar to MCM-48[56]. This supports a report by Flodstrom *et al*. that suggests the addition of salt to SBA-15 synthesis can induce phase transformation to *Ia3d*[57]. The XRD peak intensity of all samples with DHP was greater than samples without DHP indicating that the inclusion of salt brings greater pore uniformity. Similar observations were made by Newalker *et al*. when they synthesized salt added silica SBA-15[58]. The d_{100} reflection of samples with DHP appeared at lower 2θ than without DHP except for samples with the greatest amount of added molybdenum

(2g-MoP-SBA-15 and 2g-Mo-SBA-15-100) indicating that adding DHP increases pore size. All the synthesized samples were subjected to high angle X-ray diffraction analysis between 20^{o}-80^{o}. All samples prepared without DHP gave spectra that correspond to the background for amorphous silica irrespective of molybdenum loading. For the samples prepared with DHP, one sample (1g-MoP-SBA-15-100) gave peaks (2θ = 23.4, 25.8 and 27.5), which are characteristic for molybdenum trioxide in an orthorhombic phase as previously reported in the literature[59]. However, the 2g-Mo-SBA-15-100 sample, despite the increased molybdenum loading lacked the peaks characteristic for molybdenum trioxide.

Textural properties

Nitrogen physisorption isotherms of samples synthesized with and without DHP are seen in Figure 2. Table 1 summarizes textural properties of all synthesized materials along with metal loading and incorporation efficiency. All synthesized samples except for 2g-Mo-SBA-15 have type (IV) adsorption isotherm characteristic of mesoporous materials according to IUPAC classification and H1 type broad hysteresis loop typical for large pore mesoporous solids. The amount of nitrogen adsorbed for samples prepared without DHP decreased with increasing amount of metal precursor indicating that the surface area decreased with increasing addition of metal precursor. However, for the samples prepared with DHP the amount of nitrogen adsorbed decreased until 1g-MoP-SBA-15 and further increases in metal precursor did not result in increased metal incorporation and led to increased surface area. Surface area values of samples are inverse to the amount of molybdenum incorporated in the final catalyst. The amount of metal incorporated in samples synthesized with DHP are 2-3 times greater than the corresponding samples synthesized without salt additive. Hence, surface area of samples prepared with DHP is

less than the corresponding samples synthesized without DHP. Increasing hydrothermal temperature during synthesis decreased the molybdenum loading, however the surface area was not measurably affected. The metal loading wt % for samples synthesized under different hydrothermal temperatures with and without DHP was only marginally affected. In an effort to understand the role of DHP in metal loading, we synthesized three additional samples varying the added salt amount (0.25 g P, 0.5 g P and 1.5 g P) while keeping the amount of molybdenum precursor constant. The surface area of 1g-Mo-SBA-15-100 dropped from 628 m^2g^{-1} to 441 m^2g^{-1} when 0.25 g of DHP was added during synthesis which led to increased metal loading (Table 1). When the DHP amount was increased to 1 g the metal incorporation reached 12.8 wt % and the surface area decreased to 229 m^2g^{-1} and further addition of DHP led to a drop in metal loading and an increase in surface area. In general, of the samples we synthesized it was generally observed that increased metal loading led to a decrease in surface area.

Except for 2g-Mo-SBA-15-100, all other samples that we synthesized, we observed a steep rise in the nitrogen physisorption isotherm at a relative pressure of 0.6 indicating a narrow pore size distribution. The reported pore sizes in Table 1 are based on BJH calculations. Pore diameter increased with increasing hydrothermal temperature and amount of metal loading except for 2g-Mo-SBA-15-100 for samples prepared without DHP. The 2g-MoP-SBA-15-100 has very low pore volume and small pore size, which is different than the trend observed for the rest of the samples, potentially due to pore blocking caused by excessive metal loading. However, there is no clear trend in pore sizes between samples synthesized with DHP as we observed with samples prepared without DHP. Interestingly, the pore sizes for samples containing similar amounts of metal precursor prepared with DHP are larger than samples prepared without DHP.

Raman Studies:

Raman studies were performed for samples synthesized with a 373 K hydrothermal treatment with and without DHP. Representative Raman spectra for samples synthesized without DHP are shown in Figure 3. Samples with low metal loading and small particle sizes did not show any discernible Raman peaks potentially due to low metal loading or highly dispersed metal species in the silica matrix. Peaks at 910, 847, and 704 cm^{-1} correspond to the presence of ammonium heptamolybdate (data not shown)[39]. The absence of peaks in any of the analyzed samples (Figure 3) indicates that there is no unreacted metal precursor present and polymolybdate ions were completely converted to monomeric molybdenum species. The lines characteristic of α-MoO_3 in Raman spectra are 161, 285, 293, 339, 381, 666, 819 and 996 cm^{-1}[60]. In one sample, 2g-Mo-SBA-15-100, intense lines corresponding to α-MoO_3 at 996, 819 and 667 cm^{-1} were observed. The peak at 996 cm^{-1} corresponds to terminal ν(Mo=O) of MoO_3 and the peak at 819 cm^{-1} refers to $\nu(OMo_2)$. The peak at 667 cm^{-1} corresponds to $\nu(OMo_3)$[61]. Similar lines were observed for 1g-MoP-SBA-15-100 with more intensity than 1g-Mo-SBA-15-100 since it has higher metal loading (data not shown).

XPS Analyses:

To support the Raman data, XPS analysis was performed to determine the oxidation state of molybdenum. Molybdenum generally exists as Mo (IV) and Mo (VI) oxides. Molybdenum in (+4) oxidation state has a binding energy of 230.1 eV and molybdenum in MoO_2 has binding energy of 229.2 eV corresponding to the Mo $3d_{5/2}$ electron. XPS results of both 1g-MoP-SBA-15-100 (not shown) and 1g-Mo-SBA-15-100 (Fig. 4) shows peaks with binding energies of

232.7 and 235.8 eV corresponding to Mo $3d_{5/2}$ and $3d_{3/2}$ electrons, respectively. These values are in agreement with previously reported values in the literature or molybdenum in a trioxide form[62]. Even though these two peaks are observed as a doublet characteristic of Mo, the resolution of doublet is poor possibly due to low amounts of molybdenum loading in the silica support. Poor resolution for molybdenum on silica support was also reported previously[63]. The binding energy for Si 2p orbital was observed at 103.08 eV and O 1s orbital has binding energy of 532.6 eV[64]. The binding energy of O 1s corresponds to its silica environment. No second peak for oxygen at 530.6 eV corresponding to MoO_3 was observed indicating that no change occurred in the silica environment due to molybdenum loading even at 13 wt % and molybdenum is monatomically dispersed on the support.

Scanning electron microscopy (SEM) images of the series of silica supported Mo catalysts (different Mo loadings and with and without DHP) can be seen in the supporting information. It appears that the amount of Mo loading and the presence or absence of DHP does not affect the morphology of the catalysts, all catalysts appear to have a typical SBA-15 morphology. The transmission electron microscopy (TEM) images of Mo-SBA-15 and MoP-SBA-15 catalysts shown in Figure 5 reveal the highly ordered pore structure of each of the catalysts, regardless of the Mo loading or the presence or absence of DHP. Additionally, energy dispersive X-ray (EDX) spectroscopy results show the presence of Mo and Si when a single catalyst particle was analyzed (supporting information). This suggests a homogeneous mixture of Mo and Si within individual particles.

Catalytic Studies:

The catalytic activity of molybdenum incorporated SBA-15 catalysts prepared with and without DHP was investigated. First, we studied the alcoholysis of cyclohexene oxide with ethanol using catalysts containing different molybdenum loadings prepared with and without DHP. The general reaction is shown in Scheme 1 and the selectivity and turnover frequency (TOF) are tabulated in Table 2. Initially, we studied activity of catalysts prepared without DHP. It was observed that the TOF decreased with increasing molybdenum content. The selectivity of the desired product was above 95 % in all cases. The catalyst in entry 4 took two hours to reach 98 % conversion, nearly twice the time the catalyst in entry 3 took, despite the greater molybdenum loading in the former. Longer reaction times could be explained by poor diffusion of reactants and products due to the significantly decreased pore size and volume for the catalyst in entry 4. Reactions using catalysts prepared with DHP followed the same trend as without DHP of decreasing TOF (entries 5-7), except for entry 8 when the TOF increased. The TOF values for catalysts prepared with DHP were larger than catalysts prepared without DHP. This increased TOF suggests that these catalysts have more accessible catalytic sites than those prepared without DHP. The increased TOF of entry 8 was possibly due to decreased molybdenum loading and more accessible catalytic centers. Reaction times were reduced by more than half using catalysts prepared with DHP. Other alcoholysis reports[65] of cyclohexene oxide under ambient conditions in 30 minutes are limited. Once we confirmed that the catalysts prepared with DHP have better catalytic activity than catalysts prepared without DHP, we conducted further experiments using catalysts prepared with DHP. We investigated the alcoholysis using catalysts prepared under different hydrothermal treatments (entries 7, 9, and 10). Results indicate that with increasing hydrothermal treatment the TOF increased, however the reaction time and

selectivity has typically the same for these three catalysts. Further catalytic studies were carried out using the catalyst in entry 10 because of its superior performance. Slightly higher TOF of the catalyst in entry 8 may be due to different silica phases as is suggested in XRD analysis, more investigation in this is needed. As a control, we have carried out reactions using just silica (entry 11) without molybdenum and no conversion of starting material was observed for 2 h. To verify the influence of salt on catalytic activity, we synthesized a catalyst with only DHP and no molybdenum precursor. These prepared materials have no effect in catalysis (entry 11 & 12) suggesting that catalytic activity was exclusively due to molybdenum in the silica support.

Different alcohols were evaluated for alcoholysis with cyclohexene oxide as one substrate and 1g-MoP-SBA-15-150 as the catalyst under ambient conditions and results are presented in Table 3. Primary alcohols up to five-carbon chain length under went 100 % conversion with high selectivity for the expected product in 30 min. With further increase in carbon chain length (entry 6-10) it took longer reaction times to achieve conversions of less than 100 %, however; the selectivity remains fairly constant. Unsaturated primary alcohols such as crotyl alcohol and allyl alcohol had reactivities similar to short chained, saturated alcohols, however, the selectivity of crotyl alcohol was very low. Aralkyl alcohols such as benzyl alcohol and 2-phenylethanol had typical activities similar to small chain, saturated alcohols with high conversion and selectivity. A secondary alcohol, 2-propanol, converted completely to the corresponding ether but the bulkier cyclohexanol took twice the time as 2-propanol for 98 % conversion. Tertiary alcohols were found to have the poorest reactivity of all the alcohols towards the cyclohexene oxide. For example, only 75% of the *t*-butyl alcohol converted to the corresponding ether in 1 h with poor selectivity (75 %). The low reactivity for *t*-butyl alcohol is likely due to the hydroxyl group being sterically hindered by alkyl groups. This hypothesis was

strengthened further when reactivity was dropped further from 75 % to 32 % when one of the methyl groups was replaced by an ethyl group (*t*-amyl alcohol) and selectivity too decreased from 75 % to 65 %. The poor reactivity of tertiary alcohols has been observed elsewhere[66]. Despite the poor reactivity of tertiary alcohols, the conversion we observed is better than previous reports in terms of kinetics[66].

We extended our catalytic studies further to study ethanol ring opening with different epoxides as shown in Table 4. Styrene oxide, cyclohexene oxide and epichlorohydrin have gone to 100 % completion in just 30 minutes with selectivity greater than 90 %. Except for cyclohexene oxide, the rest of the epoxides tested are asymmetrical with the possibility of two products. All previous reports in the literature for asymmetrical epoxide ring opening agree that solid acid catalysts will cleave the epoxide ring in such a way to yield a more stable carbocation followed by attack of the alcohol to form alkoxyalcohols. Our selectivity results for different epoxides predominantly give the expected alkoxyalcohols consistent with the mechanism of epoxide ring opening solid acid catalysts at very high ratio.

Recycling studies:

Recycling studies for ring opening of epoxide using cyclohexene oxide as the substrate and ethanol as the nucleophile. The experiment was repeated four times and the conversions are 100, 82, 60 and 30 %, respectively. The molybdenum loaded in the catalyst was reduced from 8.5 wt % to 6 wt % as determined by ICP-AES analysis after 4 cycles. The surface area decreased from 329 $m^2 g^{-1}$ to 214 $m^2 g^{-1}$ and pore volume decreased from 1.2 to 0.716 $cm^3 g^{-1}$, however pore diameter remained the same. The decrease in pore volume can be attributed to clogging of the pore channels by reaction species in the mixture. It has been reported in

literature that metal incorporated on silica support leaches for a variety of reasons including reaction parameters such as solvent, temperature, polarity of reactants, etc[67]. Alcohols, especially smaller carbon chain ones that are highly polar in nature, are reported to facilitate leaching of metal ions supported on silica. In our case, probably alcohols that we use may be a source of metal leaching. However, a detailed investigation is required to conclude if leaching is substrate specific or due to polarity of alcohols used as nucleophiles, since we used only ethanol in our recyclability experiments.

CONCLUSIONS

We have successfully synthesized molybdenum incorporated SBA-15 by direct synthesis using diammonium hydrogen phosphate as an additive. Addition of diammonium hydrogen phosphate increased the pore size of the materials. Most importantly, for the first time, we have observed that the addition of a salt facilitates the incorporation of metal on silica support by 2-3 times more than the corresponding catalysts synthesized without DHP. However, we have limited our investigation to just one additive and its effect on loading. The catalyst we synthesized was used for effective ring opening of epoxides in a short amount of time at ambient temperature for a wide range of alcohols and epoxides. We are currently investigating the applicability of additive enhanced metal loading for different metal incorporated SBA-15, different pH and range of additives and its influence in metal loading and catalytic activity.

REFERENCES

[1] C.T. Kresge, M.E. Leonowicz, W.J. Roth, J.C. Vartuli, J.S. Beck, Nature. 359 (1992) 710-712.

[2] H. Subramanian, E.G. Nettleton, S. Budhi, R.T. Koodali, Journal of Molecular Catalysis A: Chemical. 330 (2010) 66-72.

[3] D. Zhao, S. Budhi, A. Rodriguez, R.T. Koodali, International Journal of Hydrogen Energy. 35 (2010) 5276-5283.

[4] A. Chenite, Y. Le Page, A. Sayari, Chemistry of Materials. 7 (1995) 1015-1019.

[5] D. Zhao, J. Feng, Q. Huo, N. Melosh, G.H. Fredrickson, B.F. Chmelka, G.D. Stucky, Science. 279 (1998) 548.

[6] Z. Luan, E.M. Maes, P.A.W. van der Heide, D. Zhao, R.S. Czernuszewicz, L. Kevan, Chemistry of Materials. 11 (1999) 3680-3686.

[7] Z. Luan, M. Hartmann, D. Zhao, W. Zhou, L. Kevan, Chemistry of Materials, American Chemical Society, 1999, pp. 1621-1627.

[8] A. Vinu, V. Murugesan, W. Böhlmann, M. Hartmann, The Journal of Physical Chemistry B. 108 (2004) 11496-11505.

[9] J.A. Melero, J. Iglesias, J.M. Arsuaga, J. Sainz-Pardo, P. de Frutos, S. Blazquez, Applied Catalysis A: General. 331 (2007) 84-94.

[10] S. Budhi, H.S. Kibombo, D. Zhao, A. Gonshorowski, R.T. Koodali, Materials Letters. 65 (2011) 2136-2138.

[11] Y. Wang, B. Zibrowius, C.-m. Yang, B. Spliethoff, F. Schuth, Chemical Communications (2004) 46-47.

[12] E. Krämer, S. Förster, C. Göltner, M. Antonietti, Langmuir. 14 (1998) 2027-2031.

[13] C. Yu, B. Tian, J. Fan, G.D. Stucky, D. Zhao, Journal of the American Chemical Society. 124 (2002) 4556-4557.

[14] C. Yu, J. Fan, B. Tian, D. Zhao, Chemistry of Materials. 16 (2004) 889-898.

[15] B.M. Reddy, M.K. Patil, B.T. Reddy, S.-E. Park, Catalysis Communications. 9 (2008) 950-954.

[16] E. Laurent, B. Delmon, Industrial & Engineering Chemistry Research. 32 (1993) 2516-2524.

[17] V.M.L. Whiffen, K.J. Smith, Energy & Fuels. 24 (2010) 4728-4737.

[18] C.D. Nunes, A.A. Valente, M. Pillinger, A.C. Fernandes, C.C. Romao, J. Rocha, I.S. Goncalves, Journal of Materials Chemistry. 12 (2002) 1735-1742.

[19] S. Higashimoto, R. Tsumura, M. Matsuoka, H. Yamashita, M. Che, M. Anpo, in: C.C. A. Gamba, S. Coluccia (Eds.), Studies in Surface Science and Catalysis, Elsevier, 2001, pp. 315-321.

[20] L.-X. Dai, Y.-H. Teng, K. Tabata, E. Suzuki, T. Tatsumi, Microporous and Mesoporous Materials. 44–45 (2001) 573-580.

[21] P.S. Raghavan, M.P. Vinod, Journal of Molecular Catalysis A: Chemical. 135 (1998) 47-53.

[22] P. Topka, H. Balcar, J. Rathouský, N. Žilková, F. Verpoort, J. Čejka, Microporous and Mesoporous Materials. 96 (2006) 44-54.

[23] T.M. Sankaranarayanan, A. Pandurangan, M. Banu, S. Sivasanker, Applied Catalysis A: General. 409–410 (2011) 239-247.

[24] S. Ramesh Kumar, P. Leelavathi, Journal of Molecular Catalysis A: Chemical. 266 (2007) 65-68.

[25] S. Singhal, Chemistry Letters. 37 (2008) 620.

[26] M.W.C. Robinson, D.A. Timms, S.M. Williams, A.E. Graham, Tetrahedron Letters. 48 (2007) 6249-6251.

[27] C.-J. Shih, E.A. Smith, Analytica Chimica Acta. 653 (2009) 200-206.

[28] B. Boote, H. Subramanian, K.T. Ranjit, Chemical Communications (2007) 4543-4545.

[29] K. Flodström, V. Alfredsson, N. Källrot, Journal of the American Chemical Society. 125 (2003) 4402-4403.

[30] B.L. Newalkar, S. Komarneni, Chemistry of Materials. 13 (2001) 4573-4579.

[31] X. Ma, J. Gong, S. Wang, N. Gao, D. Wang, X. Yang, F. He, Catalysis Communications. 5 (2004) 101-106.

[32] S.B. Umbarkar, T.V. Kotbagi, A.V. Biradar, R. Pasricha, J. Chanale, M.K. Dongare, A.-S. Mamede, C. Lancelot, E. Payen, Journal of Molecular Catalysis A: Chemical. 310 (2009) 150-158.

[33] L. Seguin, Spectrochimica acta. Part A, Molecular and biomolecular spectroscopy. 51 (1995) 1323.

[34] S.L.T. Andersson, R.F. Howe, The Journal of Physical Chemistry. 93 (1989) 4913-4920.

[35] B. Zhou, S. Ceckiewicz, B. Delmon, The Journal of Physical Chemistry. 91 (1987) 5061-5067.

[36] C.V. Cáceres, J.L.G. Fierro, J. Lázaro, A. López Agudo, J. Soria, Journal of Catalysis. 122 (1990) 113-125.

[37] H. Seyama, M. Soma, Journal of the Chemical Society, Faraday Transactions 1: Physical Chemistry in Condensed Phases. 81 (1985) 485-495.

[38] M.W.C. Robinson, R. Buckle, I. Mabbett, G.M. Grant, A.E. Graham, Tetrahedron Letters. 48 (2007) 4723-4725.

[39] S. Das, T. Asefa, ACS Catalysis. 1 (2011) 502-510.

[40] Y. Deng, C. Lettmann, W.F. Maier, Applied Catalysis A: General. 214 (2001) 31-46.

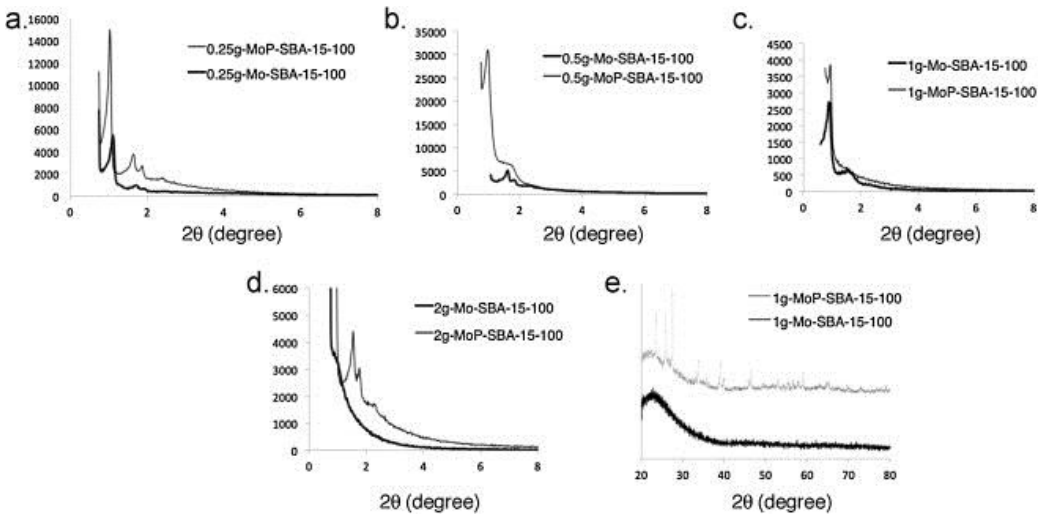

Fig. 1. Powder XRD patterns of SBA-15 samples prepared in the presence and absence of additives with (a) 0.25 g, (b) 0.5 g, (c) 1 g, (d) 2 g, and (e) 1 g (wide angle) of molybdenum precursor. The spectra in (e) are offset for clarity.

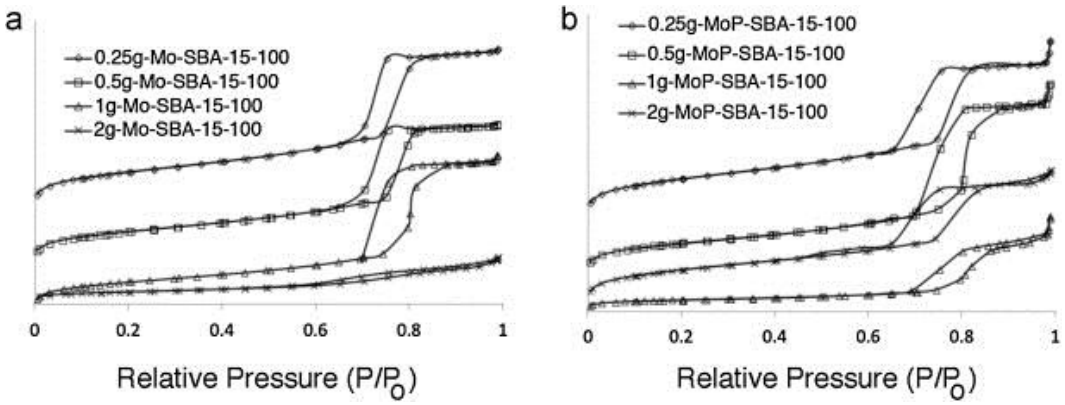

Fig. 2. Nitrogen sorption isotherms of metal incorporated SBA-15 with different amounts of molybdenum precursor in (a) absence of additives, (b) presence of additives. Spectra are offset on the *y* -axis for clarity.

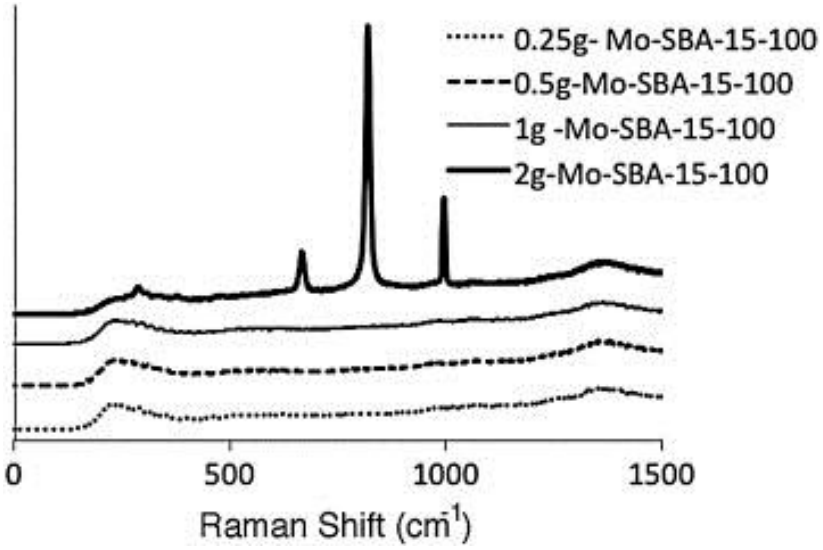

Fig. 3. Raman spectra of molybdenum incorporated SBA-15 samples with different amounts of loading without additive. Spectra are offset on the *y* -axis for clarity.

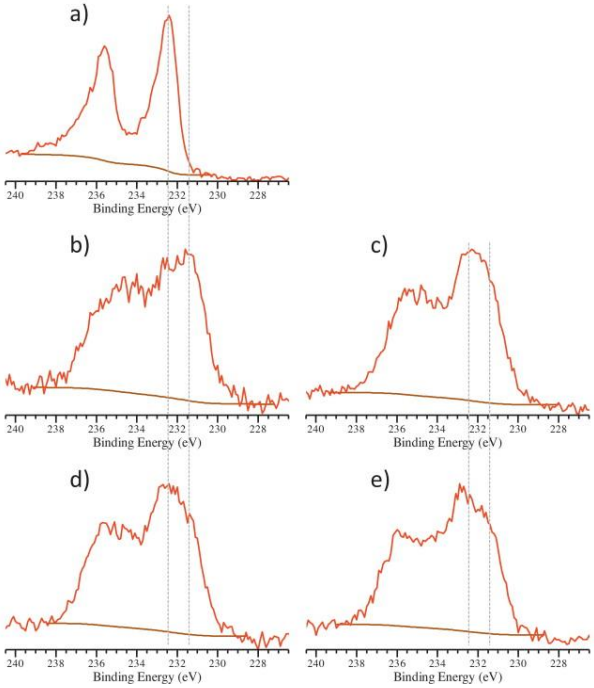

Fig. 4. High resolution XPS of Mo 3d spectra (a) 0.25g-Mo-SBA-15-100, (b) 0.25g-MoP-SBA-15-100, (c) 0.5g-MoP-SBA-15-100, (d) 1g-MoP-SBA-15-100, and (e) 2g-MoP-SBA-15-100.

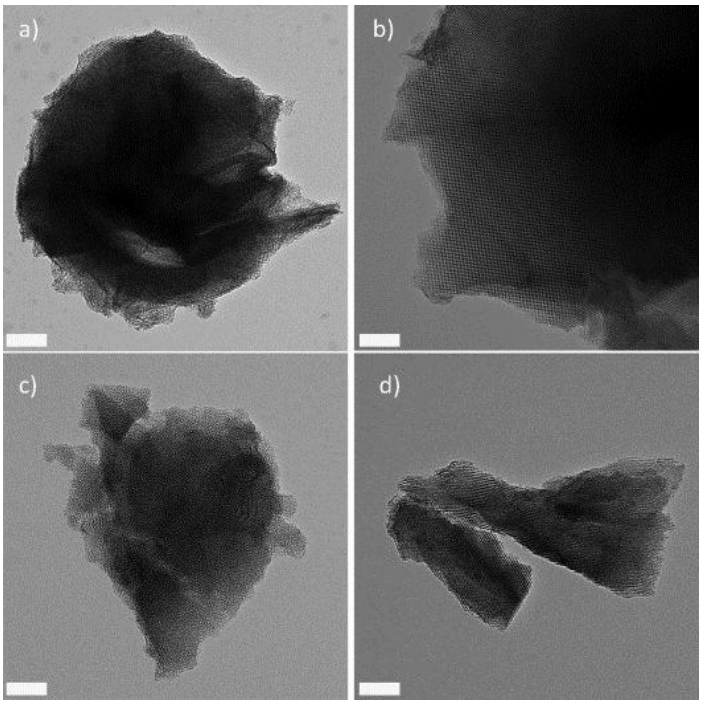

Fig. 5. Transmission electron micrographs (TEM) of Mo and MoP SBA-15 catalysts: (a) 1.0g-MoP-SBA-15-100, (b) 0.5g-MoP-SBA-15-100, (c) 1.0g-Mo-SBA-15-100, and (d) 0.5g-Mo-SBA-15-100. All scale bars represent 200 nm.

SCHEME

Scheme 1 General alcoholysis reaction catalyzed by Mo-SBA-15.

TABLES

Table 1. Textural properties of Mo incorporated SBA-15 samples prepared in presence and absence of additives.

Sample name	Si/Mo (added)	Si/Mo (Expt)	Metal loading (wt%)	Loading efficiency (%)	Surface area (m^2/g)	Pore volume (cm^3/g)	Pore diameter (nm)
0.25g-Mo-SBA-15-100	36.7	437	1.1	11.9	875	1.3	8.6
0.5g-Mo-SBA-15-100	18.3	150	3.3	17.3	744	1.1	8.8
1g-Mo-SBA-15-100	9.2	107	4.5	12.1	628	1.3	10
1g-Mo-SBA-15-130	9.2	165	4	10.7	480	1.2	10.9
1g-Mo-SBA-15-150	9.2	127	3.8	10.2	367	1.2	11
2g-Mo-SBA-15-100	6.1	26	18.8	24.3	234	0.4	7.6
0.25g-MoP-SBA-15-100	36.7	149	3.3	35	804	1.2	9
0.5g-MoP-SBA-15-100	18.3	81	6.1	32.3	590	1.3	10.7
1g-MoP-SBA-15-100	9.2	38	12.8	33.9	227	0.8	10.2
1g-MoP-SBA-15-130	9.2	44	11.1	29.4	246	1	12
1g-MoP-SBA-15-150	9.2	57	8.5	22.5	329	1.2	10.7
2g-MoP-SBA-15-100	6.1	113	4.4	4.3	694	0.9	9
0.25gP-1gMo-SBA-15-100	9.2	42	11.4	30.1	441	1	7.4
0.5gP-1gMo-SBA-15-100	9.2	43	11.3	30	408	0.9	9
1.5gP-1gMo-SBA-15-100	9.2	52	9.4	24	552	0.9	9.2

Table 2. Alcoholysis of cyclohexene oxide with ethanol catalyzed by catalyst synthesized under different hydrothermal treatments and containing different amounts of molybdenum.

Entry	Catalyst	Catalyst amount (mg)	Molybdenum mol% by substrate	Time (min)	Conv (%)	Sel (%)	TOF (h^{-1})[a]
1	0.25g-Mo-SBA-15-100	20	0.2	120	72	96	123
2	0.5g-Mo-SBA-15-100	20	0.6	120	98	95	58
3	1g-Mo-SBA-15-100	20	0.8	60	92	96	45
4	2g-Mo-SBA-15-100	20	3.4	120	98	96	10
5	0.25g-MoP-SBA-15-100	20	0.6	45	92	95	142
6	0.5g-MoP-SBA-15-100	20	1.1	45	96	94	82
7	1g-MoP-SBA-15-100	20	2.4	30	100	95	60
8	2g-MoP-SBA-15-100	20	1	30	100	96	88
9	1g-MoP-SBA-15-130	23	2.4	30	100	95	70
10	1g-MoP-SBA-15-150	30	2.4	30	100	95	90
11	1g-P-SBA-15-100	20	NA	120	0	0	NA
12	Si-SBA-15-100	20	NA	120	0	0	NA

APPENDIX B:
SCANNING ANGLE RAMAN SPECTROSCOPY MEASUREMENTS OF THIN POLYMER FILMS FOR THICKNESS AND COMPOSITION ANALYSES

A paper published in Vibrational Spectroscopy.

*Matthew Meyer,[1,2] Vy H.T. Nguyen[1,2], Emily A. Smith[1,2]**

[1]Ames Laboratory, U. S. Department of Energy, Ames, Iowa 50011-3111, and [2]Department of Chemistry, Iowa State University, Ames, Iowa 50011-3111

ABSTRACT

Scanning angle (SA) Raman spectroscopy was used to measure the thickness and composition of polystyrene films. A sapphire prism was optically coupled to a sapphire substrate on which 6–12% (w/v) polystyrene in toluene was spin coated. Raman spectra were collected as the incident angle of the p-polarized, 785-nm excitation laser was varied from 56 to 70°. These angles span above and below the critical angle for a sapphire/polystyrene interface. The thickness of the polystyrene film was determined using a calibration curve constructed by calculating the integrated optical energy density distribution as a function of incident angle, distance from the prism interface and polymer thickness. The calculations were used to determine the incident angle where waveguide modes are excited within the polymer film, which is the angle with the highest integrated optical energy density. The film thicknesses measured by SA Raman spectroscopy ranged from less than 400 nm to 1.8 μm. The average percent uncertainty in the SA Raman determinations for all films was 4%, and the measurements agreed with those obtained from optical interferometery within the experimental uncertainty for all but two films. For the 1270-nm and 580-nm polystyrene

films, the SA Raman measurements overestimated the film thickness by 5 and 18%, respectively. The dependence of the calibration curve on excitation polarization and composition of the polymer and bulk layers was evaluated. This preliminary investigation demonstrates that scanning angle Raman spectroscopy is a versatile method applicable whenever the chemical composition and thickness of interfacial polymer layers needs to be measured.

INTRODUCTION

Interest in the analysis of polymer films continues to grow due to their importance in optics, energy storage and capture devices, microelectronics and the coatings industry [1] and [2]. Popular optical methods for measuring polymer film thickness include ellipsometry and optical interferometry [3] and [4]. Like most optical measurements, these methods are non-invasive. However, they do not provide chemical content information. Optical methods that have the ability to provide combined polymer thickness with chemical specificity at an interface have been mostly limited to attenuated total reflection infrared (ATR IR) and total internal reflection (TIR) Raman spectroscopy [5], [6], [7], [8] and [9]. The penetration depth of the evanescent wave does not vary significantly across the spectrum in TIR Raman spectroscopy since a single excitation wavelength is used. On the other hand, the penetration depth does vary across the infrared spectrum, which complicates ATR IR data analysis. In addition to providing chemical content information, TIR Raman spectroscopy has the benefits of non-invasiveness, speed, limited sample preparation provided the sample can be optically coupled to a prism and the ability to study air, water or organic interfaces.

In TIR Raman experiments the illuminating laser light is directed onto a prism/analyte interface. Total internal reflection occurs when the incident angle is above the critical angle for the interface, and an evanescent wave that spatially extends into the sample is generated. TIR Raman spectroscopy is becoming a well-established technique for surface sensitive measurements of polymers, plants, and chemical surfactants [10], [11], [12] and [13]. TIR Raman spectroscopy has previously been used to analyze thin polymer films [5], [8], [14], [15], [16], [17], [18] and [19]. Kivioja et al. analyzed polystyrene on polypropylene films at a single incident angle that was greater than the critical angle [8]. The penetration depth of the evanescent wave under TIR limits the sample thicknesses that can be measured in these experiments. The thickest polystyrene sample studied was ~300 nm, and the TIR Raman spectroscopy result did not show good agreement with the thickness measured by other optical techniques. However, good agreement was achieved in the 40- to 250-nm thickness range. Varying the incident angle of excitation can provide more information about the sample. Fontaine and Furtak measured the Raman signal from a prism/polymer/air interface at varying incident angles [15] and [20]. Their results showed that the intensity of the Raman signal as a function of incident angle could be used to extract the polymer thickness, as further outlined below. Their study was limited to a single 1200 nm film, and they did not present a simple model that could easily be extended to other samples.

Integrated optical waveguides that are approximately the thickness of the excitation wavelength can increase the path length of light by a few orders of magnitude due to multiple total internal reflections within a dielectric [21]. This principle underlies a number of waveguide-based spectroscopies [22] and [23]. In order to confine the incident light in the

dielectric layer the refractive indices of the surrounding media must be lower than the refractive index of the dielectric ($\eta_1 < \eta_2$,dielectric $> \eta_3$). Radiative or "leaky" waveguides can occur at the interface when $\eta_1 > \eta_2$, dielectric $> \eta_3$ [20]. The optical energy density distributed through the dielectric exhibits an interference pattern at select incident angles at the radiative waveguide interface. There are substantial optical energy density enhancements at angles where constructive interference occurs, and this depends on the thickness of the dielectric layer, among other factors. In the present study scanning angle Raman spectroscopy was used to analyze homogeneous polystyrene films of different thickness. A simple model for extracting polymer thickness was developed by modeling optical energy density enhancements integrated over the entire polymer film at different incident angles and polymer thicknesses. The experimentally determined incident angle producing the largest Raman signal has been compared to incident angles where waveguide modes are predicted based on the electric field simulations. The goal of this work is to show the benefits of using scanning angle Raman spectroscopy over other optical-based measurements in the analysis of polymer films. The results from this study show facile scanning angle Raman spectroscopy measurements display high signal-to-noise ratio spectra that provide combined polymer thickness with tens of nanometer spatial resolution and chemical composition information.

EXPERIMENT SECTIONS:

Film Preparation.

All chemicals were purchased from Sigma–Aldrich, St. Louis, MO. Polystyrene pellets (molecular weight 280,000) were dissolved in analytical grade toluene at 12, 10, 9, 7, 6, or 4% (w/v). Two hundred microliters of the polymer solution were coated onto a 25.4-

mm sapphire disc (Meller Optics, Providence, RI) using a KW-4A spin coater (Chemat Technology, Northridge, CA). The films were coated at 3000 RPM for 60 s and dried overnight at room temperature. Film thicknesses were confirmed using a F20 thin film measurement system (Filmetrics, San Diego, CA) in transmission mode. The root-mean-square surface roughness measured by tapping mode atomic force microscopy of the 10 and 5% (w/v) polystyrene films were 1.6 nm and 0.3 nm, respectively. The root-mean-square surface roughness of the sapphire substrate was 0.8 nm. The atomic force microscopy scan size for all roughness measurements was 25 μm × 25 μm.

Sample Configuration.

The scanning angle Raman spectroscopy sample configuration is represented in Fig. 1. A sapphire prism was used for all measurements. A custom-made flow cell was designed to hold the hemispherical prism and sapphire substrate on which the polymer films were coated. Immersion oil (Cargille Labs, Cedar Groove, NJ, $\eta = 1.780$) was used to ensure optical contact between the prism and substrate. During each experiment careful attention was paid to ensure the immersion oil layer was not compromised. The flow cell was cleaned before each experiment by sonication and then dried with a stream of N2 gas.

Instrumentation.

Raman experiments were performed using a previously described scanning angle Raman microscope, which is capable of recording Raman spectra in the incident angle range of 34.5–74.0° [24]. Briefly, the 785 nm, narrow wavelength output laser was directed onto a variable angle mirror mounted onto a motorized translational stage. The beam was focused

using a lens mounted on a separate motorized translational stage. The variable angle mirror directs the incident light onto the prism/sample interface that is centered on an inverted microscope. A 1280 × 1024 CMOS camera mounted in the front port of the microscope is used to align and focus the laser beam at the sample interface. The reflectivity was collected using a 1 cm^2 photodiode mounted on a third vertically oriented motorized translational stage opposite the variable angle mirror and focusing lens. The Raman scatter was collected with a 10× magnification, 0.30 NA long working distance objective and sent onto a f/1.8i imaging spectrometer fitted with a 1340 × 400 pixel near-infrared enhanced CCD. The motorized translational stages and reflectivity were controlled though an in-house developed program with Labview 8.6.

The excitation power was set to 210 mW at the prism and the acquisition time was 60 s per spectrum. The polarization of the incident light was controlled with a polarizer and a half-wave plate to deliver s- or p-polarized light to the sample interface. The reflected light intensity from a sapphire/water interface was collected to calibrate the incident angles by modeling the data with Fresnel calculations using a program developed in IGOR Pro 6.1 that allows the incident angle spread to be varied [25] and [26].

Data Analysis.

Peak areas and intensities for the measured Raman bands were calculated by fitting them to a Gaussian curve with the "multipeak fitting 2" algorithm in IGOR Pro 6.1. Signal-to-noise ratios (S/N) were calculated as the maximum of the 1001 cm^{-1} peak intensity after background subtraction divided by the standard deviation of the noise measured from 920 to 950 cm^{-1} in a region of the spectrum where no analyte peaks were present. A 3-D finite-

difference-time-domain (FDTD)-based simulation (EM Explorer, San Francisco, CA) was used to calculate the optical energy density distribution at the interface. The calculations assumed all layers had a constant index of refraction and were homogeneous. The indices of refraction used for the calculations were: sapphire prism ($\eta_{\text{p-polarization}} = 1.764$, $\eta_{\text{s-polarization}} = 1.753$), polystyrene ($\eta = 1.578$) and air ($\eta = 1.000$). With the angular resolution used in these experiments, no difference in the polystyrene index of refraction was measured with p- or s-polarized light.

RESULTS AND DISCUSSIONS

Enhancement of the scanning angle Raman signal at the thin polymer-air interface.

The goals of this work are to experimentally measure and theoretically model the Raman scatter produced from radiative waveguides consisting of thin polystyrene films as a function of incident angle, and to develop a simple model for measuring polymer thickness in the 400 nm to 2 μm range. The first step is to analyze the Raman spectrum of polystyrene under different excitation conditions, including the scanning angle Raman sample geometry shown in Fig. 1. Fig. 2 shows the bulk Raman spectrum of solid (i.e., not cast as a thin film) polystyrene (black), the scanning angle Raman spectrum of a 580-nm polystyrene film at an angle lower than the sapphire/polystyrene critical angle (light gray) and an angle higher than the critical angle (dark gray). In all spectra, peaks representative of polystyrene are present. The aromatic ring breathing (1001 cm^{-1}), C—H bending (1032 cm^{-1}), ring deformation (620 cm^{-1}), and C=C aromatic ring stretching (1602 cm^{-1}) modes are the most intense bands [27]. The two additional peaks in the scanning angle Raman spectra at 645 and 750 cm^{-1} are from the sapphire prism. Comparing the bulk spectrum and the scanning angle

Raman spectra in Fig. 2, differences in the relative peak intensity are present. The peak intensity depends on the depolarization ratio of the peak and the excitation polarization, as previously discussed [24].

While the conventional backscattering configuration provides chemical information generated from the bulk material, it lacks the sensitivity to measure thin films. The spectrum shown in the inset to Fig. 2 was collected using the 580-nm polystyrene film and a backscattering configuration. Unlike the scanning angle Raman spectra in the same figure, no peaks were recorded despite measuring the same polystyrene thickness. The scanning angle Raman spectra at an incident angle of 60.0° (Fig. 2, light gray) and 64.1° (Fig. 2, dark gray) exhibit signal enhancement relative to probing the same amount of analyte using a traditional backscattering geometry. With an incident angle spread of 0.5° the critical angle for a sapphire/polystyrene interface is 63.8°. The background subtracted Raman intensity is 10.7-fold higher at 60.0° compared to 64.1°, and this is explained by the optical energy density enhancements when waveguide modes are excited in the film. The S/N ratios of the scanning angle Raman spectra are 119 and 16.3 above and below the sapphire/polystyrene critical angle, respectively.

Raman signal pattern at different incident angles and excitation polarization.

Fig. 3 shows 2D plots of Raman signal as a function of Raman shift and incident angle for a 950-nm polystyrene film with (a) s-polarized or (b) p-polarized excitation. It is evident from the plots that the Raman signal is higher at certain incident angles below the 63.8° sapphire/polystyrene critical angle. Cross sections of the 1001 cm^{-1} peak at different incident angles are shown in the figure insets. The angle where the Raman signal is the most

intense depends on the excitation polarization and polymer thickness. The angle producing the most intense Raman scatter is 60.4° or 60.6° for s- or p-polarized excitation, respectively. These angles are in good agreement to the maximum values predicted by integrating the calculated optical energy density over the entire film thickness (solid lines in Fig. 3 inset). At angles higher than the 63.8° sapphire/polystyrene critical angle, the collected Raman scatter decays as expected, and is less intense than at lower angles where waveguide modes are excited [28].

The number of intense peaks in the Raman spectra varies for s- and p-polarized excitation (Fig. 3). The p-polarized spectra exhibit intense peaks at 1602, 1181, 1151 and 1001 cm^{-1}. In contrast, only the 1001 cm^{-1} peak has significant intensity in the s-polarization spectra. The peaks that only have an appreciable intensity with p-polarized excitation are depolarized bands; while the 1001 cm^{-1} peak is a polarized band. Despite only one intense peak in the spectra, the background subtracted 1001 cm^{-1} peak area is 2.4-fold higher with s- compared to p-polarized excitation. All data that follows were collected using p-polarized excitation since the S/N was sufficient, and more peaks could be analyzed across the spectra. Although separate calculations would be required to model the Raman signal, either p- or s-polarized excitation (or both) could be used to collect the Raman scatter. The benefit of using both polarizations is that additional details about the structure and orientation of the polymer may be obtained by the polarization dependence of the Raman signal.

Calculated electric field distribution and integrated optical field intensity for different polystyrene thicknesses.

In order to determine the incident angle where waveguide modes are excited for interfaces containing different polystyrene thicknesses, calculations were performed for films ranging from 200 nm to 2 μm. A subset of the calculated data is shown in Fig. 4. The right panel shows 2D plots of the integrated optical energy density as a function of distance from the prism interface, with the interface designated at the distance 1000 nm, over a 58–66° incident angle range. This angle range was selected for a majority of the polymer thicknesses to minimize computing time, and was extended down to 54° for films less than 600 nm thick. The 2D electric field distribution plot can be used to determine angles where waveguide modes are excited and specific locations within the polymer film where the bulk of the Raman signal is generated. Waveguide enhancements require polymer films with thicknesses greater than ~250 nm using 785-nm excitation. Fig. 4f represents a 200-nm polystyrene film. Within the analyzed angle range, no discernible waveguide pattern can be observed, and the majority of the Raman signal is predicted to come from the polystyrene in contact with the sapphire substrate. In contrast, films with a thickness greater than a few hundred nanometers exhibit a more complex spatial distribution, and a majority of the Raman signal will be generated in approximately the middle of the film, away from the interfaces. The surface sensitivity is limited using angles below the sapphire/polystyrene critical angle. Experimentally the only Raman signal generated is from the polystyrene film since the semi-infinite air layer used in the measurements does not produce a Raman signal.

The optical energy density integrated over the entire film thickness is directly related to the predicted intensity of the Raman scatter [18]. The left panel in Fig. 4 displays the

integrated optical energy density generated from the entire polystyrene film over the incident angle range from 58 to 66°. Films with a thickness of a few hundred nanometers up to approximately 1200 nm have a single maximum calculated in this incident angle range, while films thicker than 1200 nm exhibit two or more maxima. In cases where multiple waveguide modes are present, only the mode at the largest incident angle was considered. For example, the peak maximum of the 950-nm radiative waveguide is at 60.4° (Fig. 4c) and the right-most peak maximum of the 1850-nm polystyrene film is at 62.8° (Fig. 4a).

Calculated angular shifts in the radiative waveguide's integrated optical energy density maxima can be compared to experimental angular shifts in the intensity of the Raman scatter to determine the polymer film thicknesses. These shifts can indicate thickness changes on the nanometer level. Calculated values predict a 0.10° shift between a 1230 nm film and 1200 nm film that can be detected with experimental data of sufficient S/N and similar angular resolution.

A calibration curve was constructed using the calculated integrated optical energy density maxima for polymer thicknesses in the 400 to 2 μm range (Fig. 5). Thinner films, down to ~250 nm could be included in the calibration curve. This would require extending the incident angle range of the calculations, which would increase calculation times as discussed above. Similarly, thicker films could be included in the calibration plot. As the polymer thickness increases, the interference pattern as a function of incident angle becomes more complex, and this requires analyzing the sample at higher angular resolution. In this case, experimental time would increase. The calibration points were fit with a double exponential curve $y = (30.6 \cdot e0.049x) + (1.44 \times 10{-}13 \cdot e0.585x)$ to an R^2 value of 0.9899. The minimum in the residual plot is at a thickness of 1200 nm and the maximum is at 2 μm. The

predicted percent uncertainties at these thicknesses are −4 and 3%, respectively, and the maximum expected percent uncertainty is ~5% for 400 nm films.

Experimental determination of polymer waveguide thickness.

Fig. 6 shows the area of the 1001 cm-1 polystyrene peak for the indicated incident angles and six polystyrene films fabricated by spin coating 4–12% (w/v) polystyrene in toluene onto sapphire substrates. Spectra were collected every 0.4° for most interfaces, and no lower than 0.25° or higher than 0.5° for all interfaces. The experimental Raman scatter plots were fit to a Gaussian curve to determine the angle corresponding to the maximum intensity. An example fit is shown in the inset to Fig. 6c. Similar to the calculated plots shown in Fig. 4, as the thickness of the polystyrene films decreases, the Raman scatter versus incident angle plot broadens and the incident angle that produces the maximum Raman scatter shifts to lower incident angles. The experimental data show distinct maxima for all but the 4% (w/v) polystyrene films, and multiple waveguide modes are recorded for the 12% (w/v) polystyrene film within this incident angle range. The overall Raman intensity increases as the polymer thickness increases, which is consistent with probing more polymer.

The polystyrene film thickness was calculated using the angle that produced the most intense Raman scatter from the Gaussian fit and the fit equation obtained from the calibration. The results are shown for all the films in Fig. 7. The uncertainty in the scanning angle Raman measurements ranges from 1.6 to 6.7%. Also shown in this figure are the thicknesses determined using optical interferometry for films fabricated using the same spin coating procedure. The values obtained by scanning angle Raman spectroscopy are well correlated to the optical interferometer measurements, and in all but two cases the values

reported for the two methods agree within the experimental uncertainty. For the 1270-nm and 580-nm films, the SA Raman measurements overestimated the film thickness by 5 or 18%, respectively. The average difference between the optical interferometry and SA Raman spectroscopy results is 6.9%. Some of this difference is the result of having to analyze different films by the two techniques. Altering the thickness range of the calibration plot used for the SA Raman measurements did not significantly alter the average difference obtained by the two methods. The ability to probe several incident angles with scanning angle Raman spectroscopy allows thickness measurements of polystyrene films ranging from 2 μm to less than 400 nm. When combined with traditional total internal reflection Raman measurements using the same sample geometry shown in Fig. 1, the range could decrease to ~50 nm [8]. Since the spectral S/N ratio is lower at angles above the critical angle, acquisition times need to be longer than those used for these experiments.

The measured signal enhancement in the scanning Raman geometry depends on the medium adjacent to the polymer film (i.e., Fig. 1, medium 3). Although the analyses were performed using air as the third medium, water or organic solvents can in principle be used provided the integrity of the polymer film is not compromised. In order to understand how this will affect the Raman signal, the integrated optical energy density was calculated for water ($\eta_3 = 1.329$) or organic ($\eta_3 = 1.700$) layers. At the sapphire/2-μm polystyrene film/medium 3 interface, the Raman scatter is expected to be 0.7-times (organic) or 0.3-times (water) lower compared to the value measured in air, but the constructive interface pattern as a function of varying incident angle is expected to be the same to at least 0.4° angular resolution. This means the calibration curve shown in Fig. 5 is valid for these conditions and interfaces with other η_3 layers.

CONCLUSION

A scanning angle Raman spectroscopy calibration curve for determining radiative polymer waveguide thickness with p-polarized, 785-nm excitation was constructed. The calibration curve will be suitable for any polymer with a similar index of refraction to that of polystyrene, and similar methods can be used to construct a calibration for polymers of other indices of refraction, excitation wavelengths or polarizations. The optical energy density distribution as a function of incident angle and distance from the prism interface can be used to determine the spatial dependence of the Raman signal, which is primarily generated from the center of the polymer film when the thickness is more than ~250 nm. The success of the presented approach is dependent on the incident angle resolution and the spectral S/N. Sixty-second acquisition times were used to collect each Raman spectrum every 0.25–0.5° within the range 56–70°. These conditions were sufficient for close agreement to an independent method for determining polymer thickness in the 400 nm to 2 μm range. While the reported uncertainty of the SA Raman spectroscopy thickness measurements is slightly higher than that of optical interferometry for many of the samples, longer acquisition times or averaged accumulations, and higher angular resolution measurements will reduce the uncertainty. The presented method will have utility for many applications where both polymer thickness and chemical content need to be measured, especially with stacked polymer layers.

ACKNOWLEDGEMENTS

This research is supported by the U.S. Department of Energy, Office of Basic Energy Sciences, Division of Chemical Sciences, Geosciences, and Biosciences through the Ames Laboratory. The Ames Laboratory is operated for the U.S. Department of Energy by Iowa State University under Contract No. DE-AC02-07CH11358.

REFERENCES

[1] L. Eldada, L.W. Shacklette, IEEE J. Sel. Top. Quant. 6 (2000) 54–68.

[2] Y. Wang, A. Hongo, Y. Kato, T. Shimomura, D. Miura, M. Miyagi, Appl. Opt. 36 (1997) 2886–2892.

[3] Y. Ebata, A.B. Croll, A.J. Crosby, Soft Matter (2012) 9086–9091.

[4] A. Knoll, R. Magerle, G. Krausch, J. Chem. Phys. 120 (2004) 1105–1116.

[5] N.A. Nikonenko, O.N. Tretinnikov, J. Appl. Spectrosc. 75 (2008) 878–882.

[6] P. Yang, X.F. Meng, Z.Y. Zhang, B.X. Jing, J. Yuan, W.T. Yang, Anal. Chem. 77 (2005) 1068–1074.

[7] L.J. Fina, Appl. Spectrosc. Rev. 29 (1994) 309–365.

[8] A.O. Kivioja, A.S. Jaaskelainen, V. Ahtee, T. Vuorinen, Vib. Spectrosc. 61 (2012) 1–9.

[9] M.W. Meyer, K.J. McKee, H.T. Nguyen, E.A. Smith, J. Phys. Chem. C 116 (2012) 24987–24992.

[10] R. Iwamoto, K. Ohta, M. Miya, S. Mima, Appl. Spectrosc. 35 (1981) 584–587.

[11] D.A. Woods, C.D. Bain, Analyst 137 (2012) 35–48.

[12] F. Ishizaki, M. Kim, Jpn. J. Appl. Phys. 47 (2008) 1621–1627.

[13] K.J. McKee, M.W. Meyer, E.A. Smith, Anal. Chem. 84 (2012) 9049–9055.

[14] J.T. Ives, W.M. Reichert, J. Appl. Polym. Sci. 36 (1988) 429–443.

[15] N.H. Fontaine, T.E. Furtak, J. Opt. Soc. Am. B 14 (1997) 3342–3348.

[16] N.E. Schlotter, J.F. Rabolt, Appl. Spectrosc. 38 (1984) 208–211.

[17] N.E. Schlotter, J.F. Rabolt, J. Phys. Chem. 88 (1984) 2062–2067.

[18] C.G. Zimba, V.M. Hallmark, S. Turrell, J.D. Swalen, J.F. Rabolt, J. Phys. Chem. 94 (1990) 939–943.

[19] D.R. Miller, O.H. Han, P.W. Bohn, Appl. Spectrosc. 41 (1987) 245–248.

[20] N.H. Fontaine, T.E. Furtak, Phys. Rev. B 57 (1998) 3807–3810.

[21] J.T. Bradshaw, S.B. Mendes, S.S. Saavedra, Anal. Chem. 77 (2005) 28a–36a.

[22] I. Chabay, Anal. Chem. 54 (1982) 1071–1080.

[23] A. Abbas, M.J. Linman, Q. Cheng, Sens. Actuators B 156 (2011) 169–175.

[24] K.J. McKee, M.W. Meyer, E.A. Smith, Anal. Chem. 84 (2012) 4300–4306.

[25] W.N. Hansen, J. Opt. Soc. Am. 58 (1968) 380–388.

[26] S.N. Kasarova, N.G. Sultanova, C.D. Ivanov, I.D. Nikolov, Opt. Mater. 29 (2007) 1481–1490.

[27] R.L. McCreery, Raman Spectroscopy for Chemical Analysis, Wiley-Interscience, New York NY, 2000, p. 263.

[28] K.J. McKee, E.A. Smith, Rev. Sci. Instrum. 81 (2010), 043106-043106-043106.

FIGURES

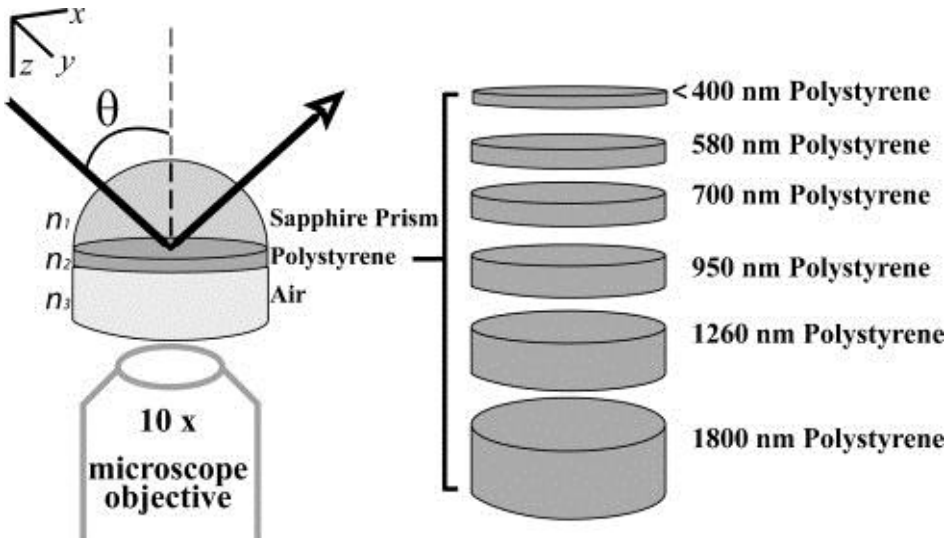

Fig. 1. Schematic of the scanning angle Raman spectroscopy sample geometry used to measure polystyrene film thicknesses. The incident angle (θ) of the excitation light at the interface is varied from 56 to 70° in approximately 0.4° increments while simultaneously collecting Raman spectra.

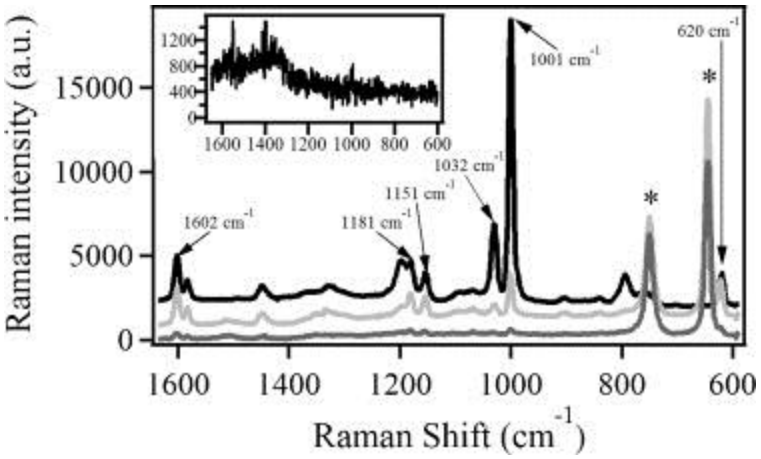

Fig. 2. Bulk Raman spectrum of solid polystyrene (black) collected using the traditional 180° backscattering Raman spectroscopy geometry. Scanning angle Raman spectra of a thin 580-nm polystyrene film collected with an incident angle of 60.0° (light gray) and 64.1° (dark gray). The critical angle for a sapphire/polystyrene interface is 63.8°. The peaks from the sapphire prism are marked with an asterisk (*). Inset: Raman spectrum of the same 580-nm polystyrene film measured with the traditional 180° backscattering configuration. All spectra were collected using p-polarized excitation.

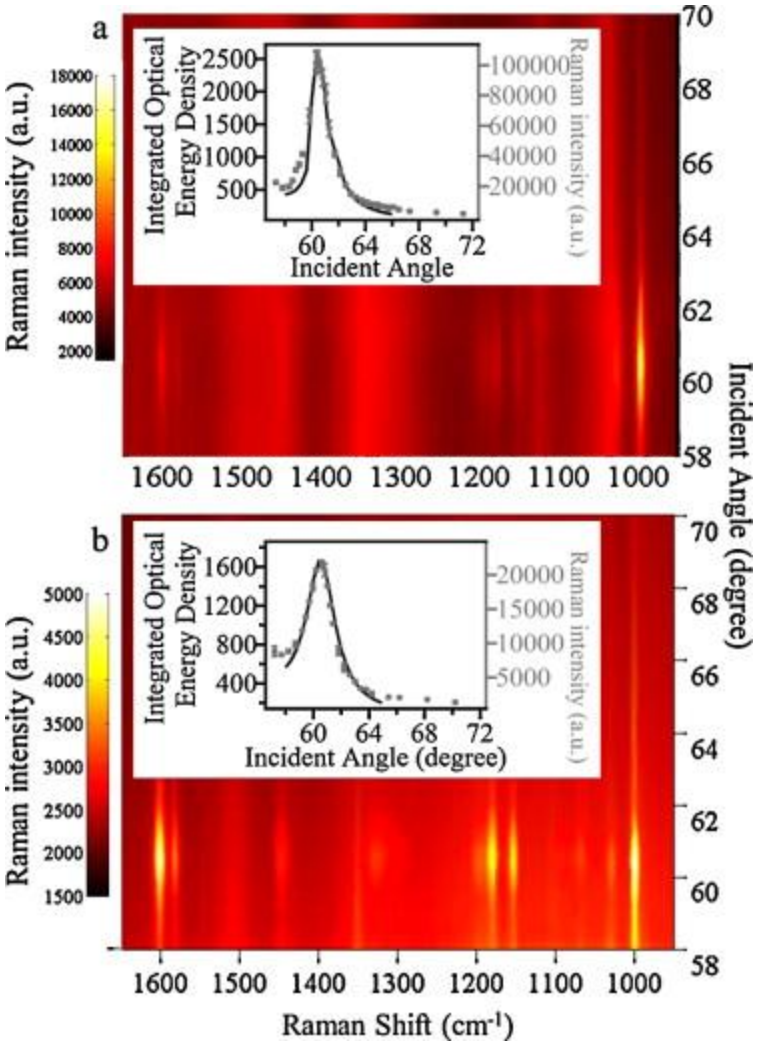

Fig. 3. Two-dimensional plot of the Raman scatter as a function of Raman shift and incident angle using (a) s-polarized or (b) p-polarized incident light and a 9% (w/v) polystyrene film. Insets: (gray symbol) Experimental Raman scatter of the 1001 cm−1 peak across all incident angles and (black line) the calculated integrated optical energy density using 785-nm excitation, 950-nm polymer thickness, (a) s-polarized excitation (*Ey*2), (b) p-polarized excitation (*Ez*2 + *Ex*2).

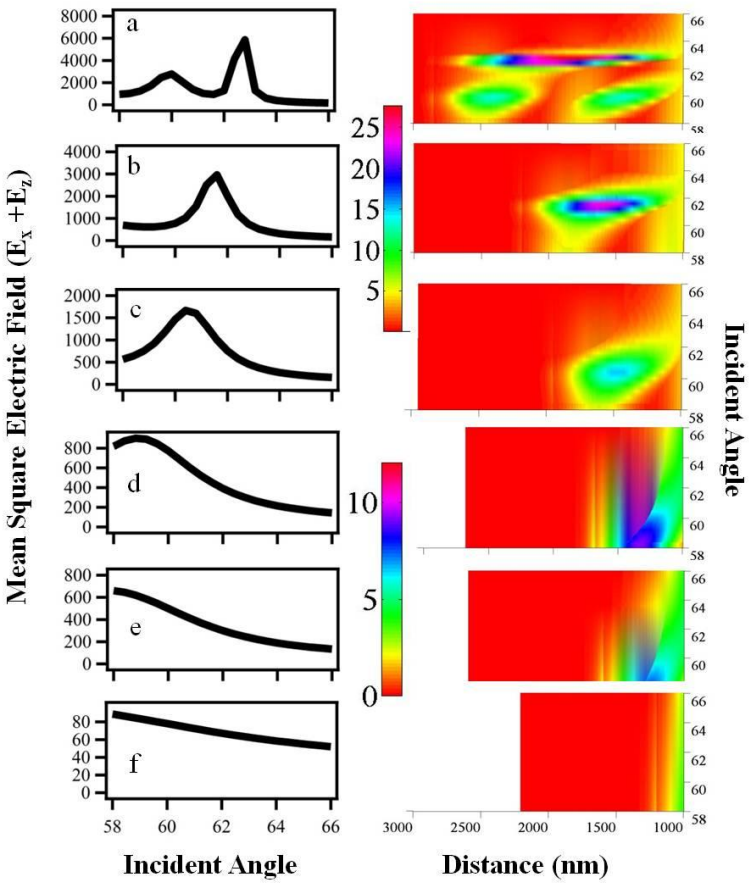

Fig. 4. Calculated integrated optical energy density over the entire film thickness as a function of incident angle (left column) with an angle resolution of 0.4°, and a 2D plot of the electric field distribution as a function of incident angle and the distance away from the sapphire/polymer interface (right column) with the interface designated at 1000 nm for polymer (η = 1.578) film thickness: (a) 1800 nm, (b) 1200 nm, (c) 950 nm, (d) 725 nm, (e) 600 nm and (f) 200 nm (right column). The intensity scale is the same for the top three plots and the bottom three plots.

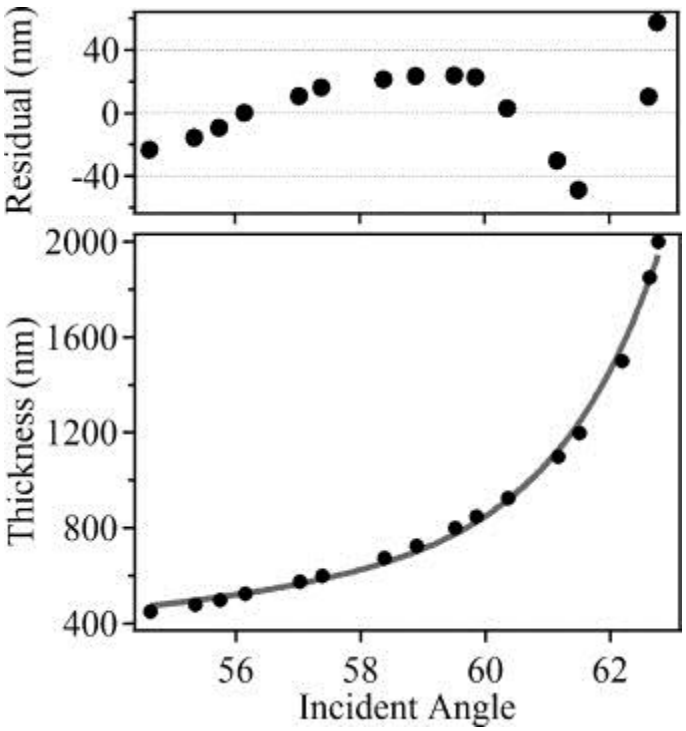

Fig. 5. Calibration plot for the polymer thickness as a function of the incident angle producing the maximum Raman scatter of the 1001 cm^{-1} polystyrene peak. Experimental data (black symbol) were fit to a double exponential curve (gray line) to generate the fit equation shown in the text. The upper plot shows the residual between the experimental points and the double exponential fit.

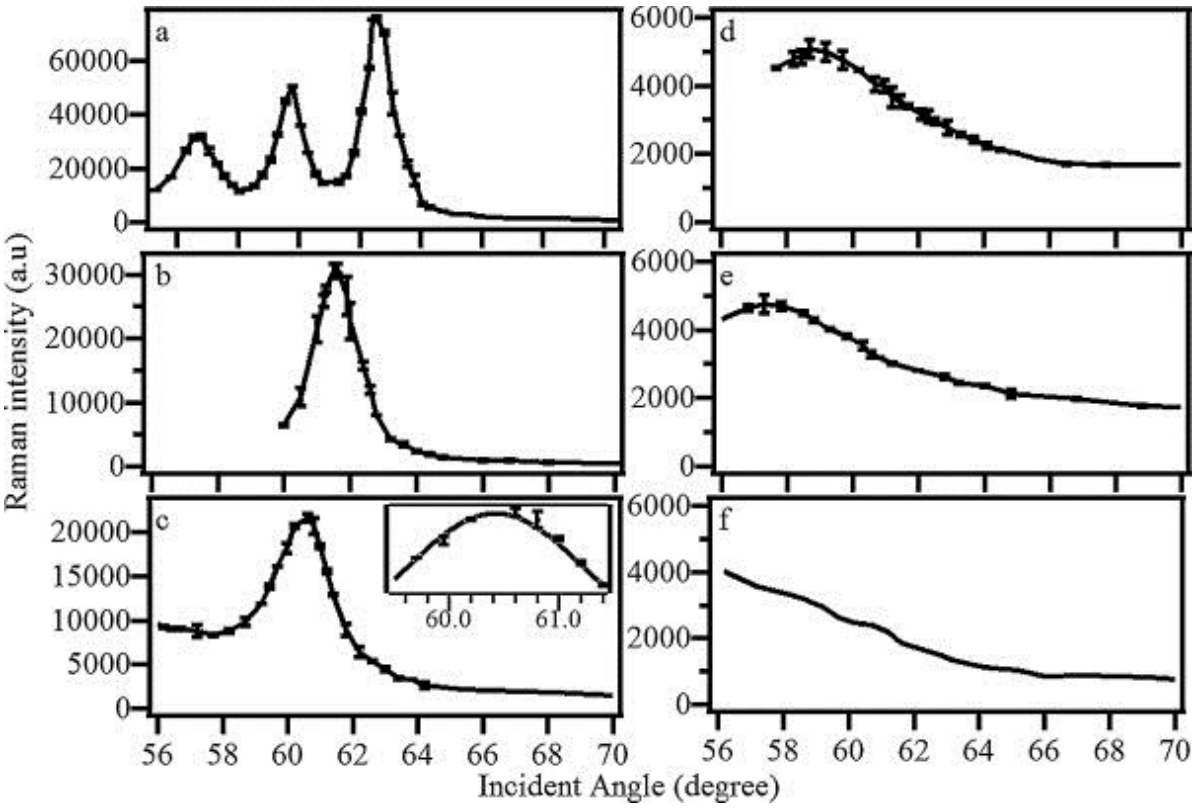

Fig. 6. Experimental Raman scatter of the polystyrene 1001 cm^{-1} ring breathing mode as a function of incident angle for thin films spin coated from a polystyrene solution of (a) 12, (b) 10, (c) 9, (d) 7, (e) 6 or (f) 4% (w/v) in toluene. Error bars are included on all data except panel f and represent the standard deviation from duplicate Raman measurements from each film. (c) The inset shows a representative weighted Gaussian fit to the experimental Raman scatter for the 9% (w/v) polystyrene film.

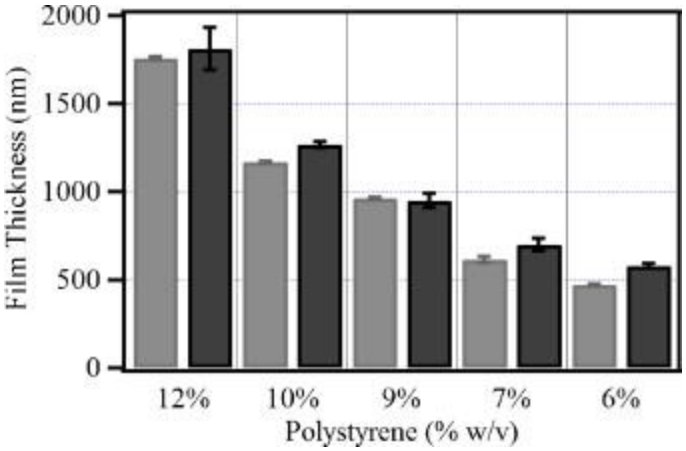

Fig. 7. Polystyrene thickness measured by scanning angle Raman spectroscopy (black) or optical interferometry (gray) for films coated from solutions with the indicated polystyrene concentration. A different set of films was measured by each technique using the same fabrication parameters. Error bars represent the standard deviation for duplicate Raman and triplicate interferometry measurements of the polystyrene film.

APPENDIX C:

SCANNING ANGLE PLASMON WAVEGUIDE RESONANCE RAMAN SPECTROSCOPY FOR THE ANALYSIS OF THIN POLYSTYRENE FILMS

A paper published in The Journal of Physical Chemistry C.

*Matthew Meyer,[1,2] , Kristopher J. McKee [1,2] ,Vy H.T. Nguyen[1,2], Emily A. Smith[1,2]**

[1]Ames Laboratory, U. S. Department of Energy, Ames, Iowa 50011-3111

[2]Department of Chemistry, Iowa State University, Ames, Iowa 50011-3111

ABSTRACT

Scanning angle (SA) Raman spectroscopy was used to characterize thin polymer films at a sapphire/50 nm gold film/polystyrene/air interface. When the polymer thickness is greater than ~260 nm, this interface behaves as a plasmon waveguide; Raman scatter is greatly enhanced with both p- and s-polarized excitation compared to an interface without the gold film. In this study, the reflected light intensities from the interface and Raman spectra were collected as a function of incident angle for three samples with different polystyrene thicknesses. The Raman peak areas were well modeled with the calculated mean-square electric field (MSEF) integrated over the polymer film at varying incident angles. A 412 nm polystyrene plasmon waveguide generated 3.34× the Raman signal at 40.52° (the plasmon waveguide resonance angle) compared to the signal measured at 70.4° (the surface plasmon resonance angle). None of the studied polystyrene plasmon waveguides produced detectable Raman scatter using a 180° backscatter collection geometry, demonstrating the sensitivity of the SA Raman technique. The data highlight the ability to measure polymer thickness,

chemical content, and, when combined with calculations of MSEF as a function of distance from the interface, details of polymer structure and order. The SA Raman spectroscopy thickness measurements agreed with those obtained from optical interferometery with an average difference of 2.6%. This technique has the potential to impact the rapidly developing technologies utilizing metal/polymer films for energy storage and electronic devices.

INTRODUCTION

Total internal reflection (TIR) Raman spectroscopy is an analytical technique used to measure chemical content near an interface.[1–3] In a typical TIR Raman experiment the illuminating light is directed onto a prism/sample/bulk interface at a precise incident angle.[4] At angles above the critical angle, total internal reflection conditions occur, and a surface-sensitive evanescent wave is generated in the sample. TIR-Raman spectroscopy has been useful in studying films, surfactants, plants, and adsorbates at various interfaces.[5–8] As with conventional Raman spectroscopy, TIR Raman spectros-copy has the benefits of being noninvasive, fast, and requiring minimal sample preparation provided the sample can be optically coupled to the prism. For conditions where the same amount of analyte is probed, the TIR Raman geometry acts as a signal enhancement mechanism, and excellent signal-to-noise ratio spectra are possible for thin films using several second acquisition times.

TIR-Raman spectroscopy has been combined with surface plasmon resonance (SPR-Raman spectroscopy) using thin noble metal films to provide predictable signal enhancements, high experimental reproducibility, and the ability to accurately model data with theoretical calculations.[9–11] An example interface used for SPR-Raman spectroscopy is prism/gold/ sample/bulk medium. The SPR phenomenon occurs at incident angles where

propagating surface-plasmon-polaritons are excited in the metal film. Under these conditions, the generated evanescent wave extends spatially into the sample. This field can produce Raman scatter from the molecules located within $D_p/2$, where D_p is the penetration depth of the evanescent wave.[4] McKee et al. used SPR-Raman spectroscopy for reproducible Raman enhancements ranging from 4.7× to 3.7× for aqueous pyridine and nitrobenzene at a sapphire/ gold/sample interface compared to a sapphire/sample inter-face.[12] The latter signal is already approximately an order of magnitude greater than probing the same amount of analyte using normal illumination geometries. The enhancements from the smooth gold films allowed for the detection of single monolayers of benzenethiol and 4-mercaptopyridine with nonresonant excitation.

Thin polymer films are critical components of many devices including sensors, coatings, and medical implants.[13] Common optical methods for measuring thin polymer films include ellipsometry, optical interferometry, attenuated total internal reflection infrared spectroscopy, and TIR-Raman spectrosco-py.[14−16] TIR-Raman spectroscopy provides the advantage of measuring thickness, structure, and chemical content simulta-neously, at a variety of interfaces.[17−19] TIR-Raman spectroscopy was used to study thin polymer films at a glass interface.[20,21]

Most recently, Kivioja et al. used TIR-Raman spectroscopy at a fixed incident angle to measure thin polystyrene films on a sapphire interface.[22] Optical waveguides can be used to confine incident light within a sample or carry incident light to the sample for the analysis of thin films.[23] When a polymer film of approximately $\lambda/2\eta$ (λ wavelength of excitation, η index of refraction of the sample) thickness is coated on a surface plasmon supporting metal film with a bulk air layer, the polymer can act as a radiative or "leaky" waveguide.[24,25]

Recently, leaky waveguideshave been used as biosensors for clinical diagnosis and bacterial analysis.[24,26] Kanger et al. used waveguides in Raman spectroscopy experiments to measure the orientation of porphyrin monolayers.[27] Their results showed the preferred orientation of the molecules can be obtained using deviations of the monolayer's depolarization ratios from those measured in the bulk. Zimba et al. calculated the expected effects of excitation wavelength on waveguide Raman spectra at a quartz/ polymer interface.[28]

At the plasmon waveguide interface, large increases in the interfacial mean square electric field relative to the incident field (MSEF) are generated at incident angles where plasmon waveguide resonances (PWR) are excited.[29] Until recently, a majority of PWR spectroscopy measurements only utilized the reflected light intensity from the interface.[30] At the PWR angles, a sharp attenuation of the reflected light occurs with both p- and s-polarized incident light. When PWR and Raman spectroscopies are combined (PWR Raman spectroscopy), strong enhancements of the Raman signal are expected at the PWR angle(s) due to enhancements in the MSEF. The incident angle(s) where plasmon waveguide resonances are excited depends on the thickness of the polymer layer; thus, polymer films of different thickness should generate unique patterns of Raman scattering intensities as the incident angle is scanned. One advantage of PWR Raman spectroscopy, compared to SPR Raman spectroscopy is that both p-polarized light (electric field oriented parallel to the plane of incidence) and s-polarized (perpendicular) light can be used to produce MSEF in the X, Y, and Z direction ($MSEF_X$, $MSEF_Y$, $MSEF_Z$), where X and Y extend in the focal plane and Z is perpendicular to the focal plane. In SPR-Raman spectroscopy no $MSEF_Y$ component is generated.

The goals of this study are to record and model the PWR Raman intensity as the

incident angle of light is scanned for thin polystyrene films coated on sapphire/gold substrates. PWR-Raman measurements of polystyrene films with thicknesses of 276, 412, and 595 nm on 50 nm gold films were measured. Large Raman signals were recorded for thin polystyrene films down to a few hundred nanometers using p- and s-polarized excitation; the Raman signal and polystyrene thickness can be well modeled by electric field calculations.

EXPERIMENTAL SECTION

Sample Preparation.

Gold films were prepared on 25.4 mm diameter sapphire discs (Meller Optics, Providence, RI) by deposition of 2 nm Ti followed by 49 ± 1 nm of gold at GWC Technologies Inc., Madison, WI. Prior to coating, the gold film was cleaned in ethanol and dried with a stream of N_2 gas. A 4.6, 6, or 8% (w/v) polystyrene (Sigma-Aldrich, St. Louis, MO) solution was prepared in toluene (Fisher Scientific, Waltham, MA), and 200 μL of the polystyrene solution was spin-coated on the gold-coated sapphire disk at 3000 rpm for 1 min using a KW-4A spin-coater (Chemat Technology, Inc. Northridge, CA). The sample was dried overnight at room temperature to make certain the solvent was completely evaporated. Gold and polymer film thicknesses were measured using a F20 series film measurement system in transmission mode (Filmetrics, San Diego, CA).

Raman Measurements.

A scanning angle Raman micro-scope with 0.05° incident angle resolution was used to simultaneously collect Raman and reflectivity spectra.[4] Raman data were collected with angle increments ranging from 0.05° near the PWR angle to 0.20° far away from the PWR

angle. Incident excitation was from a 785 nm laser with 210 mW measured at the sample. The laser power had a 0.4% relative uncertainty for all Raman measurements, which means the laser power varied by no more than ~1 mW from sample to sample. A 25.4 mm diameter sapphire prism was used for the total internal reflection element, and a 10× magnification objective (Nikon, numerical aperture 0.3) was used to collect the Raman scatter. Immersion oil (Cargille Laboratories, Cedar Groove, NJ, n = 1.7800) was used to ensure optical contact between the prism and substrate. A half-wave plate in the excitation path was used to control the polarization of the incident light at the sample interface. The polarization at the sample was 99+% pure. All spectra were acquired with 1 min acquisitions, and three replicate measurements were obtained for each sample by taking consecutive scans through the entire incident angle range.

Depolarization Ratio Measurements.

20% (w/v) polystyrene was dissolved in carbon tetrachloride (Sigma-Aldrich, St. Louis, MO). A near-infrared polarizer was placed in the illumination path, and a second polarizer was placed between the microscope and spectrometer. A scrambler was added between the second polarizer and spectrometer. Raman spectra were collected for 30 s with the collection polarizer set to collect TE or TM polarized Raman scatter.

Data Analysis.

All data analysis was performed using the software IGOR Pro 6.1. Raman peak areas were measured by fitting them to Gaussian curves with the "Multipeak fitting 2" algorithm. Signal-to-noise ratios (S/N) were calculated as the maximum of the 1001 cm^{-1} peak intensity

after background subtraction divided by the standard deviation of the noise measured from 920 to 950 cm^{-1} in a region of the spectrum where no analyte peaks were present. Fresnel calculations were used to model the reflected light intensity.[31] The Fresnel calculations account for the 0.5° incident angle spread that results from focusing within the prism.

Mean-Square Electric Field Calculations.

3-D finite-difference-time-domain (FDTD)-based simulations were used to calculate the MSEF at varying incident angles (EM Explorer, San Francisco, CA). A Yee cell size of 5 nm was used for all FDTD simulations, and the calculations account for multiple reflections within the polymer layer. The interface had a sapphire prism (η_o 1.761, η_e 1.753), 50 nm gold film (η 0.143 +4.799i), and a polystyrene layer of varying thickness (η 1.578), and the bulk medium was air.[32,33] The angular resolution used for the calculations was 0.05° near the PWR angle and 0.5° elsewhere.

RESULTS AND DISCUSSION

Calculated Reflectivity and Predicted Raman Peak Areas for a Sapphire/50 nm Au/Polystyrene/Air Inter-face.

The purpose of this study is to measure and model the PWR Raman signal for polystyrene waveguides of varying thickness. Determining the polymer thickness and chemical composition is possible by analyzing the PWR-Raman spectra as a function of incident angle. Figure 1 shows the calculated reflected light intensity (Figure 1A,C) and MSEF integrated over the polymer thickness (Figure 1B,D) at a sapphire/50 nm gold film interface containing a 276 nm (solid black), 412 nm (solid gray), or 595 nm (dotted black)

polystyrene film. Using p-polarized excitation, $MSEF_{Z+X}$ is generated (Figure 1B), while s-polarized excitation generates $MSEF_Y$ (Figure 1D). The coordinate system used in this work is shown in Figure 1.

For p-polarized excitation, the reflected light intensity is attenuated at some angles within the angle range of 34.5°−60° for all three interfaces. In this range, the angle where the attenuation of the reflected light intensity occurs is commonly referred to at the PWR angle.[34] The PWR angle undergoes a shift from 34.51° to 40.52° when the film thickness is increased from 276 to 412 nm. The reflectivity curve for the 595 nm polystyrene film contains two waveguiding modes (m = 0 and m = 1) using p-polarized excitation, giving rise to PWR angles of 34.48° and 50.77°, respectively. The PWR angle generated with s-polarized light is not the same as the PWR angle generated with p-polarized light. Although the associated angles and magnitudes are different, qualitatively, the same trends are expected in the reflectivity curves using s-polarized excitation. The shift in the PWR angle is sensitive to small changes in the polystyrene thickness. For example, the PWR angle for a 600 nm polystyrene film will undergo a 0.37° (p-polarization) and a 0.15° (s-polarization) shift when the thickness is increased to 610 nm.

For polystyrene films and using a 785 nm wavelength laser, the cutoff thickness for PWR Raman spectroscopy using a prism/gold/polystyrene/air interface with p- and s-polarized excitation is approximately 260 and 140 nm, respectively. For films thinner than this, PWR Raman spectroscopy using a prism/gold/silica/polystyrene/bulk medium interface may be utilized.[35] In theory polystyrene films of several micrometers can be measured with PWR Raman spectroscopy. A 5 μm film will produce 15 distinct waveguide modes with p- or s-polarized excitation over an angle range of 35°−65°. In practice, films of several

micrometers thickness present an experimental challenge due to the required angular resolution. The fwhm for the PWR peaks corresponding to polymer thickness below ~600 nm range from 0.04° to 0.5°; the PWR peaks with s-polarized excitation are generally narrower than those with p-polarized excitation. Experimental measurements should have an angular resolution equal to or smaller than the fwhm.

The sharp attenuation of the reflected light at the PWR angle is a near mirror reflection of the corresponding MSEF curves (Figure 1B,D), which is expected to model the Raman scatter. The 276 nm polystyrene film is at the cusp of the polymer thickness required to generate a PWR peak using p-polarized incident light and is associated with the lowest calculated MSEF (maximum integrated $MSEF_{Z+X}$ 38.1). The 412 and 595 nm polystyrene films, on the other hand, exhibit distinct PWR peaks. In contrast to p-polarized excitation, even the thinnest film is expected to exhibit significant Raman signals (maximum integrated $MSEF_Y$ up to 17700) using s-polarized excitation.

At an angle greater than 60° there is a broad attenuation dip in the reflectivity curve using p-polarized excitation. The angle where this dip occurs is referred to as the SPR angle and is the angle where the maximum Raman scatter is predicted in SPR-Raman spectroscopy. The MSEF enhancement is similar at the SPR angle regardless of whether the interface supports waveguide modes (Table 1). On the other hand, the MSEF enhancement is greater at the PWR angle than the SPR angle, and s-polarized light generates a $MSEF_Y$ component at the waveguide interface.

Compared to an interface without the gold film, the calculated MSEF at the gold film is approximately 10−50× higher. Since the MSEF is proportional to the expected Raman scatter generated at the interface, it is proposed that the PWR Raman measurements will

generate more Raman scatter when the same polymer thickness is considered. The expected, large PWR Raman signal means one or several second acquisition times should generate significant Raman scatter, which decreases the total analysis time per sample without compromising the spectral signal-to-noise ratio.

Experimental Reflectivity Curves and Determination of Polystyrene Thickness.

Reflectivity curves collected with p-polarized incident light are shown in Figure 2A, B, C for three thicknesses of polystyrene. Only the films fabricated using 6 or 8% (w/v) polystyrene generated a PWR peak, while the 4.6% (w/v) film produced only an SPR peak. The reflectivity curve of a 8% (w/v) polystyrene film using s-polarized incident light is shown in Figure 2D. The polystyrene film thickness was determined by modeling the location of the PWR or SPR angle(s) using Fresnel calculations.[31] While holding all other parameter constant, the thickness of the polystyrene layer was varied until the best fit was obtained (Figure 2: A, 276 nm; B, 412 nm; and C, D, 595 nm). For the 595 nm polystyrene film, the thickness that generated the best fit to the PWR peaks did not fit the SPR peak as well. A small increase in the imaginary component of gold's index of refraction will shift the calculated SPR peak to the left, with minimal perturbations to the PWR peak. This suggests there is heterogeneity in the gold films on which the polymer was deposited, which is reasonable since they were fabricated in several batches. For the 595 nm polystyrene film using s-polarized excitation, the attenuation of the reflected light corresponding to the m = 1 guided mode at 41.80° is experimentally measured, but the predicted m = 0 mode at 57.57° is not. The fwhm of the PWR reflectivity peaks are calculated to be roughly 6× narrower than the SPR peaks. The lack of a measured PWR peak at 57.57° is attributed to the narrowness of

the PWR peak (fwhm 0.04°) and the instrument's angular resolution of 0.05°. This is also the reason the experimental reflectivity minima is less than predicted in several instances.

The polymer thicknesses obtained from the modeled reflectivity data agree with a calibration curve generated using optical interferometry (data not shown). The difference between the scanning angle Raman and optical interferometry measurements is associated with an average difference of 2.6% for all three films. Potential errors involved in the thickness measurement include the instrument's incident angle calibra-tion, the finite angular resolution of the instrument, and uncertainties in the gold film thickness or indices of refraction of any of the interfacial layers.

PWR-Raman Spectra of Polystyrene Films.

Raman spectra are shown in Figure 3 for the same samples used to simultaneously generate the reflectivity data in Figure 2. Assignments for the most intense peaks are shown in Table 2. The Raman spectra were collected at an incident angle of 68.40° (p, 276 nm polystyrene), 40.52° (p, 412 nm polystyrene), 50.77° (p, 595 nm polystyrene), or 41.80° (s, 595 nm polystyrene), which correspond to the incident angles that generated the greatest Raman scatter. For the 276 nm film, the highest Raman scatter was collected at the SPR angle, which is expected since no PWR peak was measured for this film. The higher 1003 cm^{-1} peak intensity for s-polarized excitation compared to p-polarized excitation quantitatively agrees with the calculated MSEF from Figure 1 when the magnitude of the reflected light intensity is considered.

The PWR Raman spectrum's S/N ratio for the 412 nm polystyrene film is 602 (Figure 3B) using a 60 s acquisition time, which is significantly better than the S/N ratio of 28 for a

580 nm film at the sapphire interface without a gold film (data not shown). The gold film enables the acquisition time to be reduced to a couple of seconds per spectrum to achieve the same S/N ratio as a 60 s acquisition for a similar film thickness deposited on sapphire. It should also be stated that none of the polystyrene waveguides produced detectable Raman scatter using a 180° backscatter geometry with the same instrument.

The insets in Figure 3C,D show the spectra normalized to the most intense polystyrene peak (1003 cm^{-1}) to compare the relative peak intensities using different excitation polarizations. PWR-Raman measurements of polystyrene show certain bands produce more Raman scatter with p-polarized excitation compared to s-polarized excitation when the spectra are normalized to the 1003 cm^{-1} polarized peak. Table 2 lists the ratio of the PWR Raman peak intensity for s/p-polarized excitation and the 595 nm film. Also shown in Table 2 are the depolarization ratios measured for a solution of polystyrene with the 180° backscattering geometry. The polarized bands produced a s/p-peak intensity ratio greater than 0.8 when comparing spectra normalized to the 1003 cm^{-1} peak. The depolarized bands produce ratios from 0.5 to 0.6. The origin for the differences in the scanning angle Raman spectra using orthogonal excitation has been previously discussed.[12]

Measured Raman Peak Areas and Calculated MSEF.

The Raman peak areas of the polystyrene 1003 cm^{-1} band are plotted as a function of incident angle in Figure 4 for the same samples discussed above. The Raman peak areas fit to the calculated integrated MSEF using the appropriate polymer thickness. The maximum Raman peak area always corresponds to the angle producing the greatest attenuation of the reflected light intensity; thus, the reflected light intensity can be used to identify the angle

producing the largest Raman signal. As expected, this is in good agreement with previous SPR studies that have demonstrated that reflectivity data can be used to predict the collected Raman intensity.[12] The slight differences in the predicted Raman peak area and the measured Raman peak area can be attributed to the same causes discussed above for differences in the reflectivity data (i.e., angle resolution, angle spread, etc.).

The plot of the MSEF as a function of distance from the gold/polystyrene interface (Figure 5) at the PWR angle indicates the collected Raman scatter is not always uniformly generated throughout the polymer film. The radiative or "leaky" waveguide mode maxima are the result of interference between courterpropagating reflections.[36] For thinner polystyrene films and p-polarized excitation only a single leaky mode exists, but for all films with s-polarization and the 595 nm polystyrene film with p-polarized excitation two leaky waveguide modes exist. Both the polymer thickness and the excitation polarization will affect the spatial distribution of the Raman signal within the polymer film. For the 276 and 412 nm polystyrene film, p-polarized excitation will produce Raman intensities nearly uniformly from the entire polymer film at the PWR angle. With thicker films using p-polarized excitation and all thicknesses using s-polarized excitation, the spatial distribution of the MSEF is more complex. For example, the strongest Raman intensity will be generated near the center of the polymer films using s-polarized excitation with the 412 nm film at the PWR angle indicated in the figure legend. For films that contain more than one polymer, the MSEF versus distance plots can be used to aid in the interpretation of polymer structure or order.

CONCLUSION

This proof of principle study shows scanning angle plasmon waveguide resonance Raman spectroscopy can measure thin polymer films with predicable signal enhancements, to obtain simultaneous chemical content and accurate polymer film thicknesses. A polystyrene/air interface was used in this study to ensure that the entire Raman signal was generated from polystyrene and no polymer swelling or contamination occurred. However, other polymer films that are of high optical quality, transparent, and meet the thickness requirements of an optical waveguide could be measured, as could water or organic interfaces. Overall, the method demonstrates that PWR-Raman spectroscopy utilizing a simple plasmonic supporting system allows for optimal experimental modeling of thin films.

ACKNOWLEDGMENT

This research is supported by the U.S. Department of Energy, Office of Basic Energy Sciences, Division of Chemical Sciences, Geosciences, and Biosciences through the Ames Laboratory. The Ames Laboratory is operated for the U.S. Department of Energy by Iowa State University under Contract DE-AC02-07CH11358. The authors thank the Iowa State University Microelectronics Research Center for use of their Filmetrics instrument.

REFERENCES

(1) Ikeshoji, T.; Ono, Y.; Mizuno, T. Appl. Opt. 1973, 12, 2236.

(2) Woods, D. A.; Bain, C. D. Analyst 2012, 137, 35.

(3) Tisinger, L. G.; Sommer, A. J. Microsc. Microanal. 2004, 10, 1318.

(4) McKee, K. J.; Smith, E. A. Rev. Sci. Instrum. 2010, 81, 043106/1.

(5) Hoelzer, W.; Schroeter, O.; Richter, A. J. Mol. Struct. 1990, 217, 253.

(6) Woods, D. A.; Petkov, J.; Bain, C. D. J. Phys. Chem. B 2011, 115, 7341.

(7) Woods, D. A.; Petkov, J.; Bain, C. D. J. Phys. Chem. B 2011, 115, 7353.

(8) Greene, P. R.; Bain, C. D. Colloids Surf., B 2005, 45, 174.

(9) Bolduc, O. R.; Masson, J. F. Anal. Chem. 2011, 83, 8057.

(10) Liu, Y.; Xu, S. P.; Xuan, X. Y.; Zhao, B.; Xu, W. Q. J. Phys. Chem. Lett. 2011, 2, 2218.

(11) Corn, R. M.; Philpott, M. R. J. Chem. Phys. 1984, 80, 5245.

(12) McKee, K. J.; Meyer, M. W.; Smith, E. A. Anal. Chem. 2012, 84, 4300.

(13) Harsanyi, G. Sens. Rev. 2000, 20, 98.

(14) Fina, L. J. Appl. Spectrosc. Rev. 1994, 29, 309.

(15) Yang, P.; Meng, X. F.; Zhang, Z. Y.; Jing, B. X.; Yuan, J.; Yang, W. T. Anal. Chem. 2005, 77, 1068.

(16) Bohn, P. W. Annu. Rev. Mater. Sci. 1997, 27, 469.

(17) Ishizaki, F.; Kim, M. Jpn. J. Appl. Phys. 2008, 47, 1621.

(18) Fontaine, N. H.; Furtak, T. E. Phys. Rev. B 1998, 57, 3807.

(19) Zimba, C. G.; Hallmark, V. M.; Turrell, S.; Swalen, J. D.; Rabolt, J. F. J. Phys. Chem. 1990, 94, 939.

(20) Fontaine, N. H.; Furtak, T. E. J. Opt. Soc. Am. B 1997, 14, 3342.

(21) Ives, J. T.; Reichert, W. M. J. Appl. Polym. Sci. 1988, 36, 429.

(22) Kivioja, A. O.; Jaaskelainen, A. S.; Ahtee, V.; Vuorinen, T. Vib. Spectrosc. 2012, 61, 1.

(23) Chabay, I. Anal. Chem. 1982, 54, A071.

(24) Im, W. J.; Kim, B. B.; Byun, J. Y.; Kim, H. M.; Kim, M.-G.; Shin, Y.-B. Sens. Actuators, B 2012, 173, 288.

(25) Abbas, A.; Linman, M. J.; Cheng, Q. Sens. Actuators, B 2011, 156, 169.

(26) Zourob, M.; Mohr, S.; Brown, B. J. T.; Fielden, P. R.; McDonnell, M. B.; Goddard, N. J. Anal. Chem. 2005, 77, 232.

(27) Kanger, J. S.; Otto, C. Appl. Spectrosc. 2003, 57, 1487.

(28) Zimba, C. G.; Rabolt, J. F. Thin Solid Films 1991, 206, 388.

(29) Bradshaw, J. T.; Mendes, S. B.; Saavedra, S. S. Anal. Chem. 2005, 77, 28a.

(30) Hruby, V. J.; Alves, I.; Cowell, S.; Salamon, Z.; Tollin, G. Life Sci. 2010, 86, 569.

(31) Corn, R. M.; http://corninfor.ps.uci.edu/calculations.html.

(32) Kasarova, S. N.; Sultanova, N. G.; Ivanov, C. D.; Nikolov, I. D. Opt. Mater. 2007, 29, 1481.

(33) Bass, M.; DeCusatis, C.; Enoch, J. M.; Lakshminarayanan, V.; Li, G.; MacDonald, C.; Mahajan, V. N.; Van Stryland, E. Handbook of Optics, 3rd ed.; McGraw-Hill: New York, 2009; Vol. IV.

(34) Salamon, Z.; Tollin, G. Spectrosc.: Int. J. 2001, 15, 161.

(35) McKee, K. J.; Meyer, M. W.; Smith, E. A. Anal. Chem. 2012, 84, 9049.

(36) Zia, R.; Selker, M. D.; Brongersma, M. L. Phys. Rev. B 2005, 71, 165431.

(37) Loader, E. J. J. Catal. 1971, 22, 41.

(38) Palm, A. J. Phys. Chem. 1951, 55, 1320.

FIGURES

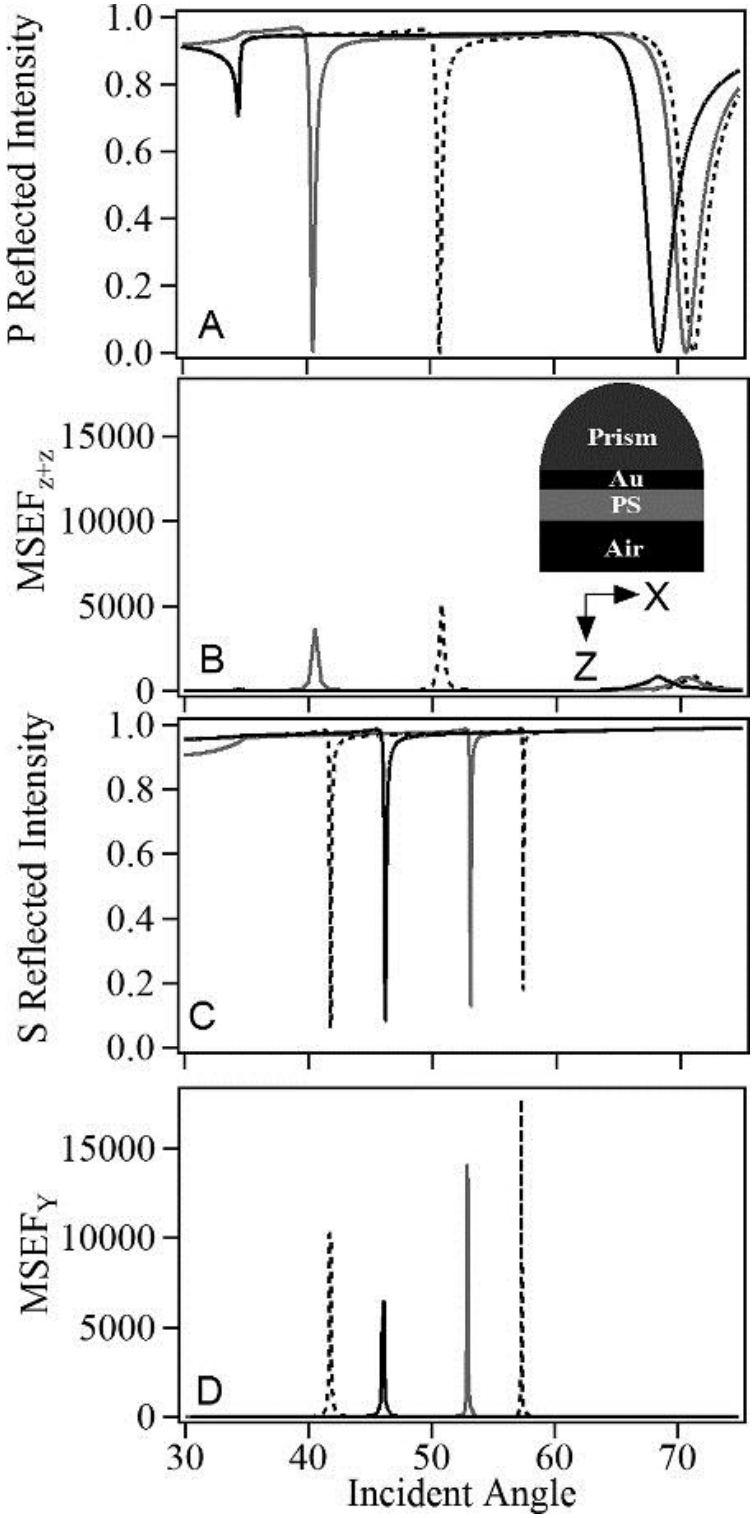
P Reflected Intensity
1.0
0.8
0.6
0.4
0.2
0.0
A
MSEF$_{z+z}$
15000
10000
5000
0
B
Prism
Au
PS
Air
X
Z
S Reflected Intensity
C
MSEF$_{Y}$
D
30
40
50
60
70
Incident Angle

Fig. 1 Calculated reflectivity (A and C) and mean-square electric field integrated over the polymer stack (MSEF, B and D) for a sapphire prism/50 nm gold/polystyrene (PS)/air interface. The thickness of the polystyrene film is 276 nm (solid black), 412 nm (solid gray), or 595 nm (dotted black). The reflectivity calculations used a 0.5° incident angle spread in the excitation light. The p-polarized incident light (A, B) generates a MSEF in the Z and X directions, and s-polarized incident light (C, D) generates a MSEF in the Y direction. The inset schematic shows the coordinate system used in this work; the Y-axis points toward the reader.

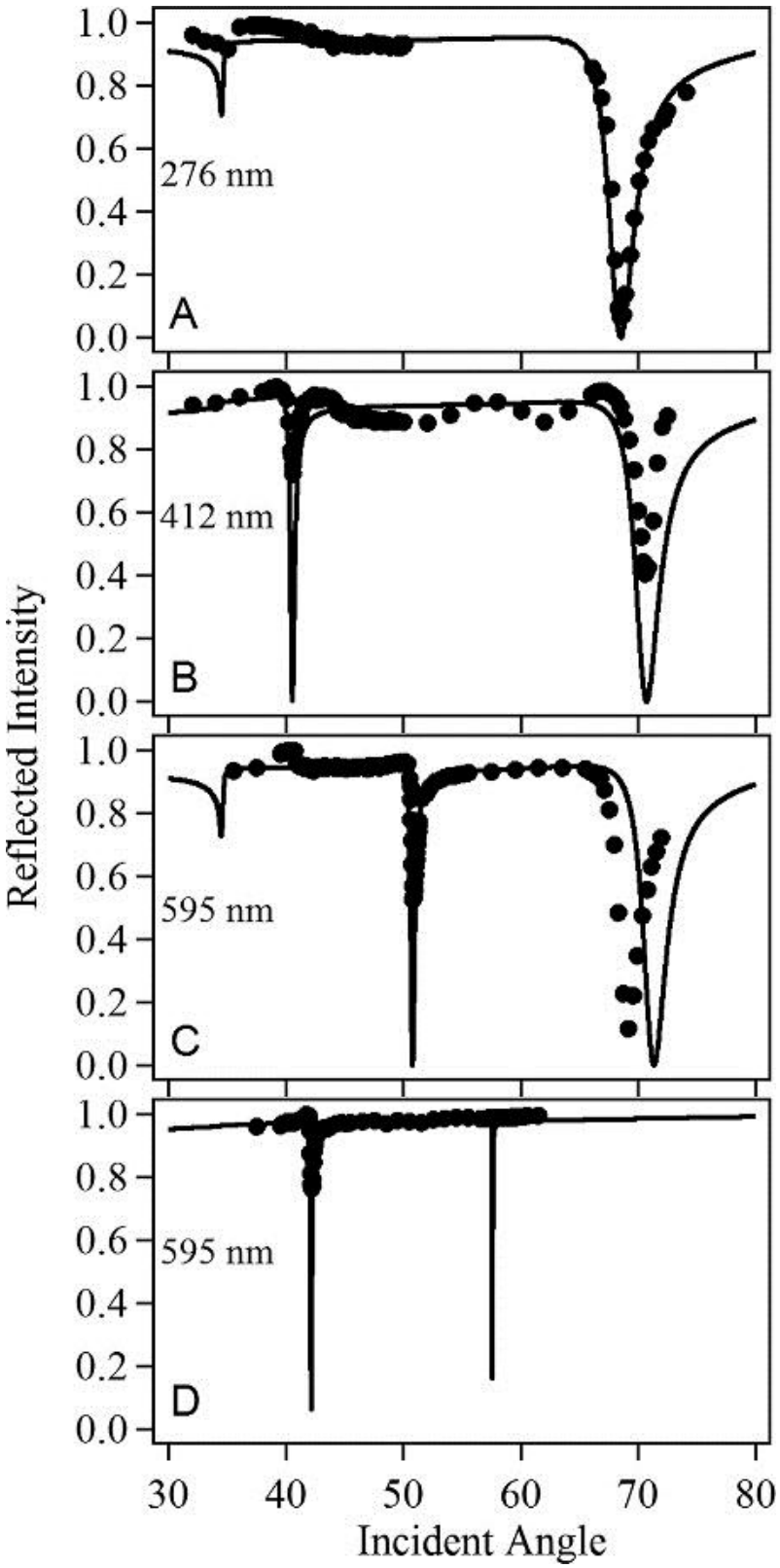
Reflected Intensity
1.0
0.8
0.6
0.4
0.2
0.0
276 nm
A
412 nm
B
595 nm
C
595 nm
D
30
40
50
60
70
80
Incident Angle

Fig. 2 Reflectivity spectra (solid symbols) from a sapphire prism/ 50 nm gold/polystyrene (PS)/air interface: (A) 276 nm PS; (B) 412 nm PS; (C) 595 nm PS collected with p-polarized incident excitation. (D) Sapphire prism/50 nm gold/595 nm polystyrene (PS)/air interface collected with s-polarized incident excitation. The solid lines are calculated reflectivities for the same interfaces.

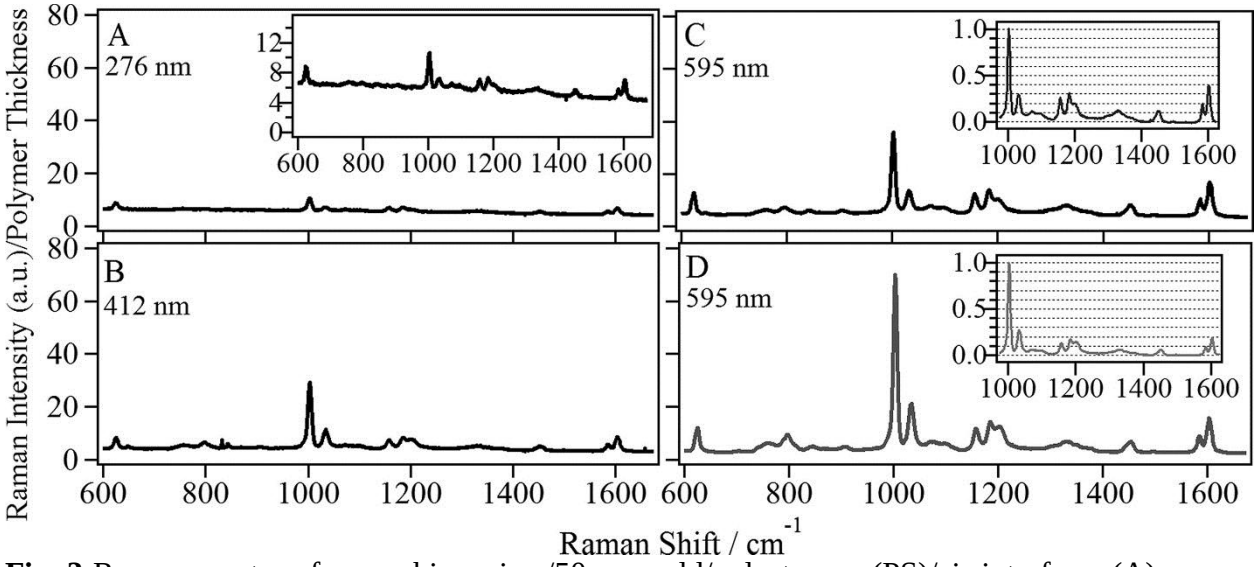

Fig. 3 Raman spectra of a sapphire prism/50 nm gold/polystyrene (PS)/air interface: (A) 276 nm PS; (B) 412 nm PS; (C) 595 nm PS collected with p-polarized incident excitation at 68.40°, 40.52°, and 50.77° incident angle, respectively. (D) Sapphire prism/50 nm gold/595 nm polystyrene (PS)/air interface collected with s-polarized incident excitation at 41.80° incident angle. The inset in (A) shows the same spectrum at a smaller scale. The inset in (C) and (D) show the normalized spectra so that relative peak intensities can be compared. All spectra have been divided by their respective film thickness to emphasize differences in the scattering intensity due to differences in the MSEF. The slight elongation of the beam size at larger incident angles (e.g., 242 μm × 179 μm at 40° and 271 μm × 177 μm at 68°) has not been accounted for in the spectra.

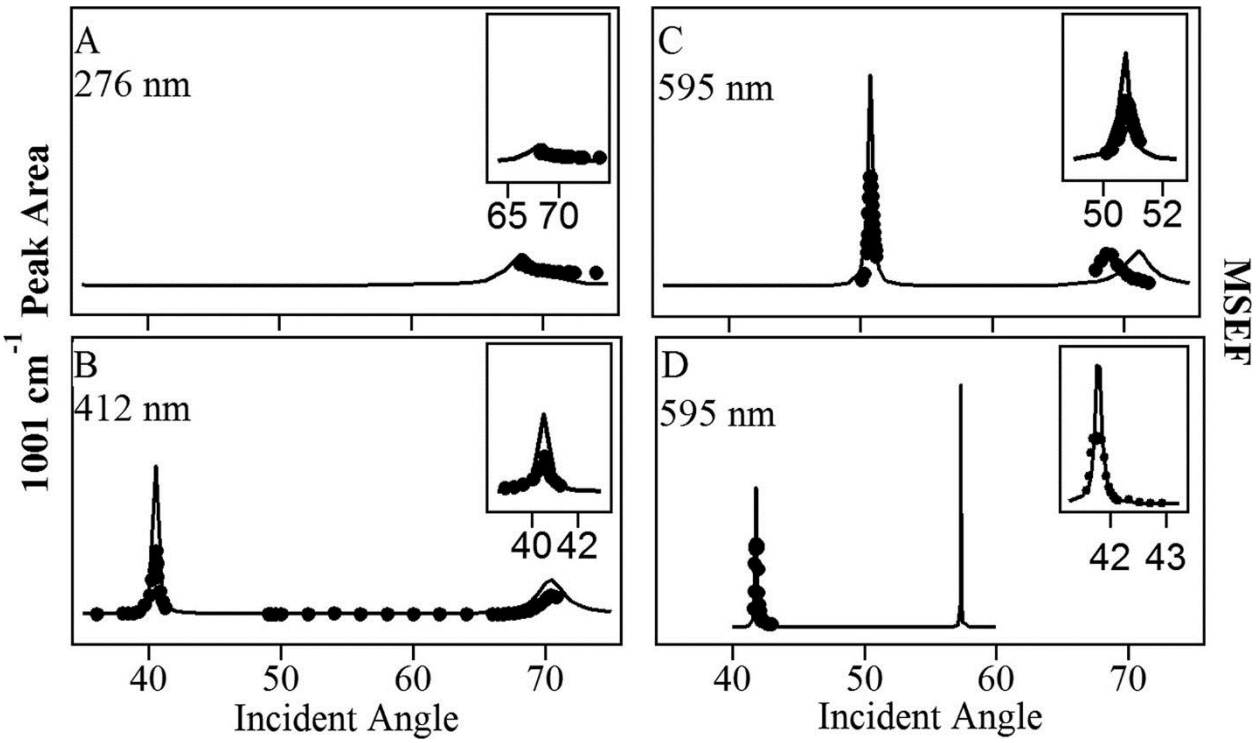

Fig. 4 Raman 1003 cm−1 peak areas (black spheres) as a function of incident angle for a sapphire prism/50 nm gold/polystyrene (PS)/ air interface: (A) 276 nm PS; (B) 412 nm PS; (C) 595 nm PS collected with p-polarized incident excitation. (D) Sapphire prism/50 nm gold/595 nm polystyrene (PS)/air interface collected with s-polarized incident excitation. The solid black line is the calculated MSEF (A, B, C: MSEFZ+X; D: MSEFY) integrated over the entire polymer thickness. The peak area and MSEF scales are the same in (A, B, C) and are expanded 3× in (D). Example MSEF plots at select incident angles are plotted in Figure 5.

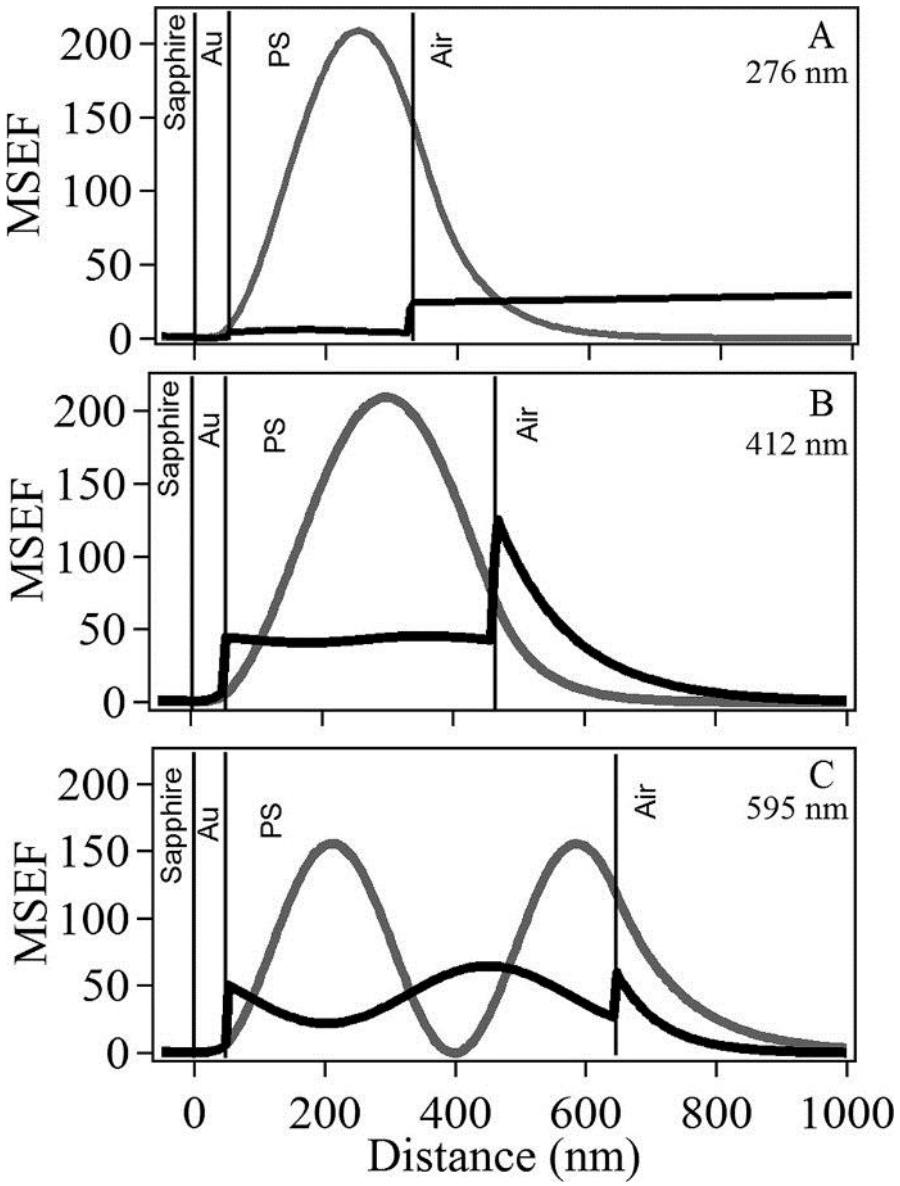

Fig. 5 Calculated MSEF as a function of the distance from the interface for p-polarized (black) and s-polarized (gray) incident excitation and a sapphire prism/50 nm gold/polystyrene (PS)/air stack: (A) 276 nm PS at 34.51° (p-polarized excitation, MSEFZ+X) and 46.20° (s-polarized excitation, MSEFY); (B) 412 nm PS at 40.52° (p) and 53.07° (s); (C) 595 nm PS at 50.77° (p) and 41.80° (s). The location of each phase in the stack is shown with a solid vertical line.

Table 1. Comparison of Surface Plasmon Resonance and Plasmon Waveguide Resonance Parameters for Thin Polystyrene Films at the Sapphire/50 nm Gold/Polystyrene Interface.

Polymer thickness and Platform	SPR/PWR angle (degrees)	FWHM (degrees)	$MSEF_{Ex+Ez}$ Integrated Over Polymer Film	$MSEF_{Ey}$ Integrated Over Polymer Film
Non-waveguide (100 nm) SPR	50.69	2.24	786	0.0
Waveguide (412 nm) SPR	70.67	2.76	839	0.0
PWR (p)	40.52	0.48	3776	0.0
PWR (s)	52.95	0.12	0.0	9651

Table 2. Peak location, assignment and relative intensity ratio for s/p-polarized excitation for scanning angle Raman spectra of polystyrene; measured depolarization ratios for a solution of polystyrene.

Peak (cm^{-1})	Assignment [32,33] (Wilson Notation)	Relative Intensity (s/p): PWR Raman spectroscopy	Solution Depolarization Ratio: Normal illumination Raman Spectroscopy
624	ν_{6b}	0.5	1.08
760		0.8	ca. 0
795	ν_{11}	1	ca. 0
843	$\nu_{10a/17b}$	0.5	
906	vinyl	0.5	
1003	ν_{1}	1	0.06
1031	ν_{18a}	0.9	ca. 0
1073		0.5	
1097		0.6	
1156	ν_{9b}	0.5	0.84
1184	ν_{9a}	0.5	0.65
1201	ν_{7a}	0.8	ca. 0
1304	vinyl	0.6	
1330	ν_{14}	0.5	
1346	ν_{3}	0.5	
1368	vinyl	0.5	
1451	$\nu_{19b/a}$	0.5	
1584	ν_{8b}	0.5	1.22
1602	ν_{8a}	0.5	0.91